

# Packaging and Deployment of Large Planar Spacecraft Structures

Thesis by  
Manan Arya

In Partial Fulfillment of the Requirements  
for the Degree of  
Doctor of Philosophy

The logo for the California Institute of Technology (Caltech), featuring the word "Caltech" in a bold, orange, sans-serif font.

California Institute of Technology  
Pasadena, California

2016  
(Defended 2 May 2016)



# Acknowledgements

Many people helped me as this work unfolded, and therefore there are many people I want to thank. Prime among them is my adviser Professor Sergio Pellegrino; I would be entirely unraveled without his guidance and his expertise, his advocacy and his encouragement. Thanks are also due to members of my dissertation committee, Professor Guruswami ‘Ravi’ Ravichandran, Professor Dennis Kochmann, and Professor Melany Hunt, for their time and their commitment.

Dr. Nicolas Lee and I conceived of the core of the ideas contained herein at the end of a wintry day at a conference just outside Washington, D.C. in January 2014. I could not have asked for a more creative or a more indefatigable partner in these adventures. I am greatly indebted to him.

The Space Solar Power Initiative, a collaboration between Professors Sergio Pellegrino, Harry Atwater, and Ali Hajimiri, provided a definite direction in which to take my ideas. For this I am greatly indebted to them. The Northrop Grumman Corporation funded my work with the Initiative.

Kate Jackson, Christine Ramirez, and Dimity Nelson keep the Pellegrino group, the Aerospace option, and all of GALCIT running, respectively. Things would fall apart without the constant attention of this triad; I am extremely grateful to them. I also want to thank Petros Arakelian for his assistance in the lab, and John Van Deusen for his assistance in the machine shop.

I am also deeply grateful to Dr. Gregory Davis, Dr. Daniel Scharf, Dr. Anthony Freeman, John Baker, Dr. Andrew Shapiro-Scharlotta, and Dr. James Breckinridge for advice and mentorship.

The workshops at the W. M. Keck Institute of Space Studies in which I was lucky enough to participate were tremendous sources of inspiration. Many thanks to Michele Judd, Professor Tom Prince, and Louis Friedman for these amazing workshops.

Many thanks to members of the Space Structures Laboratory for ideas, discussions, and helping hands: Mélanie Delapierre, Dr. John Steeves, Kristina Hogstrom, Thibaud Talon, Dr. Keith Patterson, Dr. Ignacio Maqueda Jiménez, Yuchen Wei, Christophe Leclerc, Thomas Lumpe, Stefan Haegeli Lohaus, Maria Sakovsky, Lee Wilson, and Dr. Stephen Bongiorno.

The Theater community at Caltech – this group of brilliant, bold, madcap, hilarious, fearless, talented, and beautiful people – has given me so much. I have tried my hardest to be worthy of belonging among them, and I am a better person for it.

And, of course, many many thanks to my family and my friends.

# Abstract

This thesis presents a set of novel methods to biaxially package planar structures by folding and wrapping. The structure is divided into strips connected by folds that can slip during wrapping to accommodate material thickness. These packaging schemes are highly efficient, with theoretical packaging efficiencies approaching 100%. Packaging tests on meter-scale physical models have demonstrated packaging efficiencies of up to 83%. These methods avoid permanent deformation of the structure, allowing an initially flat structure to be deployed to a flat state.

Also presented are structural architectures and deployment schemes that are compatible with these packaging methods. These structural architectures use either in-plane pretension – suitable for membrane structures – or out-of-plane bending stiffness to resist loading. Physical models are constructed to realize these structural architectures. The deployment of these types of structures is shown to be controllable and repeatable by conducting experiments on lab-scale models.

These packaging methods, structural architectures, and deployment schemes are applicable to a variety of spacecraft structures such as solar power arrays, solar sails, antenna arrays, and drag sails; they have the potential to enable larger variants of these structures while reducing the packaging volume required. In this thesis, these methods are applied to the preliminary structural design of a space solar power satellite. This deployable spacecraft, measuring  $60\text{ m} \times 60\text{ m}$ , and with an areal density  $100\text{ g m}^{-2}$ , can be packaged into a cylinder measuring 1.5 m in height and 1 m in diameter. It can be deployed to a flat configuration, where it acts as a stiff lightweight support framework for multifunctional tiles that collect sunlight, generate electric power, and transmit it to a ground station on Earth.

# Published Content and Contributions

M. Arya, N. Lee, and S. Pellegrino, “Wrapping Thick Membranes with Slipping Folds”, in 2<sup>nd</sup> AIAA Spacecraft Structures Conference, 2015, doi:10.2514/6.2015-0682.

M.A. co-invented the idea of slip wrapping, did the mathematical analysis, designed and conducted the experiments, and wrote the manuscript.

M. Arya, N. Lee, and S. Pellegrino, “Ultralight Structures for Space Solar Power Satellites”, in 3<sup>rd</sup> AIAA Spacecraft Structures Conference, 2016, doi:10.2514/6.2016-1950.

M.A. invented the packaging method, did the mathematical modeling and analysis, and wrote the manuscript.

# Contents

<b>Acknowledgements</b>	<b>iii</b>
<b>Abstract</b>	<b>iv</b>
<b>Published Content and Contributions</b>	<b>v</b>
<b>1 Introduction</b>	<b>1</b>
1.1 Outline of Thesis . . . . .	2
1.2 State of the Art in the Packaging of Large Planar Structures . . . . .	2
1.2.1 Uniaxial Compaction . . . . .	3
1.2.2 Biaxial Compaction . . . . .	3
1.2.3 Thickness Effects . . . . .	4
1.2.4 Cuts and Slits . . . . .	7
<b>2 Structures with Parallel Slipping Folds</b>	<b>8</b>
2.1 Packaging Concept . . . . .	8
2.1.1 Slipping Folds . . . . .	9
2.1.2 Volume-Based Model of Wrapping . . . . .	10
2.1.3 Maximum Slip . . . . .	15
2.1.4 Packaging Efficiency . . . . .	18
2.1.5 Compaction Ratio . . . . .	19
2.1.6 Combined Elastic and Volume-Based Model of Wrapping . . . . .	20
2.1.7 Packaging Experiments . . . . .	25
2.2 Pretensioning with Scalloped Edges . . . . .	28
2.2.1 Pretensioning Experiment . . . . .	29
2.3 Deployment of Structures with Parallel Slipping Folds . . . . .	31
2.3.1 Estimating Deployment Forces . . . . .	32
2.3.2 Deployment Experiments . . . . .	37
2.4 Summary . . . . .	41

<b>3 Polygonal Structures with Slipping Folds</b>	<b>44</b>
3.1 Packaging Concept . . . . .	44
3.1.1 Volume-Based Model of Wrapping . . . . .	45
3.1.2 Estimate of Maximum Slip . . . . .	50
3.1.3 Packaging Efficiency . . . . .	53
3.1.4 Packaging Experiments . . . . .	55
3.2 Structural Architectures . . . . .	58
3.2.1 Pretensioning with Scalloped Edges . . . . .	58
3.2.2 Strips with Bending Stiffness . . . . .	60
3.3 Deployment Concept . . . . .	64
3.4 Physical Model with Bending-Stiff Strips . . . . .	66
3.4.1 Fabrication Process . . . . .	67
3.4.2 Packaging Experiment . . . . .	68
3.4.3 Deployment Experiments . . . . .	70
3.5 Summary . . . . .	75
<b>4 Structures for Space Solar Power Satellites</b>	<b>76</b>
4.1 The Need for Space Solar Power . . . . .	76
4.2 Space Solar Power Concept . . . . .	77
4.3 Background . . . . .	78
4.3.1 Structures for Space Solar Power Systems . . . . .	78
4.3.2 Concentrating Photovoltaic Systems for Spacecraft . . . . .	80
4.4 Tile Design Concept . . . . .	81
4.5 Space Solar Power Satellite Structural Design . . . . .	83
4.5.1 Numerical Structural Model . . . . .	84
4.5.2 Spacecraft Loading . . . . .	85
4.5.3 Performance Metric . . . . .	89
4.5.4 Structural Design Results . . . . .	93
4.6 Spacecraft Packaging . . . . .	94
4.7 Spacecraft Design Summary . . . . .	95
<b>5 Conclusions</b>	<b>96</b>
5.1 Open Questions . . . . .	97
5.2 Future Work . . . . .	98
<b>A Large Deflections of an Elastic Rod in Bending</b>	<b>100</b>
<b>B Involute of a Circle</b>	<b>104</b>

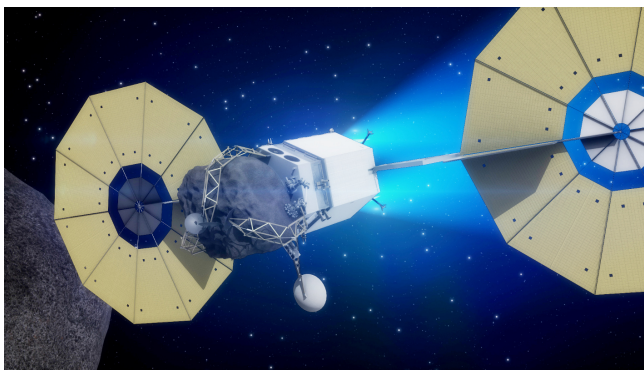
<b>C</b>	<b>Generator Curves for Compact Wrapping</b>	<b>107</b>
C.1	Generator Curve for 2-fold Symmetry . . . . .	107
C.2	Generator Curves for $N$ -fold Symmetry . . . . .	110
<b>D</b>	<b>TRAC Cross-Section Properties</b>	<b>115</b>
<b>E</b>	<b>Cutting Pattern</b>	<b>117</b>
	<b>Bibliography</b>	<b>118</b>

# Chapter 1

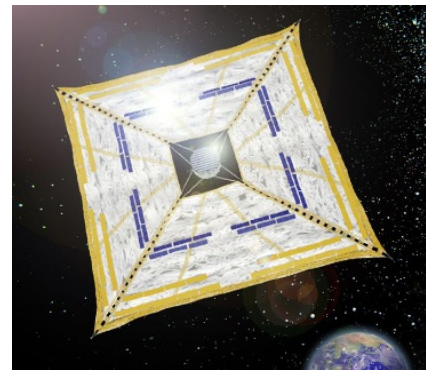
## Introduction

The performance of many kinds of spacecraft structures depends directly on their projected area. Solar power arrays, radio frequency antenna arrays, solar sails, and drag devices are all examples of spacecraft structures for which increased area leads directly to increased performance. In general, two distinct physical principles are responsible for this trend: 1) increased area leads to an increase in the collected quantity of a flux; and 2) increased area results in increased aperture, leading to higher spatial resolution of transmitted and received signals.

To save mass, these large-area structures tend to be thin. Thus the form of these structures is sheet-like: planar with comparable and large dimensions in-plane, and a relatively small out-of-plane thickness. Examples of such structures are shown in Figure 1.1, in the context of the proposed Asteroid Redirect Mission [1] spacecraft, which, like other solar electric missions, requires large solar arrays to generate power for propulsion, and IKAROS [2], a mission that demonstrated the use of solar sail propulsion.



(a) Asteroid Redirect Mission [1].



(b) IKAROS [2].

Figure 1.1: Examples of spacecraft structures that require large area: (a) solar power arrays and (b) solar sails.

Often, these large structures must be packaged to fit into a rocket vehicle for launch and then deployed once in space. This need for packaging and deployment poses four fundamental challenges:

first, biaxial compaction, reducing both of the large in-plane dimensions; second, making efficient use of the stowage volume, leaving minimal voids; third, avoiding permanent deformation of the material, i.e., remaining within the elastic limit; and, fourth, being able to deploy with small and predictable forces, to lower the requirements on the structure that will carry out the deployment. Individually, each of these issues has been addressed in the literature, but the search for solutions to all four challenges combined is a problem still wide open.

This thesis describes novel families of biaxial packaging schemes for large planar structures that fold and wrap the structure into a compact form. These packaging schemes accommodate arbitrarily large out-of-plane thicknesses and avoid kinematic incompatibilities in the wrapping step by using slipping folds. Without slipping folds, there would be buckles and spurious creasing during wrapping, leading to decreased packaging efficiency, plastic deformation, and non-smooth deployment.

## 1.1 Outline of Thesis

Two general families of packaging methods are described: Chapter 2 discusses z-folding and wrapping, and Chapter 3 discusses star folding and wrapping. In both cases, mathematical models of the packaging process are developed, and validated through packaging experiments on physical models.

In each of these two chapters, applicable structural architectures and deployment strategies are also described. Analytical tools are developed to aid in the design of these structures and deployment schemes. These structural architectures and deployment strategies are experimentally demonstrated using lab-scale models.

Chapter 4 applies these ideas to the preliminary structural design of a space solar power satellite. Many of the analytical tools developed in Chapter 2 and Chapter 3 are leveraged here to develop an initial design for a large, lightweight, and stiff structure that can package compactly for launch.

Finally, Chapter 5 offers some conclusions, and provides an outlook of future work that may be conducted to further advance the ideas, concepts, and models described herein.

## 1.2 State of the Art in the Packaging of Large Planar Structures

Existing packaging solutions can be divided into two broad categories, those providing compaction in one dimension, and those providing biaxial compaction.

Most solutions use folding as the basic mechanism for compaction; folding can be accomplished either by creasing, i.e., a local bending deformation of the material, or through mechanical hinges. Heavy creasing results in plastic deformation, and a plastically creased membrane structure cannot

be pulled flat using in-plane tension [3, 4]. Mechanical hinges, on the other hand, may be unfolded using in-plane tension alone, though they add mass and complexity to the structure.

### 1.2.1 Uniaxial Compaction

Well-known techniques for one-dimensional packaging include: z-folding, wrapping (or rolling), and fan-folding. These techniques address three of the four packaging challenges listed above: they provide efficient packaging, can accommodate the thickness of the material, and can avoid plastic deformation. However, they do not provide biaxial compaction.

Deployment and pretensioning can be carried out by a simple, uniaxial deployment mechanism, e.g., with a linear actuator such as a telescopic boom. For example, the first set of solar arrays for the Hubble Space Telescope adopted a wrapping packaging scheme for the solar power array and two deployable booms for each wing of the array.

However, compaction occurs in one dimension only, and hence these techniques are not applicable when both in-plane dimensions of the deployed structure exceed the available packaging envelope.

### 1.2.2 Biaxial Compaction

Several solutions for biaxial compaction have been proposed; almost all of these are drawn from the world of origami. Origami mathematics provides useful tools to describe a network of folds that can be used for biaxial compaction.

Miura-ori [5], shown in Figure 1.2a, is a well-known scheme for biaxially packaging a structure. It modifies the standard map folding technique (i.e., double z-folding) by skewing one set of parallel fold lines. Both map folding and Miura-ori have been used for packaging space structures [6, 7].

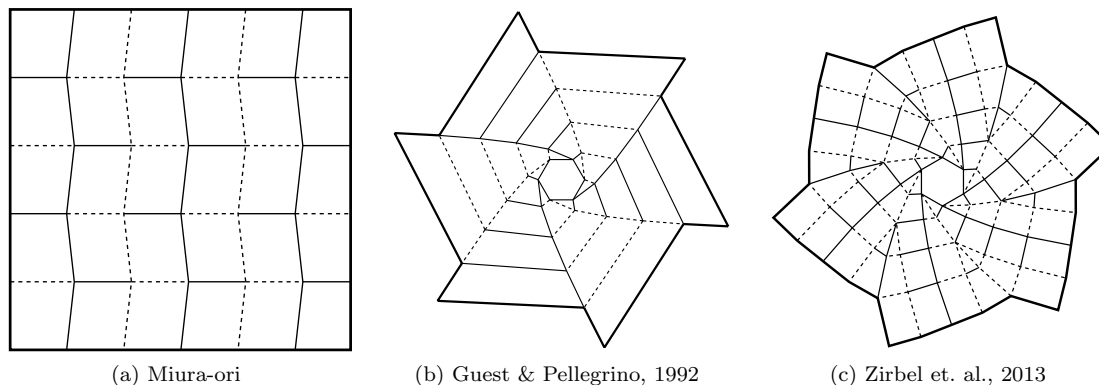


Figure 1.2: Fold patterns for biaxial compaction of structures. Mountain folds are shown as solid lines, valley folds as dotted lines.

There are several techniques for wrapping a membrane around a polygonal hub using straight creases [8, 9]. Examples of 6-fold symmetric crease patterns to wrap a flat membrane around a

hexagonal hub are shown in Figures 1.2b and 1.2c. The curvature of the near-radial crease lines is related to the thickness of the membrane. The coordinates of the vertices of the crease pattern are computed such as to provide sufficient spacing between vertices that fall in the same meridional plane, in the creased configuration. The crease lengths and angles are computed by considering both the flat and the wrapped configurations of the membrane, i.e., neglecting the intermediate configurations.

It is also possible to compact membranes biaxially by first folding in one direction and then wrapping. Both z-folding and wrapping [7], and star folding and wrapping [10] have been proposed. This approach requires the crease lines to be curved to accommodate the thickness of the membrane [11, 12, 13], as is shown in Figure 1.3.

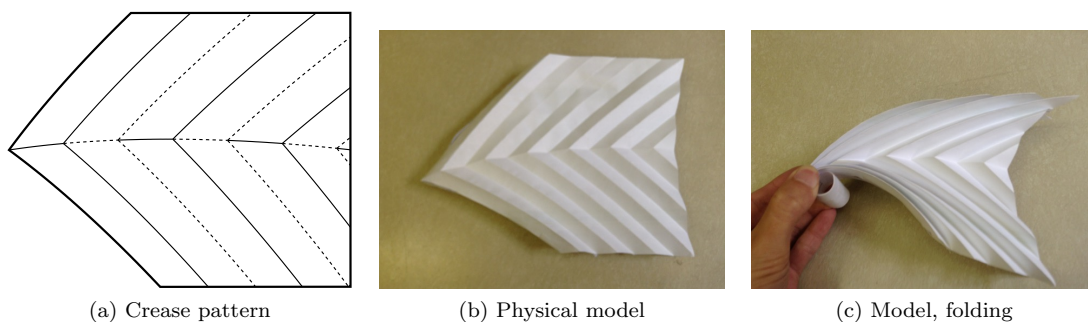


Figure 1.3: Curved crease folding.

### 1.2.3 Thickness Effects

In general, these origami-based schemes account for material thickness by spacing apart the layers in the folded form. The local effects of material thickness, near the fold lines and vertices where the fold lines intersect, are not considered. There exists a growing body of literature on solutions for adapting origami patterns, initially developed for idealized zero-thickness materials, to be realized with finite-thickness materials. This subsection describes some of this work, using, as a simple illustrative example, the case of z-folding.

To accommodate thickness near the fold lines, the hinge axes of the folds can be shifted to either the top or the bottom surface of the material, as illustrated in Figure 1.4. This is known as the *axis shift* method. For biaxial packaging, the amount of axis shift for each fold line at a vertex must be determined to ensure that the vertex is not over-constrained. This amount of axis shift that allows folding has been determined for symmetric degree-4 vertices [14] and, indeed, for any vertex [15]. The structures with these specific hinge axis offsets have a stepped nature; different levels of panel thickness are needed to provide the appropriate axis shifts. Since the hinge axes are not coplanar in the fully deployed state, the kinematics of such structures are different from those of the parent origami fold pattern.

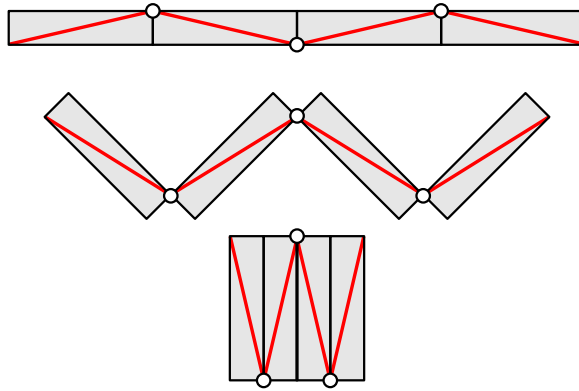


Figure 1.4: Hinge axis shift method for accommodating thickness.

A variant of the axis shift approach is to allow sliding along the hinge lines [16]. This enables the hinge axis offsets to have arbitrary values. However, fully folding a vertex with sliding hinges without allowing any deformation of the panels would require an infinite amount of sliding.

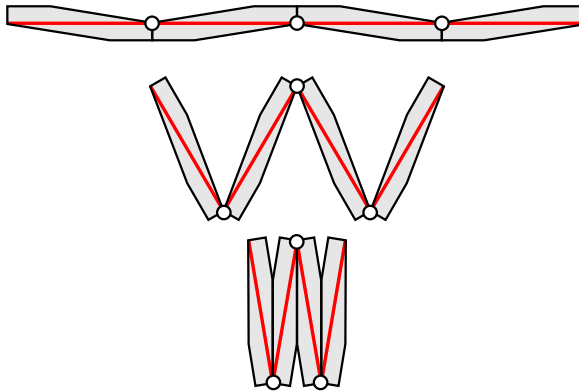


Figure 1.5: Volume trimming method for accommodating thickness.

An alternative method that preserves the kinematics of the underlying origami is called *volume trimming* [17]. As shown in Figure 1.5, the hinge axes remain planar. Material close to the hinge axes is removed to allow folding. However, this method requires variable-thickness panels, which can be difficult to manufacture. Additionally, the amount of material removed is a function of the final fold angle; as this angle approaches  $\pm 180^\circ$ , more and more material must be removed. In the limit of a fully folded hinge, all material must be removed.

To address the concerns with the volume trimming method, it has been proposed to offset the panels from the hinge axes by means of standoffs [18], as shown in Figure 1.6. The resulting panels have uniform thickness and can be folded fully. However, at many scales, the construction of the

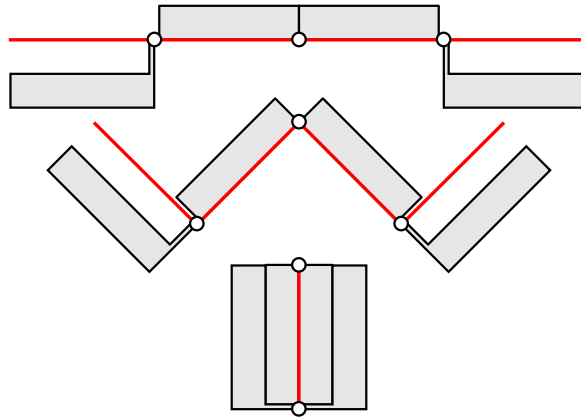


Figure 1.6: Offset panel method for accommodating thickness.

standoffs may be problematic. Additionally, the unfolded structure presents no flat, planar faces.

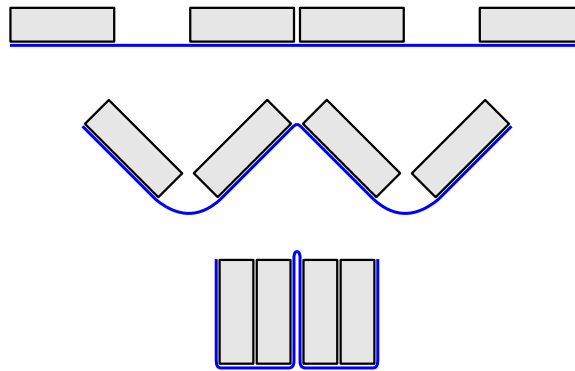


Figure 1.7: Membrane creases for accommodating thickness.

Another approach is to connect thick panels with thinner material, leaving gaps between the thick panels where necessary [9, 19]. This is illustrated in Figure 1.7. This technique introduces additional compliance in the structure, and the structure does not follow the kinematics of a flat origami during folding. Additionally, if in the packaged configuration the folds are not fully closed, there will be some gaps between the edges of the panels. These voids lead to a loss of packaging efficiency.

A variant of this approach is shown in Figure 1.8, and was detailed for flat-foldable origami [20]. This technique replaces the compliant membrane in the fold region by two separate hinges. The relationship between the kinematics of such a mechanism and those of its origami counterpart is poorly understood. Furthermore, this technique, as it currently exists, only applies to flat-foldable origami.

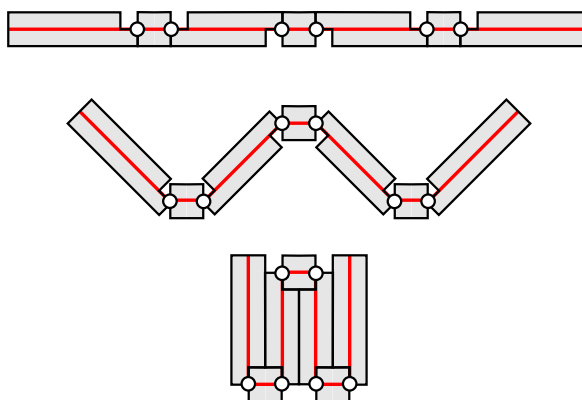


Figure 1.8: Offset creases for accommodating thickness.

In summary, even though there are a variety of origami-like biaxial packaging schemes that account for material thickness in a global sense, accommodating material thickness locally around folds and vertices is challenging, especially if uniform-thickness structures are desired that follow the kinematics of the parent origami pattern.

#### 1.2.4 Cuts and Slits

Packaging of circular thin-shell reflectors using either radial cuts [21, 22] or spiral cuts [23] has been proposed. It was found that a wide range of packaging schemes could be enabled by introducing localized cuts in the structure. However, these cuts and slits produce discontinuities across which tractions cannot be transmitted. These packaging schemes utilize all kinematic degrees of freedom introduced by cutting, and it is challenging to re-establish connectivity between separate pieces after deployment. Some of these schemes have connected edges [21, 22], but the bulk of the structure remains discontinuous, leading to a loss of dimensional stability.

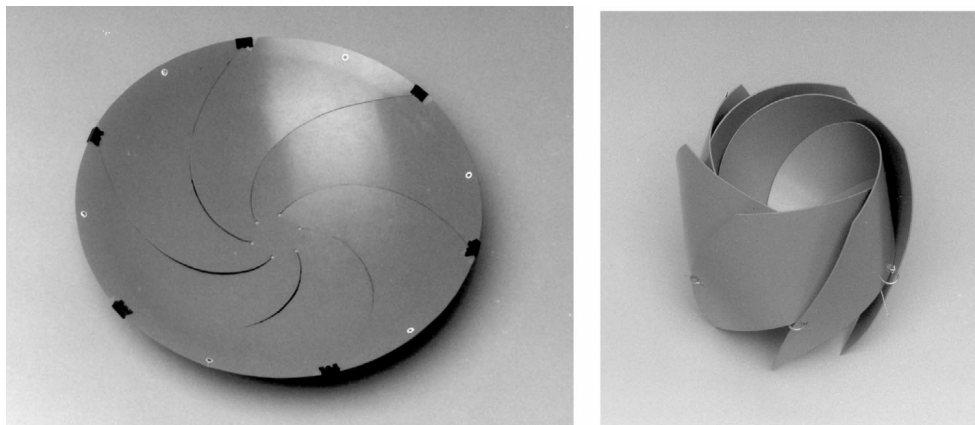


Figure 1.9: Radial spiral cuts used to package a thin shell reflector [21].

## Chapter 2

# Structures with Parallel Slipping Folds

This chapter introduces the concept of slipping folds and describes how planar structures may be biaxially compacted using parallel straight slipping folds. This configuration of slipping folds and this packaging method are compatible with a pretensioning scheme that stabilizes and stiffens the deployed structure; this pretensioning scheme is also discussed. Finally, a method of deploying such structures is described. To validate these concepts for packaging, pretensioning, and deployment, simple experiments were conducted; these experiments and their results are also discussed.

Parts of this chapter were previously published as [24].

### 2.1 Packaging Concept

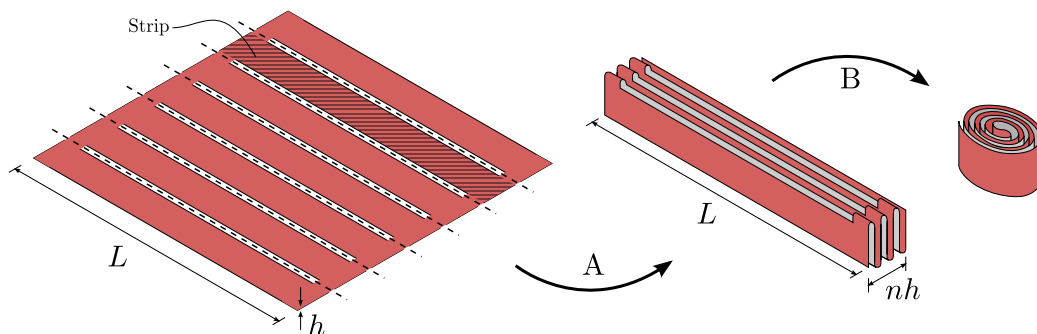


Figure 2.1: The packaging concept consists of two steps: (A) z-folding and (B) wrapping. The square structure is z-folded using  $n - 1$  slipping folds. Then, the resulting stack of  $n$  strips is wrapped in a 2-fold rotationally symmetric fashion. For clarity, only a single strip is shown in the wrapped configuration.

Consider a square planar structure of side length  $L$  and thickness  $h$  as shown in Figure 2.1. The structure is divided into  $n$  strips by  $n - 1$  *slipping folds*. A slipping fold allows rotation about the fold line as well as translation along the fold line, herein called *slip*. In Figure 2.1, the slipping folds

are shown as slits, but there are many ways of realizing slipping folds, as discussed in Section 2.1.1.

The packaging concept, generally called *slip wrapping*, has two steps, each compacting the structure along a single dimension. First, the structure is z-folded using the parallel slipping folds, producing a stack of  $n$  strips. Second, this stack of strips is wrapped in a 2-fold rotationally symmetric fashion. The slipping folds are needed to accommodate the incompatibility created by wrapping the thick strips around different radii, as seen in Figure 2.2. The 2-fold rotational symmetry imposes zero slip at the ends of the wrapped stack, allowing the perimeter of the square to remain continuous.

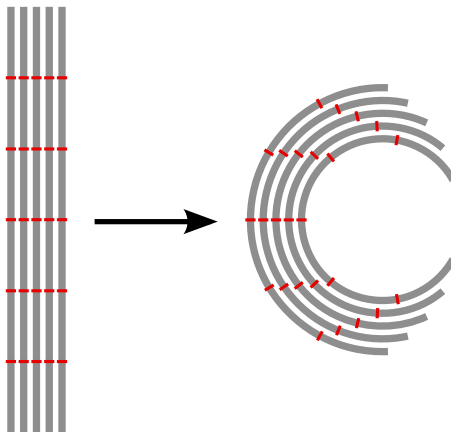


Figure 2.2: Wrapping a stack of thick inextensible strips requires that the strips slip against each other.

The slip degree of freedom is crucial; it enables the second compaction step of wrapping. As shown in Figure 2.2, wrapping the z-folded stack of  $n$  strips leads to the outer strips going around larger radii than the inner strips because each strip has thickness  $h > 0$ . Thus, for the same arclength, outer strips traverse smaller wrapping angles than inner layers. If the strips cannot slip against each other, wrapping the stack of strips will result in straining or micro-buckling.

### 2.1.1 Slipping Folds

The packaging concepts proposed in this thesis rely on slipping folds, which allow rotation about the fold line, as well as translation along the fold line. These two independent kinematic degrees of freedom of a slipping fold are shown in Figure 2.3. Ideal slipping folds allow the structure to be folded and unfolded, and slipped and unslipped at these fold lines without plasticity or damage.

As shown below in Section 2.1.3, the amount of slip needed to package a given structure to a certain level of compaction is finite and can be calculated. As such, a slipping fold is required to provide only a finite amount of slip, and it can be designed to provide the necessary amount of slip.

The simplest realization of a slipping fold involves removing material at a fold line to create a slit; a slit allows for rotation and translation without any material strain. However, it introduces

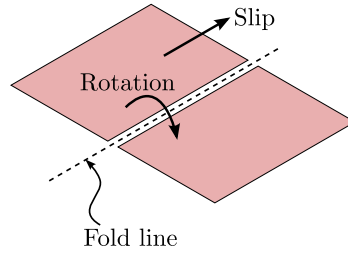


Figure 2.3: Slipping folds have two kinematic degrees of freedom: rotation about and translation along the fold line.

unnecessary degrees of freedom. Realizations of slipping folds have been considered that are not simple cuts, but that include connections that allow for the transmission of tension forces and the limited transmission of shearing forces across fold lines. Figure 2.4 illustrates two possible methods for forming these connections.

**Hinged fold** A cylindrical flexible rod is located at the fold line. This rod is attached to the material on one side of the fold using tabs. The material on the other side is attached to the rod using a loop. This loop can rotate about the rod and slip along the rod. The gaps between the loops and the tabs defines the maximum slip that can be obtained. Tension can be transmitted across the fold line. In the maximum slip state, a shearing force may also be transmitted.

**Ligament fold** To create a ligament fold, one or more thin strips of material are left uncut at the fold line. The length of the ligament is chosen to allow for the required deformation along the fold line. Like the hinged fold, a ligament fold has a state of maximum slip; beyond this state the ligament will deform plastically. A ligament fold allows for the transmission of tension and a limited amount of shear across the fold line.

Whereas hinged folds are more suitable for larger structures where mechanical complexity may be appropriate, ligament folds are useful for developing structures and prototypes at small scales.

### 2.1.2 Volume-Based Model of Wrapping

To develop a mathematical model of the wrapped configuration of the square structure shown in Figure 2.1, assume that in the wrapped state the mid-surface of each strip lies on a generalized cylindrical surface (i.e., a ruled surface spanned by parallel lines, and not necessarily the common case of a *right circular* cylinder). Further assume that the mid-surface of each strip is normally separated from that of its adjacent strip by a constant distance (i.e., the mid-surfaces of the strips are parallel). Nominally, this constant separation distance is the strip thickness  $h$ . Thus, by fixing the shape of the mid-surface of a reference strip, the mid-surfaces of every other strip can be found.

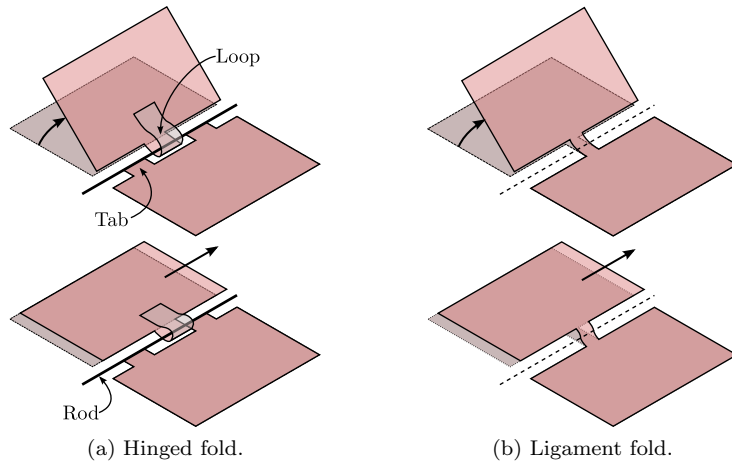


Figure 2.4: Two examples of slipping folds with connections across the fold lines.

Once the configuration of the wrapped strips is known, the amount of slip between them, the maximum strain in the strips, and the overall packaging efficiency can be determined.

The problem of determining the shape of the wrapped structure can be reduced to determining the 2D curve produced by the intersection of the mid-surface of this reference strip and a horizontal plane; this 2D curve is called the *base curve*. In general, a 2D curve produced by the intersection of the mid-surface of a strip and a horizontal plane is said to *trace* that strip. The base curve is parametrized by its arclength  $s$ :

$$\mathbf{r}(s) : [-L/2, L/2] \rightarrow \mathbb{R}^2 \quad (2.1)$$

As shown in Figure 2.5, the strips are indexed by positive integers on one side of the base curve, and negative integers on the other. If  $n$  is odd, the index  $i$  takes on integer values between  $-(n-1)/2$  and  $(n-1)/2$ , and  $i = 0$  corresponds to the central strip and the base curve. If  $n$  is even,  $i$  has integer values between  $-n/2$  and  $n/2$ , and  $i = 0$  corresponds to the base curve, but not a strip. The  $i^{\text{th}}$  strip is traced by a curve  $\mathbf{r}(i; s)$  that is offset from the base curve by  $q(i)\mathbf{n}(s)$ , where  $\mathbf{n}(s)$  is the normal to the base curve and  $q(i)$  is a separation distance:

$$\mathbf{r}(i; s) = \mathbf{r}(s) + q(i)\mathbf{n}(s) \quad (2.2)$$

$$q(i) = \begin{cases} i\phi h & \text{if } n \text{ is odd} \\ i\phi h - \frac{\phi h}{2}\text{sgn}(i) & \text{if } n \text{ is even} \end{cases} \quad (2.3)$$

where  $h$  is the strip thickness, and  $\phi \geq 1$  is strip thickness multiplier that accounts for the fact that in the packaged configuration the mid-surfaces of the strips may be separated by some distance  $\phi h \geq h$ .

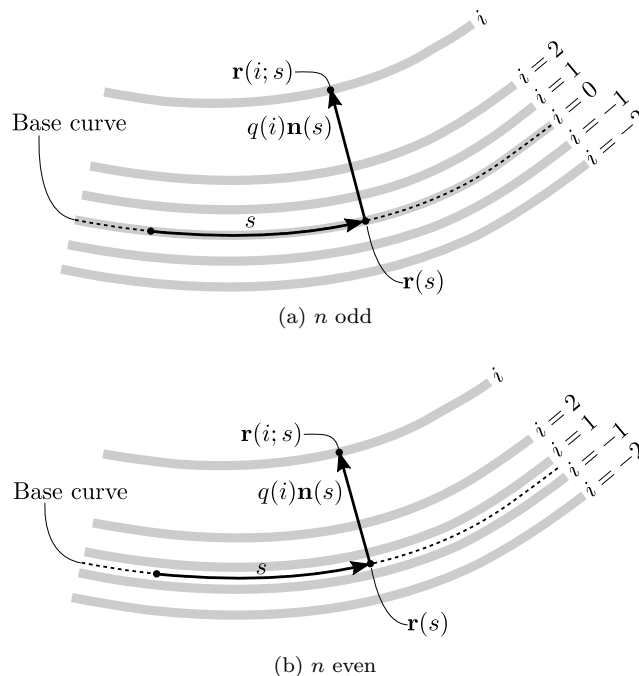


Figure 2.5: The strip mid-surfaces, represented by thick grey lines, have index  $i$  and are uniformly separated from the base curve, shown as the dashed black line.

The slip  $l(i; s)$  between the  $i^{\text{th}}$  and the  $(i+1)^{\text{th}}$  strips is defined to be the difference between the arclengths  $s_i$  and  $s_{i+1}$  of the two strips, at some arclength  $s$  along the base curve.

$$l(i; s) \equiv s_{i+1}(s) - s_i(s) \quad (2.4)$$

The arclength of strip  $i$  has the expression

$$s_i(s) = \int_{s_0}^s \|\mathbf{r}'(i; \tilde{s})\| d\tilde{s} \quad (2.5)$$

where  $s_0$  is a reference point along the base curve, and  $\tilde{s}$  is a dummy variable of integration corresponding to the arclength  $s$ . The magnitude of the tangent vector  $\|\mathbf{r}'(i; s)\|$  is obtained by differentiating Equation (2.2) with respect to the arclength  $s$  and taking the norm:

$$\|\mathbf{r}'(i; s)\| = \|\mathbf{r}'(s) + q(i)\mathbf{n}'(s)\| \quad (2.6)$$

The derivative of the normal vector,  $\mathbf{n}'(s)$ , is parallel to the tangent vector and has length  $|\kappa(s)|$  [25], where  $\kappa(s)$  is the signed curvature of the base curve:

$$\mathbf{n}'(s) = -\kappa(s)\mathbf{r}'(s) \quad (2.7)$$

Substituting this into Equation (2.6) and noting that  $\|\mathbf{r}'(s)\| = 1$  gives

$$\|\mathbf{r}'(i; s)\| = 1 - q(i)\kappa(s) \quad (2.8)$$

Substituting this into Equation (2.4):

$$l(i; s) = [q(i) - q(i + 1)] \int_{s_0}^s \kappa(\tilde{s}) d\tilde{s} = \phi h \int_{s_0}^s \kappa(\tilde{s}) d\tilde{s} \quad (2.9)$$

Note how the slip  $l(i; s)$  between two adjacent strips is independent of the strip index  $i$ . Therefore the design of the slipping folds (e.g., the length of the ligaments) can be the same from strip to strip. (From here on, the slip will be denoted simply as  $l(s)$  without reference to the strip index  $i$ .)

Equation (2.9) provides a definition of slip that depends on the global distribution of curvature; however, it is possible to simplify Equation (2.9) and provide a local definition of slip by noting that

$$\kappa = \frac{d\theta}{ds} \quad (2.10)$$

where  $\theta(s)$  is the tangent angle to the base curve at  $s$ . Thus

$$l(s) = \phi h \int_{s_0}^s \frac{d\theta}{ds} d\tilde{s} \quad (2.11)$$

$$= \phi h [\theta(s) - \theta(s_0)] \quad (2.12)$$

This implies that the slip between two points  $s_0$  and  $s$  is simply proportional to the change in tangent angle (measured continuously) between the two points, and the constant of proportionality is the strip separation  $\phi h$ .

Equation (2.9) is used to determine a condition for having zero slip at both ends of the wrapped square structure described in Section 2.1:

$$\int_{-L/2}^{L/2} \kappa(s) ds = 0 \quad (2.13)$$

A simple way to meet this condition is to have  $\kappa(s)$  be an odd function of arclength, i.e.,  $\kappa(-s) = -\kappa(s)$ . A base curve that has this property may be defined in a piecewise manner, using a *generator curve*  $\mathbf{p}(s) : [0, L/2] \rightarrow \mathbb{R}^2$  and a copy of the generator curve rotated by  $180^\circ$ :

$$\mathbf{r}(s) = \begin{cases} -\mathbf{p}(-s) & \text{if } s \in [-L/2, 0) \\ \mathbf{p}(s) & \text{if } s \in [0, L/2] \end{cases} \quad (2.14)$$

This describes a wrapping with 2-fold rotational symmetry. Thus it is shown that a 2-fold rotationally

symmetric wrapping scheme is a sufficient (though not necessary) condition for having zero slip at both ends of the wrapped stack.

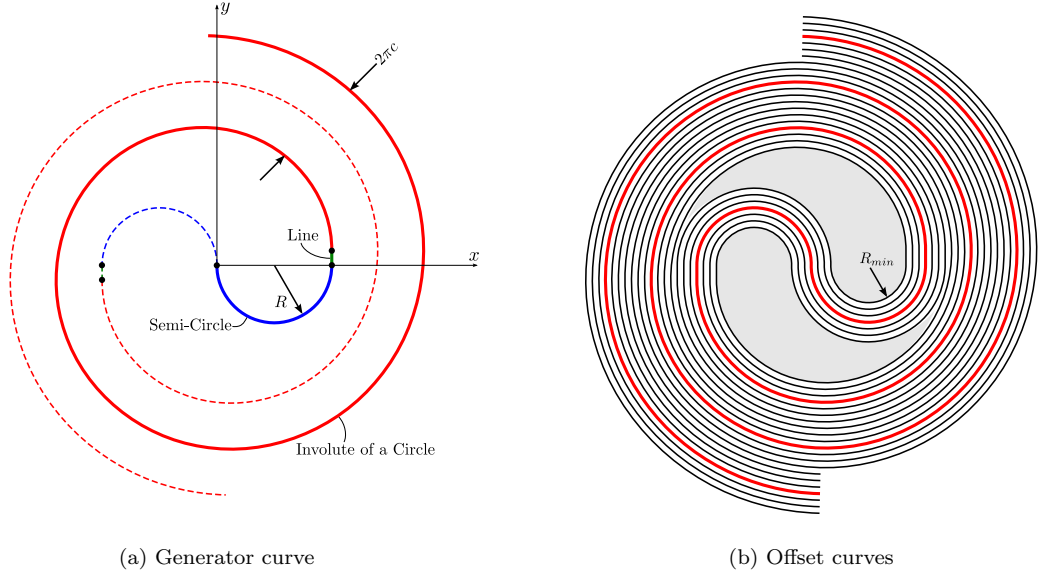


Figure 2.6: Base curve for compact packaging. The shaded areas in (b) are the only voids that result from this curve, and their size depends on the minimum radius of curvature  $R_{min}$ .

A generator curve that allows for compact wrapping is shown in Figure 2.6a as a solid path. It is a piecewise curve consisting of a semi-circle of radius  $R$ , a vertical line of length  $c$ , and an involute of a circle with pitch  $2\pi c$ . As shown in Appendix B, an involute of a circle is a spiral curve with constant normal spacing  $2\pi c = 2n\phi h$  between successive turns. This constant spacing accounts for the thickness of the  $z$ -folded stack of strips. This generator curve is derived in more detail in Appendix C and has the following expression:

$$\mathbf{p}(s) = \begin{cases} R \{1 - \cos(s/R), -\sin(s/R)\} & \text{if } s \in [0, \pi R) \\ R \{2, (s/R) - \pi\} & \text{if } s \in [\pi R, \pi R + c) \\ c \{-\sin(\alpha - \alpha_0) + \alpha \cos(\alpha - \alpha_0), \\ \cos(\alpha - \alpha_0) + \alpha \sin(\alpha - \alpha_0)\} & \text{if } s \in [\pi R + c, L/2] \end{cases} \quad (2.15)$$

$$\alpha^2 = \frac{2}{c}(s - \pi R - c) + \alpha_0^2 \quad (2.16)$$

$$\alpha_0 = \frac{2R}{c} \quad (2.17)$$

$\alpha$  is an angular parameter that is related to the arclength through Equation (2.16);  $\alpha$  parametrizes the involute more simply than the arclength  $s$ .  $\alpha_0$  is the value of  $\alpha$  at the starting point of the involute, where it connects to the vertical line.

It is not expected that a wrapped stack will follow this curve exactly; however, it is a simple curve that may be used to estimate the maximum slip and the packaging efficiency of this concept.

The maximum bending strains in this wrapped configuration occur in the central part of the wrapping. The radius of the semi-circle  $R = R_{min} + \phi hn/2$  can be designed such that the maximum change in longitudinal curvature for an initially flat strip does exceed the limit imposed by, for example, the Tresca yield criterion:

$$R_{min} \geq \frac{Eh}{2\sigma_y(1-\nu^2)} \quad (2.18)$$

where  $E$  is the material modulus,  $\sigma_y$  is the yield stress, and  $\nu$  is Poisson's ratio. Other similar conditions may be formulated based on other failure criteria to ensure that the strip material is not permanently damaged or deformed during packaging.

### 2.1.3 Maximum Slip

For this particular choice of generator curve, the profile of slip for  $s \in [0, L/2]$  can be calculated using Equation (2.9):

$$l(s) = l(0) + \phi h \int_0^s \kappa(\tilde{s}) d\tilde{s} \quad (2.19)$$

Here, the slip at arclength  $s$  along the base curve is calculated with reference to the slip at the origin  $l(0)$ . Recall that the 2-fold symmetry of the base curve ensures that the curvature is an odd function, i.e.,  $\kappa(-s) = -\kappa(s)$ . As such, the slip, which is proportional to the integral of curvature, must be an even function, i.e.,  $l(-s) = l(s)$ . Thus, the slip profile for the other half of the wrapped structure  $s \in [-L/2, 0)$  can be found through this property and Equation (2.19).

To calculate the slip, the curvature of the base curve must be found. The curvature of the semi-circle is simply the inverse of the radius  $1/R$  and the curvature of the line is 0. The curvature for the involute of the circle is calculated in Appendix B. Assembling these pieces together:

$$\kappa(s) = \begin{cases} 1/R & \text{if } s \in [0, \pi R) \\ 0 & \text{if } s \in [\pi R, \pi R + c) \\ 1/[c\alpha(s)] & \text{if } s \in [\pi R + c, L/2] \end{cases} \quad (2.20)$$

Taking the integral with respect to arclength to find the slip:

$$l(s) = l(0) + \phi h \int_0^s \kappa(\tilde{s}) d\tilde{s} = l(0) + \phi h \begin{cases} s/R & \text{if } s \in [0, \pi R) \\ \pi & \text{if } s \in [\pi R, \pi R + c) \\ \alpha(s) - \alpha_0 + \pi & \text{if } s \in [\pi R + c, L/2] \end{cases} \quad (2.21)$$

Figure 2.7a plots an example of the non-dimensional slip profile against the non-dimensional base curve arclength. Note that the slip  $l(0)$  at  $s = 0$  has been chosen to give zero slip at both ends of the wrapped stack. Figure 2.7b provides a visual representation of how the slip, held to be zero at one end of the stack, grows as the stack spirals inwards. At the origin, the curvature of the base curve flips sign, and the slip decreases until it reaches zero again at the other end of the stack.

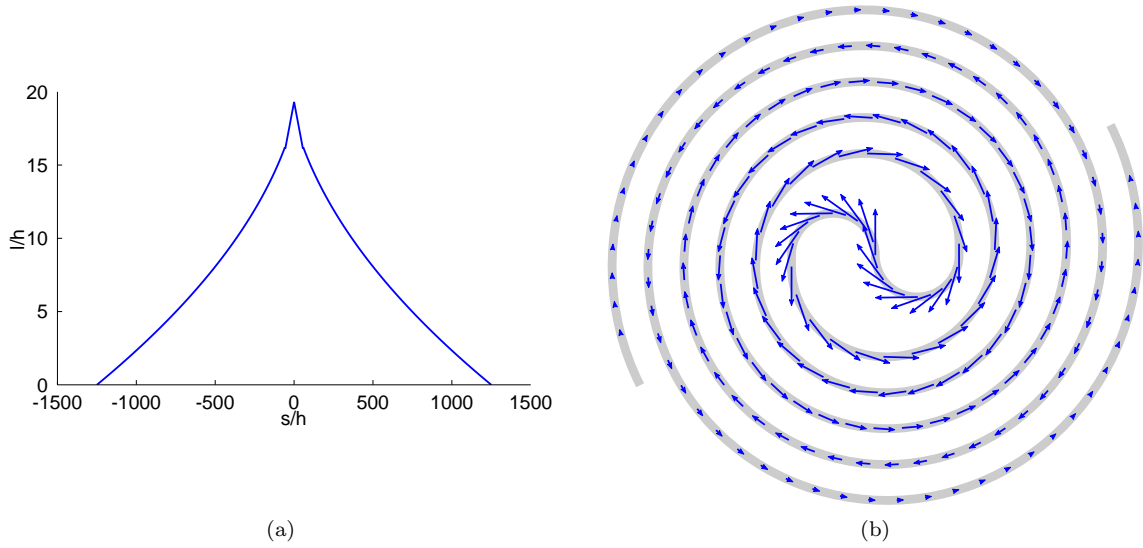


Figure 2.7: (a) plots the slip  $l$  non-dimensionalized by the structure thickness  $h$  against the non-dimensional arclength  $s/h$ . (b) depicts the magnitude of slip over the wrapped stack. The length of the arrows is proportional to the amount of slip.

Since the ends of the wrapped stack are not allowed to slip, the maximum slip  $l_{max}$  occurs at the center of the curve at  $s = 0$ . From Equation (2.21), assuming  $l(L/2) = l(-L/2) = 0$ ,  $|l_{max}| = l(0)$ :

$$|l_{max}| = \phi h (\alpha_{max} - \alpha_0 + \pi) \quad (2.22)$$

Defining the non-dimensional slip  $\chi \equiv |l_{max}|/h$ :

$$\chi = \phi \alpha_{max} - \frac{2\pi\psi}{n} \quad (2.23)$$

$$\alpha_{max}^2 = \frac{\pi\lambda}{n\phi} + \frac{2\pi^2\psi}{n\phi} - 2 + \left(\frac{2\pi\psi}{n\phi}\right)^2 \quad (2.24)$$

where  $\psi$  is the non-dimensional minimum bend radius  $R_{min}/h$ ,  $\lambda$  is the length-to-thickness ratio  $L/h$ , and  $\alpha_{max}$  is the maximum value of  $\alpha$ , obtained by evaluating Equation (2.16) at  $s = L/2$ .

$\lambda$ , the length-to-thickness ratio, is an important parameter. Low values of  $\lambda$  correspond to smaller, thicker structures (e.g., blanket solar power arrays and planar antennas) and high values of  $\lambda$  correspond to bigger, thinner structures (e.g., solar sails and drag sails). In general, the range of values of  $\lambda$  in which aerospace engineers tend to be interested extends from  $\lambda = 10^3$  on the lower end (i.e., structures with  $L \approx 1$  m and  $h \approx 1$  mm) to  $\lambda = 10^7$  (for larger, more conceptual structures with  $L \approx 100$  m and  $h \approx 10$   $\mu$ m).

Figure 2.8 shows plots of the variation of the non-dimensional maximum slip  $\chi$  with the length-to-thickness ratio  $\lambda$  for different values of the number of strips  $n$  and the non-dimensional minimum bend radius  $\psi$ , with the thickness multiplier  $\phi$  held constant.

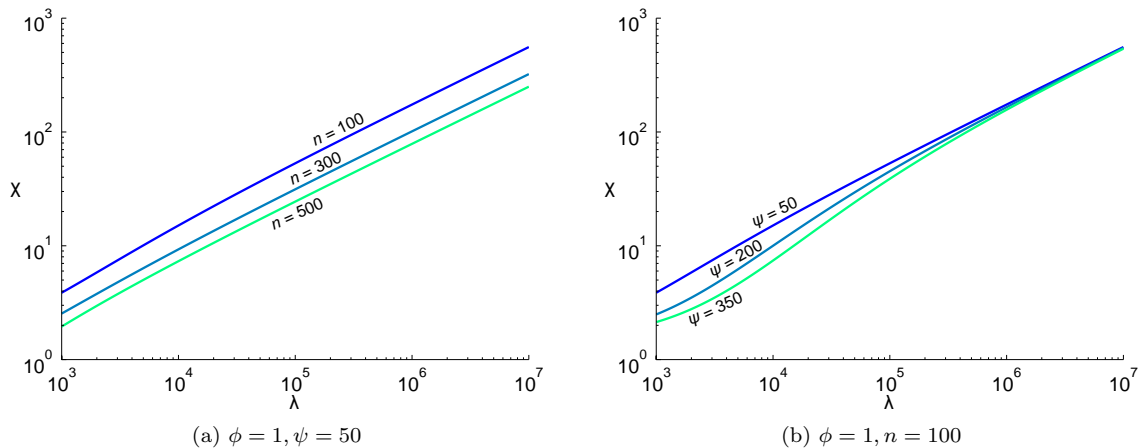


Figure 2.8: Non-dimensional maximum slip  $\chi$  as a function of the dimensionless deployed length  $\lambda = L/h$ , the dimensionless minimum bend radius  $\psi = R_{min}/h$ , and the number of strips  $n$ . For (a),  $\phi$  and  $\psi$  are held constant, and for (b),  $\phi$  and  $n$  are held constant.

As  $\lambda$  grows larger, the first term in Equation (2.24) dominates, and the non-dimensional maximum slip  $\chi$  approaches the following asymptote. As  $\lambda \rightarrow \infty$

$$\alpha_{max}^2 \rightarrow \frac{\pi\lambda}{n\phi} \quad (2.25)$$

$$\Rightarrow \chi \rightarrow \left(\frac{\pi\phi\lambda}{n}\right)^{1/2} \quad (2.26)$$

This result implies that the proposed concept incurs a less-than-proportional increase in non-dimensional maximum slip  $\chi$  as the structure is scaled to higher  $\lambda$ . That is, as the structure grows longer (while keeping constant the thickness), the maximum slip grows as the square root of  $\lambda$ .

### 2.1.4 Packaging Efficiency

The packaging efficiency  $\eta$  is the ratio of the material volume of the structure to the volume of the container into which it is packaged. For this concept, the structure has material volume  $L^2h$  and can be contained within a cylinder of radius  $R_p$  and height  $H_p$ . Thus:

$$\eta = \frac{L^2h}{\pi R_p^2 H_p} \quad (2.27)$$

The packaged height  $H_p$  is taken to be the width of each strip  $H_p = L/n$ . The radius  $R_p$  is the outermost point in the wrapped configuration among any of the strips:

$$R_p = \max_{i,s} \|\mathbf{r}(i; s)\| \quad (2.28)$$

Using Equation (2.2) and Equation (2.3),

$$R_p = \max_{i,s} \|\mathbf{r}(s) + q(i)\mathbf{n}(s)\| \quad (2.29)$$

$$= \max_i \left\| \mathbf{r}\left(\frac{L}{2}\right) + q(i)\mathbf{n}\left(\frac{L}{2}\right) \right\| \quad (2.30)$$

$$= \left\| \mathbf{r}\left(\frac{L}{2}\right) + \frac{1}{2}\phi h(n-1)\mathbf{n}\left(\frac{L}{2}\right) \right\| \quad (2.31)$$

The extremal point along the base curve  $\mathbf{r}(L/2)$  and the normal there  $\mathbf{n}(L/2)$  can be evaluated by considering Equation (2.15). This gives an expression for the packaged radius  $R_p$ :

$$R_p = \phi h \left[ \left(\frac{n}{\pi}\right)^2 + \left(\frac{n\alpha_{max}}{\pi}\right)^2 + \left(\frac{n-1}{2}\right)^2 + \frac{n(n-1)}{\pi}\alpha_{max} \right]^{1/2} \quad (2.32)$$

where  $\alpha_{max}$  is evaluated in Equation (2.24).

Using this, the packaging efficiency can be calculated to have the following expression:

$$\eta = \frac{n\lambda}{\pi\phi^2} \left[ \left(\frac{n}{\pi}\right)^2 + \left(\frac{n\alpha_{max}}{\pi}\right)^2 + \left(\frac{n-1}{2}\right)^2 + \frac{n(n-1)}{\pi}\alpha_{max} \right]^{-1} \quad (2.33)$$

Figure 2.9 shows the variation of the packaging efficiency with  $\lambda$ ,  $\psi$ , and  $\phi$ . The effect of  $n$  on the packaging efficiency is minimal, since as  $n$  increases, the packaged height decreases but the packaged radius increases, and thus the packaged volume varies minimally.

Figure 2.9a shows that the strip thickness multiplier  $\phi$  has the greatest effect on the packaging efficiency for large  $\lambda$ . In fact, in the limit of  $\lambda \rightarrow \infty$ ,  $\eta \rightarrow 1/\phi$ . This means that for very large or very thin structures, the global packaging efficiency depends only on the local, per-strip packaging efficiency. If  $\phi = 1$ , i.e., the strips are packaged together as close as possible everywhere, the

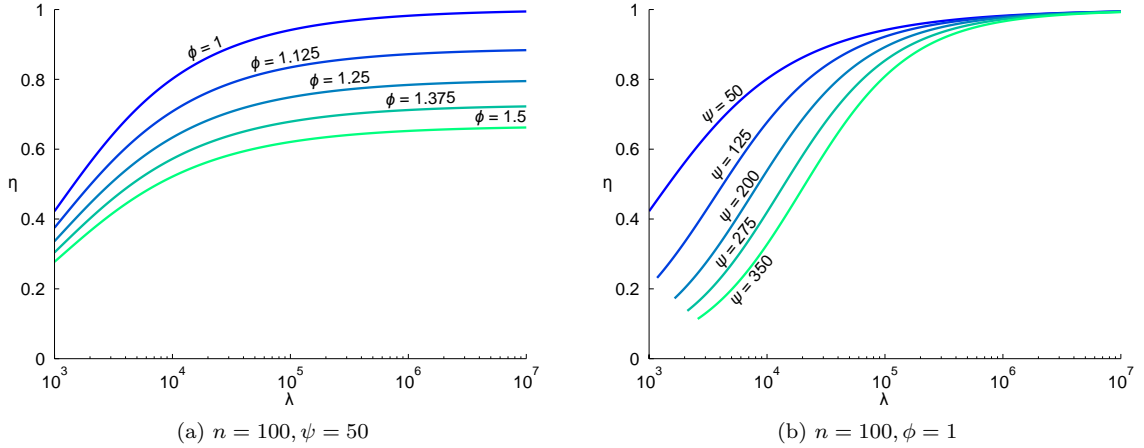


Figure 2.9: Packaging efficiency  $\eta$  as a function of the dimensionless deployed length  $\lambda = L/h$ , the dimensionless minimum bend radius  $\psi = R_{min}/h$ , and the strip thickness multiplier  $\phi$ . For (a),  $n$  and  $\psi$  are held constant, and for (b),  $n$  and  $\phi$  are held constant.

packaging efficiency of this concept approaches 100%.

Figure 2.9b shows that the minimum bend radius of the material  $R_{min} = h\psi$  has the greatest effect for small  $\lambda$ . As  $\lambda$  increases, the size of the two voids (which is determined by  $R_{min}$ ) shown in Figure 2.6 shrinks in relation to the material volume and the effect of  $\psi$  decreases.

### 2.1.5 Compaction Ratio

The compaction ratio compares the packaged dimensions to the deployed dimensions of an unfoldable structure. The compaction ratio and the packaging efficiency are related; whereas the packaging efficiency measures the degree to which a structure occupies its container, the compaction ratio indicates the size of the container.

In the case of uniaxial compaction, the compaction ratio is simply the ratio of the packaged size and the deployed size along the compacted dimension. In the case of biaxial compaction, a compaction ratio  $\zeta$  is proposed:

$$\zeta \equiv \frac{1}{2} \left( \frac{l_1}{L_1} + \frac{l_2}{L_2} \right) \quad (2.34)$$

where  $l_1$  and  $l_2$  are the packaged sizes along the two orthogonal compacted dimensions, and  $L_1$  and  $L_2$  are the deployed sizes. This compaction ratio discriminates between uniaxial and biaxial compaction. In the case of uniaxial compaction (say along the 1-axis),  $0 \leq l_1 < L_1$  and  $l_2 = L_2$ . Therefore, in the case of uniaxial compaction,  $\zeta \geq 0.5$ . Thus, if packaging scheme achieves  $\zeta < 0.5$ , it must compact the structure biaxially.

In the particular case of z-folding and wrapping a square membrane,  $L_1 = L_2 = L$  and  $l_1 = l_2 =$

$2R_p$ . Thus the biaxial compaction ratio is

$$\zeta = \frac{2R_p}{L} \quad (2.35)$$

This compaction ratio can be evaluated in terms of the non-dimensional parameters described in Section 2.1.3:

$$\zeta = \frac{2\phi}{\lambda} \left[ \left(\frac{n}{\pi}\right)^2 + \left(\frac{n\alpha_{max}}{\pi}\right)^2 + \left(\frac{n-1}{2}\right)^2 + \frac{n(n-1)}{\pi}\alpha_{max} \right]^{1/2} \quad (2.36)$$

Figure 2.10 plots this compaction ratio as a function of  $\lambda$  for various values of  $n$  and  $\psi$ . As can be seen,  $\zeta < 0.5$  for almost all plotted values, indicating a degree of compaction unachievable by uniaxial means.

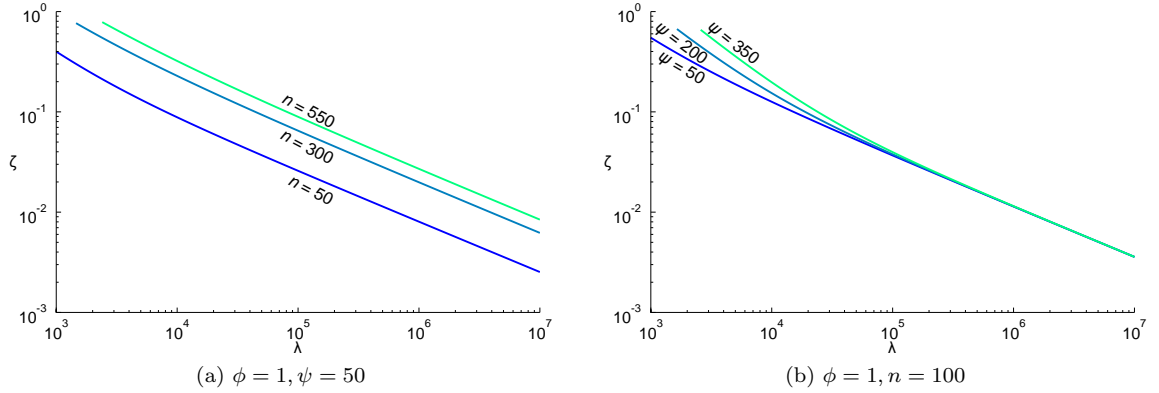


Figure 2.10: Compaction ratio  $\zeta$  as a function of the dimensionless deployed length  $\lambda = L/h$ , the dimensionless minimum bend radius  $\psi = R_{min}/h$ , and the number of strips  $n$ . For (a),  $\phi$  and  $\psi$  are held constant, and for (b),  $\phi$  and  $n$  are held constant.

It is illuminating to evaluate the compaction ratio  $\zeta$  at values of large  $\lambda$ , when the second term in Equation (2.36) dominates. Using Equation (2.25) to evaluate  $\alpha_{max}$  as  $\lambda \rightarrow \infty$ :

$$\zeta \rightarrow \left(\frac{4\phi n}{\pi\lambda}\right)^{1/2} \quad (2.37)$$

### 2.1.6 Combined Elastic and Volume-Based Model of Wrapping

Though the spiral curves used to describe the wrapped configuration are based on an accounting of the finite thickness of the stack of strips, the semicircles are a simple approximation to the equilibrium shape of an unrestrained stack of folded strips in the center of the wrap. Though the stack can be made to follow a semicircular profile by using appropriately shaped guides (as is done in Section 2.1.7), it is useful to know the shape of the stack at the center of the wrap in the absence of such guides.

In this subsection, an alternative model of the wrapped structure will be developed that replaces the semicircles with curves derived from elastica theory. The spiral section of the base curve, however, will be used, since it offers a reasonable volume-based approach to modeling the shape of the wrapped stack.

The problem of finding the elastica-based curve that models the unrestrained interior of the wrapped stack can be posed as follows. Say the stack has been wrapped to follow a semicircular profile using appropriately shaped guides. The outer diameter of this wrapped stack is then held fixed by an external restraint. What shape does the stack take once the wrapping guides are removed? The tightly coiled part of the stack is modeled using an involute of a circle  $\mathbf{p}_v$  with pitch  $2\pi c = 2n\phi h$ :

$$\mathbf{p}_v(\alpha) = c \begin{Bmatrix} \cos \alpha + \alpha \sin \alpha \\ \sin \alpha - \alpha \cos \alpha \end{Bmatrix} \quad (2.38)$$

$$\alpha \in [\alpha_0, \alpha_{max}] \quad (2.39)$$

$\alpha_{max}$  is set by the fixed outer diameter of the wrapping. As shown in Figure 2.11, at point  $A = \mathbf{p}_v(\alpha_0)$ , to be determined, the involute is attached to an elastic rod in bending, while maintaining tangent and curvature continuity. This rod represents the stack of  $n$  strips, and has length  $L_e$ . The profile of this elastic rod is given by  $\mathbf{p}_e(s) : s \in [0, L_e] \rightarrow \mathbb{R}^2$ . By symmetry, the elastica curve must pass through the origin (i.e.,  $\mathbf{p}_e(0) = \{0, 0\} = O$ ) and have zero curvature there (i.e.,  $\kappa_e(0) = 0$ ).

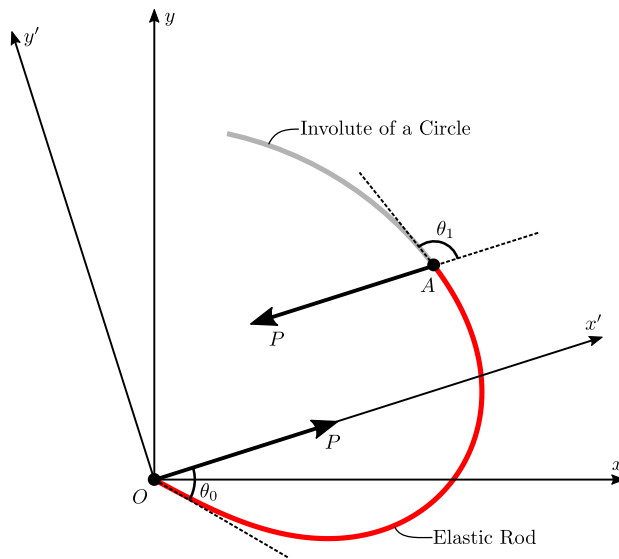


Figure 2.11: A bent rod, or elastica, is used to model to the curve that traces the interior of the wrapped stack. In the rotated frame of reference  $x'y'$ , it is acted on by horizontal end forces  $P$ .

The elastica is loaded by point forces  $P$  at either end and has bending stiffness  $D$ . (Modeling the stack of strips that can slip with respect to each other as a single elastic rod is an approximation that

does not account for the different curvatures of the different strips, or for the contact interactions between the strips.) The equations that describe the shape, angle, and curvature profiles of such a rod in bending are derived in Appendix A. Using those results, and by rotating into a frame where the point forces  $P$  act along the rotated  $x'$ -axis, the following equations are obtained to ensure shape, tangent angle, and curvature continuity between the elastica and the involute of the circle:

$$c(\cos \theta_1 + \alpha_0 \sin \theta_1) = \frac{2}{k} (\mathcal{E}(\omega_1; q) - \mathcal{E}(\pi/2; q)) - L_e \quad (2.40)$$

$$c(\sin \theta_1 - \alpha_0 \cos \theta_1) = -\frac{2q}{k} \cos \omega_1 \quad (2.41)$$

$$q \sin \omega_1 = \sin \frac{\theta_1}{2} \quad (2.42)$$

$$2qkca_0 \cos \omega_1 = 1 \quad (2.43)$$

where  $\theta_1$  is the elastica tangent angle at point  $A$  in the rotated frame of reference, and  $k^2 = P/D$ .  $\mathcal{E}$  is the incomplete elliptic integral of the second kind, and  $\omega_1$  is a transformation variable; both are described in detail in Appendix A. The variable  $q = \sin \frac{\theta_0}{2}$  is defined by the elastica tangent angle at the origin  $\theta_0$ . The length of the elastica is constrained to be  $L_e$ :

$$L_e = \frac{1}{k} (\mathcal{F}(\omega_1; q) - \mathcal{F}(\pi/2; q)) \quad (2.44)$$

where  $\mathcal{F}$  is the incomplete elliptic integral of the first kind, defined in Appendix A.

The length of material available to the elastica is the length of the initially restrained interior portion of the stack (i.e., the length of the semi-circle of radius  $R$  and a line of length  $c$ ), and whatever length is obtained from the involute of the circle by shifting the transition point  $A$  from its original position  $\mathbf{p}(\alpha = 2R/c) = \{2R, c\}$  to its final equilibrium position. Using Equation (2.16) to obtain an expression for this additional length, an expression for  $L_e$  can be found:

$$L_e = \pi R + c + \frac{c}{2} \left( \alpha_0^2 - \left( \frac{2R}{c} \right)^2 \right) \quad (2.45)$$

This equation ensures that the total length of the wrapped stack remains constant, without altering the fixed outer diameter of the packaged structure.

Defining dimensionless variables  $\tau \equiv ck$ , and  $\tilde{\psi} \equiv R_{min}/(\phi nh) = \psi/(\phi h)$ , Equations 2.40 to 2.44

can be non-dimensionalized:

$$\cos \theta_1 + \alpha_0 \sin \theta_1 = \frac{2}{\tau} (\mathcal{E}(\omega_1; q) - \mathcal{E}(\pi/2; q)) - \left( \frac{\alpha_0^2}{2} - \pi^2 \tilde{\psi} - 2\pi^2 \tilde{\psi}^2 + 1 \right) \quad (2.46)$$

$$\sin \theta_1 - \alpha_0 \cos \theta_1 = -\frac{2q}{\tau} \cos \omega_1 \quad (2.47)$$

$$q \sin \omega_1 = \sin \frac{\theta_1}{2} \quad (2.48)$$

$$2q\tau\alpha_0 \cos \omega_1 = 1 \quad (2.49)$$

$$\left( \frac{\alpha_0^2}{2} - \pi^2 \tilde{\psi} - 2\pi^2 \tilde{\psi}^2 + 1 \right) = \frac{1}{\tau} (\mathcal{F}(\omega_1; q) - \mathcal{F}(\pi/2; q)) \quad (2.50)$$

Here, a non-dimensional form of Equation (2.45) has been used to substitute for the non-dimensional length  $L_e/c$ . These five equations have five variables: the elastica end angles  $\theta_0$  and  $\theta_1$ ,  $\alpha_0$ ,  $\omega_1$ ,  $q$ , and  $\tau$ . Given a single parameter  $\tilde{\psi}$ , which is the non-dimensional minimum radius of curvature, these equations can be solved numerically to obtain the elastica shape and curvature profiles.

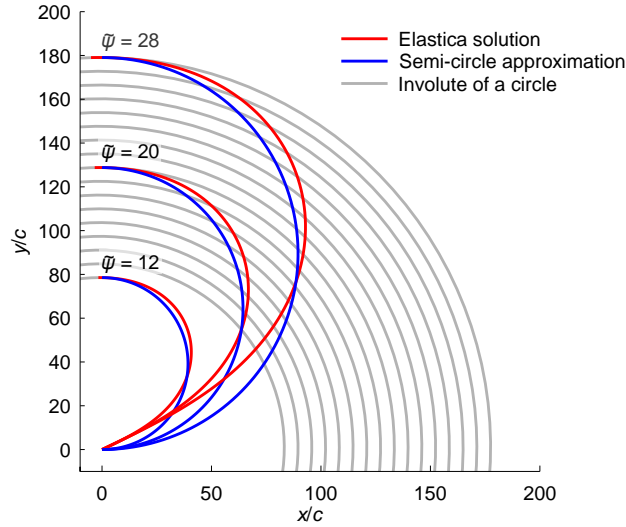


Figure 2.12: The semi-circular approximation compared to an elastica solution for the shape of the wrapped stack in the center, for three different values of the non-dimensional void radius  $\tilde{\psi}$ . The  $x$  and  $y$  axes are non-dimensionalized by parameter  $c = \phi n h / \pi$ .

Figure 2.12 shows the non-dimensional elastica shape profile  $\mathbf{p}_e/c$  for three different values of  $\tilde{\psi}$ . Also plotted are the profiles from the semi-circular approximation. As can be seen, the two profiles are similar. It is also interesting to compare curvature profiles for these two different models. Figure 2.13 plots the elastica curvature  $\kappa_e$  non-dimensionalized by the semi-circular radius  $R$  against the non-dimensional elastica arclength  $s/c$  for a variety of values of  $\tilde{\psi}$ .

As can be seen from Figure 2.13, the bent rod solution has variable radius of curvature, as compared to the constant-curvature approximation of a semi-circle. The elastica curvature vanishes at the origin at  $s = 0$ , reaches a maximum around 1.25 times the void radius  $R$ , and then decreases.

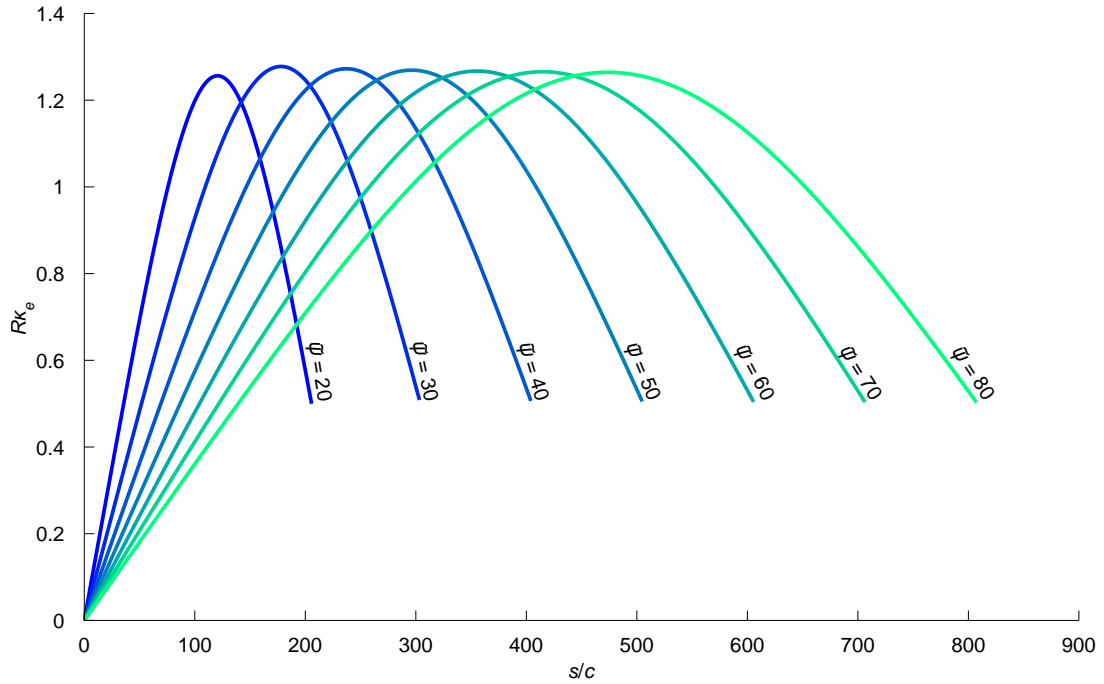


Figure 2.13: Elastica curvature  $\kappa_e$  non-dimensionalized by the semi-circular radius  $R$  for a range of non-dimensional void radii  $\tilde{\psi}$

This result indicates that if a wrapping is done with void radius  $R$  by using appropriately shaped guides, the outer diameter of the wrapping is held fixed, and then the guides are removed, the resulting maximum curvature may be up to 1.25 times the initial void radius  $R$ . Thus, the maximum bending strain may be larger than expected, and the initial void radius must be designed to account for this increase in curvature.

### 2.1.7 Packaging Experiments

To validate the packaging method four test articles were made from commercially available aluminized polyester (Mylar®) films, packaged according to the method, and the packaged shapes were measured. The properties of the test articles are summarized in Table 2.1. The film thicknesses are as specified by the manufacturers.

The slipping folds were implemented using ligaments, which were cut into the membrane substrate using a computer-controlled laser cutter (Universal Laser Systems® ILS9.75). The ligaments had widths of 1.5 mm and lengths of 6.6 mm. Model A4 was too large to be cut as a single piece on the laser cutter; it was cut in two separate parts and then joined together using lengths of Kapton® tape.

Model ID	$h$ ( $\mu\text{m}$ )	$L$ (m)	$\log_{10} \lambda$	$n$	$\psi$	$l_{max}$ (mm)
<b>A1</b>	50.8	0.24	3.67	6	39.4	1.2
<b>A2</b>	50.8	0.50	3.99	13	39.4	1.7
<b>A3</b>	25.4	0.50	4.29	13	78.7	1.1
<b>A4</b>	25.4	0.90	4.55	23	78.7	1.5

Table 2.1: Packaging Test Articles

A set of wrapping guides were made to impose the wrapping profile described in Section 2.1.2. These guides also prevent the strips from exceeding the maximum curvature limit provided by Equation (2.18). Using  $E = 3.50$  GPa,  $\sigma_y = 100$  MPa, and  $\nu = 0.38$  as the material properties [26], Equation (2.18) requires  $R_{min} \geq 1.04$  mm for a 50.8  $\mu\text{m}$ -thick polyester membrane. The guides consisted of two identical pieces, as shown in Figure 2.14, with  $R_{min} = 2$  mm, thereby achieving a margin of 2 against plastic deformation. The two pieces were fabricated from UV-curable acrylic plastic using stereolithography. A lengthwise hole in each piece was used to assemble the guides with end plates and threaded rods. Each piece also had small pegs at either end that mate with the two end plates. These end plates held the two guides in alignment.

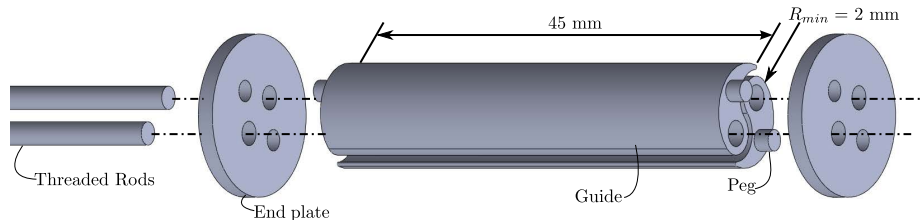


Figure 2.14: Wrapping guides.

To test the packaging scheme, the four models were first folded into a stack of strips. The strips were then pre-slipped with respect to each other at the middle of the stack by the amounts indicated in Table 2.1. This pre-slip was calculated from Equation (2.22) and induced before the stack was inserted into the guides. When packaging without guides, this step of pre-slipping is not required,

since the strips are free to slip during packaging. However, since the guides tightly clamp the strips against each other and hence prevent slip from developing during wrapping, it was necessary to pre-slip the strips.

The strips were then manually wrapped tightly around the guides. A loop of string was used to hold the structure wrapped, see Figure 2.15, while a digital caliper was used to measure the maximum diameter of the cylindrical package at the middle of the wrapped stack, i.e., away from the ligaments and close to the restraining string. The height of the package was taken to be the strip width, which neglects any vertical shift of the individual strips due to uneven folding. Figure 2.15 shows model A2 wrapped around the guides.



Figure 2.15: Model A2 wrapped around the guides. The packaged diameter was 23.9 mm.

From the packaged dimensions and the known material volumes, the respective packaging efficiencies were calculated, and the results are plotted in Figure 2.16. The highest packaging efficiency achieved experimentally was 83% for model A4. Also plotted in Figure 2.16 are four curves generated using the mathematical model presented in Section 2.1.4 with the same  $n$  and  $\psi$  values as the four models, and a value of  $\phi$  for which the curve passes through the experimental point. These lines represent packaging efficiencies achievable using similar manufacturing and packaging techniques to those used in the present study, but scaled to different values of  $\lambda$ .

Since the experimental models had been wrapped tightly and without gaps, a thickness multiplier  $\phi \approx 1$  was expected. For the two thinner models A3 and A4 with  $h = 25.4 \mu\text{m}$ , the experimentally obtained values of  $\phi = 1.057$  and  $1.043$  confirmed this expectation. The other two measurements, with  $\phi = 1.139$ , and  $\phi = 1.106$  were obtained from the thicker models ( $h = 50.8 \mu\text{m}$ ), which indicates that manual packaging with small gaps is more difficult to achieve for thicker and hence stiffer models.

This trend indicates a need for method of more systematic and controlled packaging. A mechanical apparatus, such as the one proposed by Lanford [27], that maintains dimensional stability of the membrane during wrapping by inducing a degree of tension in the unwrapped membranes, would be beneficial. The design of such a jig, however, is outside the scope of this thesis.

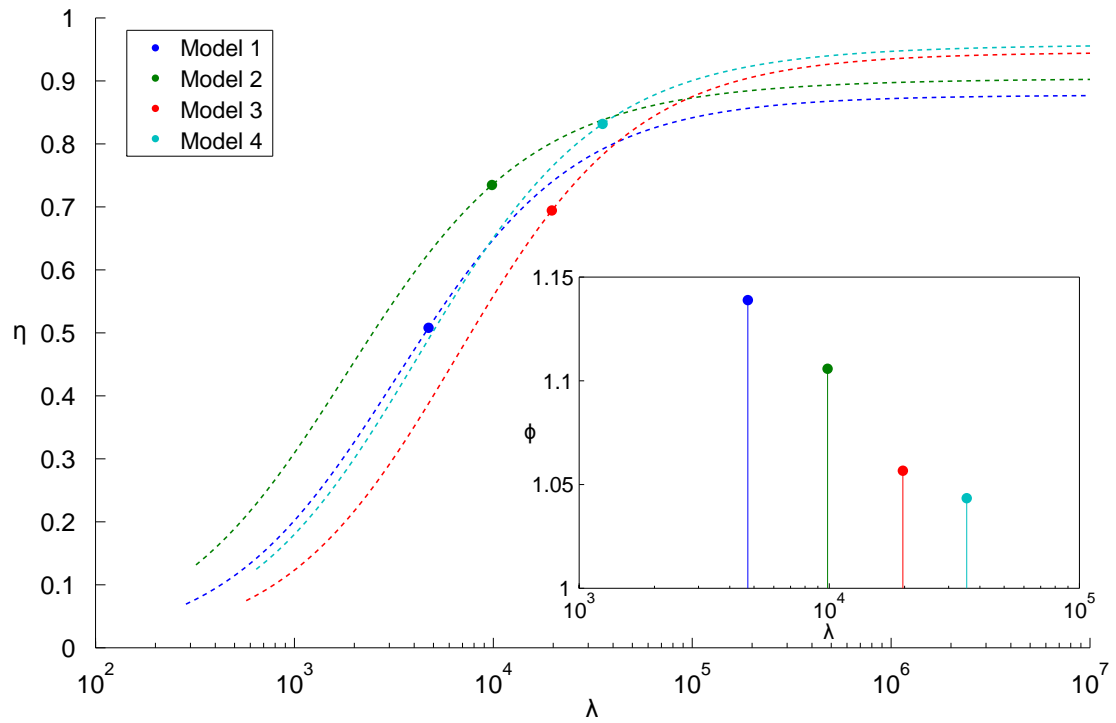


Figure 2.16: Packaging test results for z-folded and wrapped membrane test articles. The points represent experimentally measured packaging efficiencies, and the dashed lines are predictions from the mathematical model with the value of  $\phi$  chosen to pass through the experimental points. The chosen values of  $\phi$  are plotted in the inset.

## 2.2 Pretensioning with Scalloped Edges

The z-fold and wrapping scheme presented in Section 2.1 enforces zero slip along the edges of the structure, and therefore, these edges be made continuous, stiff, and able to transmit tension without excessive deflection. By shaping the edge profile, this edge tension can be used to induce a uniform prestress in the inner part of the structure. This approach is a variation of a standard approach in the design of suspension bridges [28]. This pretensioning approach is particularly useful when the structure has small out-of-plane bending stiffness, as in the case of membranes, and needs to be pretensioned to be stabilized.

Consider the structure shown in Figure 2.17, with slipping folds parallel to the  $y$ -axis, and lengths  $L_a$  along the  $x$ -axis and  $L_b$  along the  $y$ -axis. It is desired that each strip has uniform pretension in the  $y$ -direction, i.e., parallel to the slipping folds, and no pretension in the  $x$ -direction, i.e., perpendicular to the slipping folds. (This neglects the ability of the slipping folds to transmit tension.)

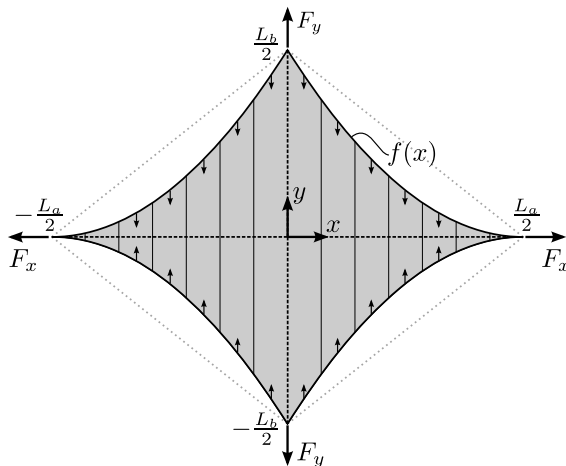


Figure 2.17: A structure with parabolic edges, loaded by pairs of diagonal forces at the corners, is subject to uniform uniaxial tension per unit width.

Consider applying corner tensioning forces  $F_x$  at  $[\pm L_a/2, 0]$  and  $F_y$  at  $[0, \pm L_b/2]$  (using suitable external compression members, e.g., booms or masts), as shown in Figure 2.18. It is desired to induce a uniform uniaxial tension per unit width  $P$  in each strip, acting in the  $y$ -direction. The appropriate edge profile for the top-right quadrant is a parabola:

$$f(x) = \left(\frac{P}{F_x}\right)x^2 - \left(\frac{PL_a}{2F_x} + \frac{L_b}{L_a}\right)x + \frac{L_b}{2} \quad (2.51)$$

$$x \in [0, L_a/2] \quad (2.52)$$

The remaining edges of the membrane can be defined by reflections of  $f(x)$  through the  $x$  and  $y$  axes. To ensure  $f(x) \geq 0$  over  $x \in [0, L_a/2]$ , the slope at  $x = L_a/2$  must satisfy the condition

$f'(L_a/2) \leq 0$ , and hence

$$\frac{PL_a}{2F_x} - \frac{L_b}{L_a} \leq 0 \quad (2.53)$$

This particular parabolic edge profile produces the desired tension distribution only in the limit of inextensional materials, and does not account for the changes in geometry due to the extension of the strips or the edges. Therefore, it is only valid for low extensions for real materials.

Additionally, strips under pure uniaxial tension will be subject to transverse compression due to Poisson effects. If this compression is sufficiently large, it will lead to transverse buckling of strips. As such, this formulation is only valid in the asymptotic case of large  $n$ , when the structure is sufficiently anisotropic. This architecture will need to be modified, for example by shaping the edges of the strips to reduce compressive stresses [29], to be applicable to structures with low values of  $n$ .

The loading ratio  $\sigma \equiv (PL_a/2F_x)$  and the aspect ratio  $\gamma \equiv (L_b/L_a)$  are the non-dimensional parameters that control this design. Of interest are the membrane area  $A$  normalized by the rhombus area  $(L_aL_b/2)$ , denoted  $\rho \equiv 2A/L_aL_b$ , and the corner force ratio  $F_y/F_x$ . These are given by:

$$\rho = 1 - \frac{\gamma\sigma}{3} \quad (2.54)$$

$$\frac{F_y}{F_x} = \sigma + \gamma \quad (2.55)$$

Figure 2.18 shows a plot of the dimensionless area  $\rho$  as a function of the loading ratio  $\sigma$  and the aspect ratio  $\gamma$ . Since the deployed area cannot exceed the area of the bounding rhombus,  $\rho \leq 1$ . In fact,  $\rho = 1$  (i.e., the structure occupies the entirety of the bounding rhombus) requires  $\sigma = 0$  (i.e., the strips are unstressed).

Scalloped edges have been previously used to distribute edge loads to tension membranes [30, 29]. However, the presence of slipping folds, which result in a membrane that has in-plane stiffness that is much higher parallel to the fold lines than perpendicular to the fold lines, requires and admits a tensioning solution wherein the membrane tension is oriented in one direction only.

### 2.2.1 Pretensioning Experiment

A single model was made, using the same materials and techniques as described in Section 2.1.7, to test the pretensioning concept. It had a thickness of 50.8  $\mu\text{m}$ , lengths  $L_A = L_B = 0.8 \text{ m}$ , and 18 strips. The ligaments had lengths of 1.0 mm and widths of 4.0 mm. The parabolic edge profile was chosen to provide a loading ratio of  $\sigma = 1$  (and since the aspect ratio  $\gamma = 1$ , Equation (2.53) is satisfied). For these parameters, Equation (2.55) gives a force ratio  $F_y/F_x = 2$ .

Figure 2.19 shows the model hanging on a metal-backed chalkboard using magnets. The ten-

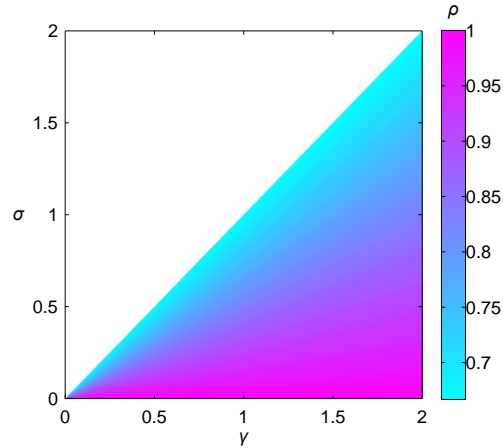


Figure 2.18: Structure area normalized by rhombus area  $\rho = 2A/L_aL_b$  as function of the aspect ratio  $\gamma = L_b/L_a$  and the loading ratio  $\sigma = PL_a/2F_x$ . The upper triangular region is inaccessible because of Equation (2.53).

sioning forces were applied by hanging weights:  $F_y$  was applied by hanging a 50 g weight from the bottom corner and holding the top corner of the membrane with a pin and  $F_x$  was applied through a pulley by hanging a 25 g weight and pinning the right corner of the membrane.

Inspection of this model showed that each strip was in a state of tension, and that the model was hanging flat. Some transverse curvature of the strips was observed, which could be due to the film having been stored on a roll (though that could be avoided by starting from a membrane with no initial curvature) or from transverse compression from Poisson effects.

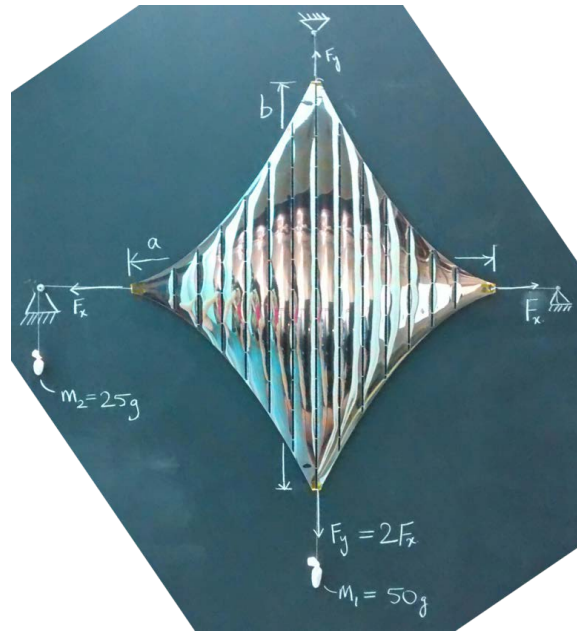


Figure 2.19: Hanging model test of prestressing concept.

## 2.3 Deployment of Structures with Parallel Slipping Folds

Figure 2.20 shows a two-stage deployment concept for a slip-wrapped structure with scalloped edges. The deployment process consists of an unwrapping stage followed by an unfolding stage.

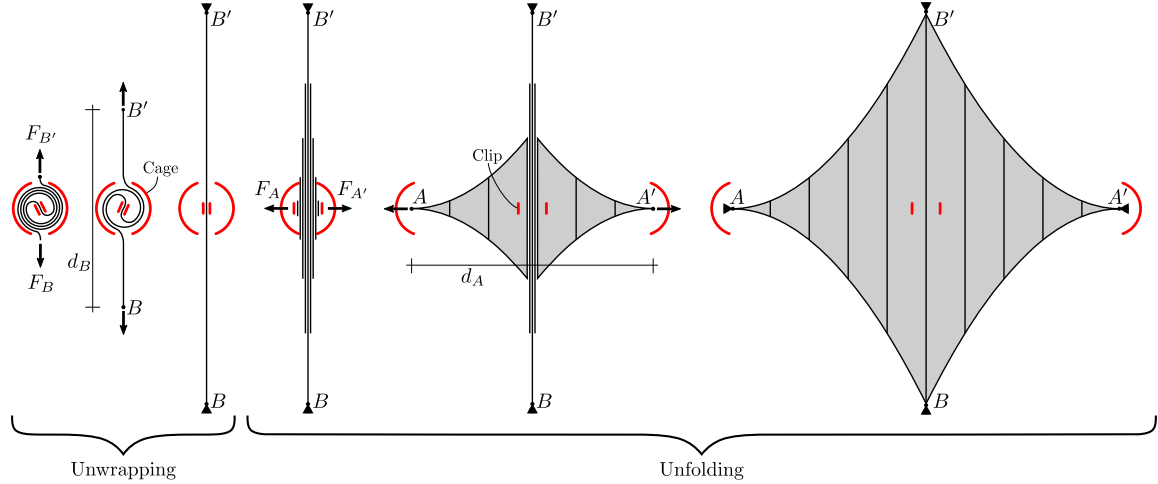


Figure 2.20: Two stages of deploying a slip-wrapped structure with parabolic edges. For clarity, only one strip is shown for the unwrapping stage.

In the unwrapping stage, the two ends  $B$  and  $B'$  of the wrapped stack are pulled in opposite directions by applying forces  $F_B$  and  $F_{B'}$ . The separation  $d_B$  between  $B$  and  $B'$  increases until  $d_B = L_B$ . In the unfolding stage, the stack of strips is unfolded by applying forces  $F_A$  and  $F_{A'}$  at points  $A$  and  $A'$ . The separation  $d_A$  between these points increases until  $d_A = L_A$ , at the end of deployment.

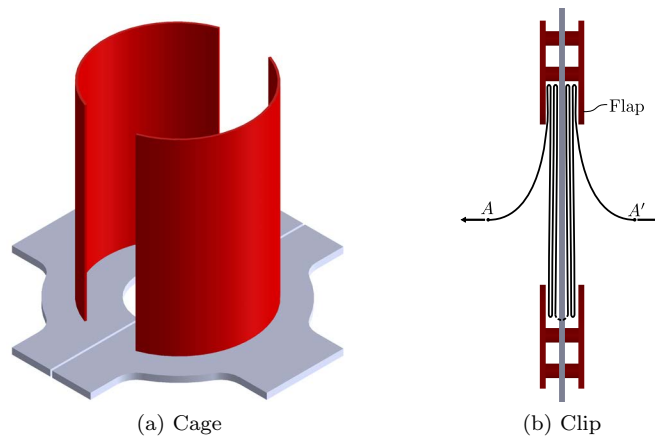


Figure 2.21: Components of deployment restraint concept.

The deployment restraint system consists of two elements, the cage and the clip, shown in Figure 2.21. The two-part cage, Figure 2.21a, is used to control the unwrapping process. The endpoints

$B$  and  $B'$  of the packaged stack are pulled out through two slots in the cage. During the unfolding stage, the two halves of the cage separate and move apart, as shown in Figure 2.20. The clip, shown in Figure 2.21b, holds together the folded stack of strips, at its midpoint. It consists of four thin flaps that manage the unfolding stage; when the endpoints  $A$  and  $A'$  of the folded stack are pulled apart, the flaps bend elastically and allow only a single strip to deploy at a time. Note that the wrapped structure rotates with respect to the cage during the unwrapping stage, and hence the clip has to rotate as well.

### 2.3.1 Estimating Deployment Forces

The first stage of the deployment process, the unwrapping stage, is dominated by the frictional sliding of the stack against the cage. There are also frictional interactions between the strips as they slip against each other. A simple model of the unwrapping stack can be obtained by modeling the wrapped stack as an elastic rod of uniform cross-section, i.e., assuming that all strips have equal length, as shown in Figure 2.22. It is assumed that the  $n$  strips in the stack are overlapped, and hence follow the same curve, hence the geometrical effects of strip thickness are neglected.

Each strip has modulus  $E$ , Poisson's ratio  $\nu$ , width  $w$ , and thickness  $h$ , leading to a stack bending stiffness of

$$D = nE \frac{wh^3}{12(1 - \nu^2)} \quad (2.56)$$

that is uniform over the length of the rod.

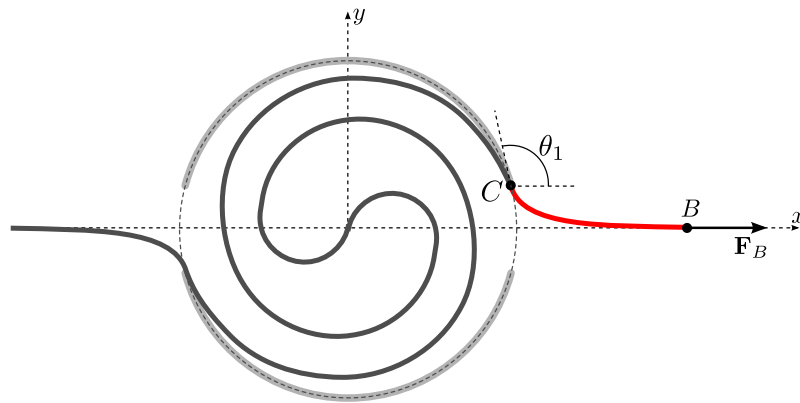


Figure 2.22: Unwrapping model.

The stack is pulled at point  $B$  by a horizontal concentrated force  $\mathbf{F}_B = \{F_B, 0\}$ , parallel to the  $x$ -axis. It is assumed that no moments are applied at point  $B$ , to satisfy moment equilibrium for the free body comprising the membrane stack and the cage. The stack exits the cage at point  $C$ , where the cage applies an equal and opposite force  $\mathbf{Q} = -\mathbf{F}_B$ . A non-zero internal bending moment at

point  $C$  ensures moment equilibrium of the arc  $BC$ , highlighted in red in Figure 2.22.

At point  $C$ , the slope of the rod is denoted by  $\theta_1$  (note that the rod may not be tangent to the cage at this point), such that the rod-normal component  $Q_N$  and the rod-tangent component  $Q_T$  of  $\mathbf{Q}$  are related through the coefficient of friction  $\mu$ , and hence

$$Q_T = \mu Q_N \quad (2.57)$$

Taking components of the forces acting at  $C$ :

$$\|\mathbf{Q}\| \cos(\pi - \theta_1) = \mu \|\mathbf{Q}\| \sin(\pi - \theta_1) \quad (2.58)$$

and solving for  $\theta_1$

$$\theta_1 = \pi - \tan^{-1} \left( \frac{1}{\mu} \right) \quad (2.59)$$

The problem of finding the profile of the unwrapping force can be posed as follows: given the location of points  $B = \{x_B, 0\}$  (determined by the imposed motion of point B) and  $C = \{x_C, y_C\}$  (determined by the design of the slot in the cage), the bending stiffness  $D$  of the rod, find  $F_B$  such that the tangent angle is  $\theta_1$  at  $C$  and the bending moment at point  $B$  is zero. This is a standard elastica problem; its solution is derived in Appendix A:

$$y_C = \frac{2}{k} q \cos \phi_1 \quad (2.60)$$

$$x_B - x_C = \frac{1}{k} [\mathcal{F}(\phi_1; q) - \mathcal{F}(\pi/2; q)] - \frac{2}{k} [\mathcal{E}(\phi_1; q) - \mathcal{E}(\pi/2; q)] \quad (2.61)$$

where  $\mathcal{F}(\phi; q)$  is the incomplete elliptic integral of the first kind, and  $\mathcal{E}(\phi; q)$  is the incomplete elliptic integral of the second kind.  $q$ ,  $\phi_1$ , and  $k$  are defined as follows:

$$q = \sin \left( \frac{\theta_2}{2} \right) \quad (2.62)$$

$$\sin \phi_1 = \frac{1}{q} \sin \left( \frac{\theta_1}{2} \right) \quad (2.63)$$

$$k^2 = \frac{F_B}{D} \quad (2.64)$$

where  $\theta_2$  is the tangent angle of the rod at  $B$ .

Equation (2.60) and Equation (2.61) can be solved numerically for a range of values of  $x_B$  to obtain  $k$  as a function of  $x_B$ . Then, the variation of  $F_B$  over the unwrapping process can be found using Equation (2.64).

Figure 2.23 plots the predictions of this model in a non-dimensional form, for various values of the coefficient of friction  $\mu$ . The model predicts an initial smooth ramp up in force, followed by a plateau

as the amount of total curvature in the bent stack approaches an asymptote, thus requiring less additional work. The model predicts higher values of this force plateau as the coefficient of friction decreases; this is because the tangent angle,  $\theta_1$ , at point  $C$  increases with increasing coefficient of friction,  $\mu$ , and at high values of  $\theta_1$ , the stack needs to bend less to accommodate the boundary conditions. This model does not account for the final stages of unwrapping; when the stack is almost fully unwrapped, the contact between the stack and the cage at point  $C$  is lost, and the unwrapping force drops. This particular model described above cannot capture this behavior.

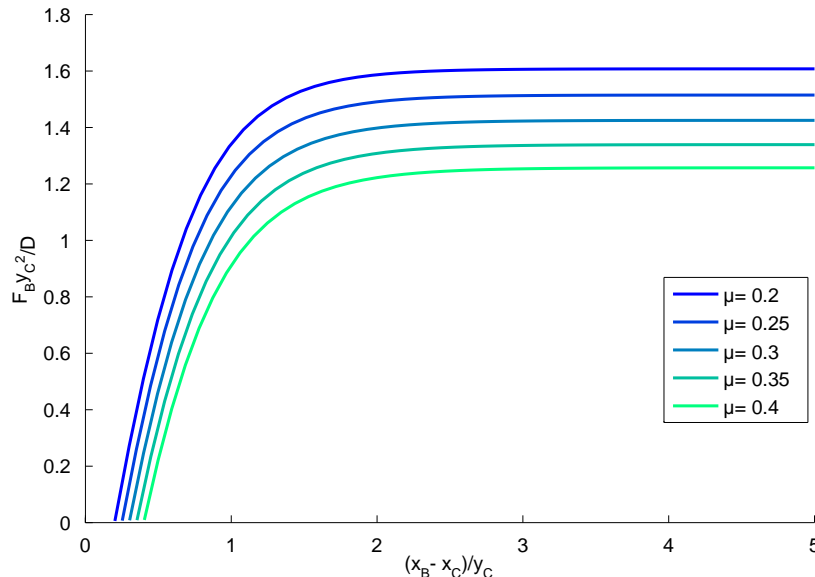


Figure 2.23: Non-dimensional unwrapping force  $F_B y_C^2 / D$  with respect to non-dimensional deployment parameter  $(x_B - x_C) / y_C$ .

Turning to the second stage of the deployment process, the deployment force  $F_A$  is mainly due to the elastic deformation of the clip; its magnitude increases as each strip is pulled out and suddenly decreases when the clip deformation is sufficiently large.  $F_A$  can be estimated from the simple two-dimensional model in Figure 2.24, where the strips are modeled as inextensible tension elements of equal length connected by frictionless pin joints. The strips are held in the packaged configuration by two elastic cantilevers that represent the flaps. The thickness of the strip is small with respect to the deployed dimensions, and hence for simplicity it is neglected in the following analysis.

There are two different configurations of this model, depending on whether the strips that have been previously released are slack, and hence  $F_A = 0$ , Figure 2.25(a), or taut, in which case  $F_A \geq 0$  and the flap is deformed, until a maximum amount of deformation is reached and the hinge  $i + 1$  is released; Figure 2.25(b).

Define as  $d_{A,i}$  the specific value of  $d_A$  that corresponds to the instance when  $F_A$  first becomes non-zero after the release of hinge  $i$ . This is the situation shown in Figure 2.25(b). From Figure

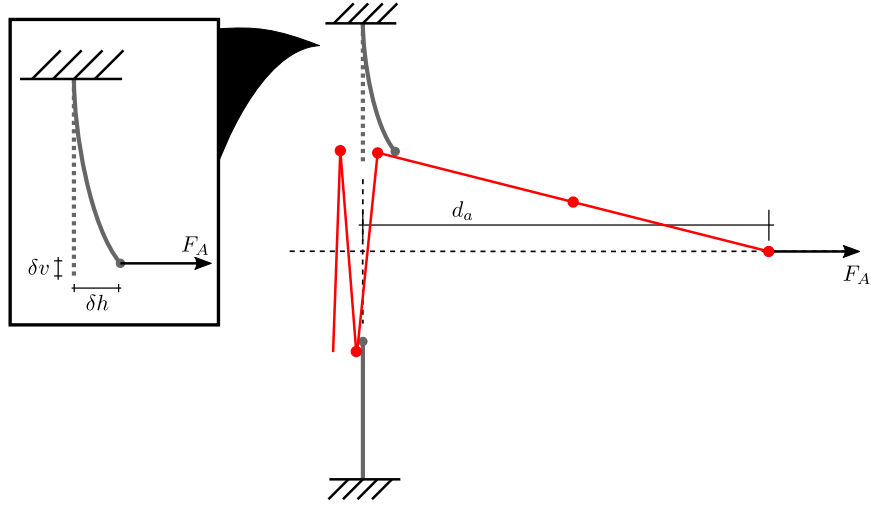


Figure 2.24: Model to analyze deployment force  $F_A$  during unfolding process.

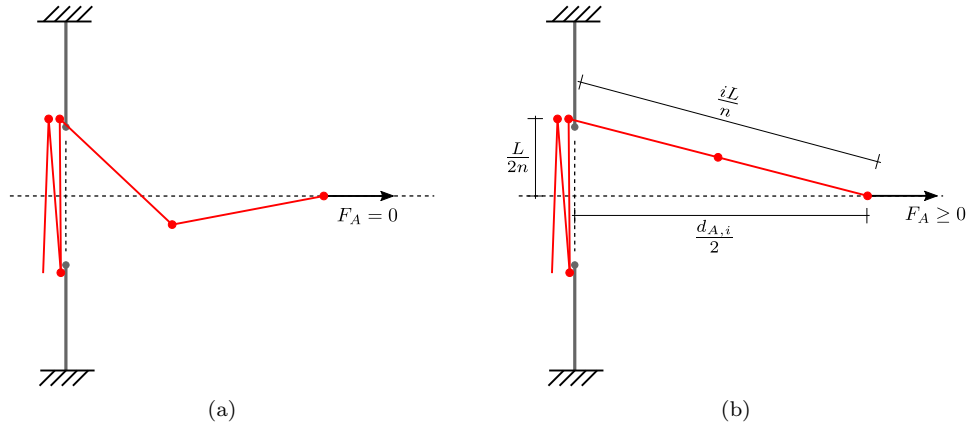


Figure 2.25: The two configurations of the unfolding model: (a) when the previously released strips are slack and  $F_A = 0$ , and (b) when the strips are taut and  $F_A \geq 0$ .

2.25(b),  $d_{A,i}$  can be determined from Pythagoras' theorem:

$$\left(\frac{d_{A,i}}{2}\right)^2 + \left(\frac{L}{2n}\right)^2 = \left(\frac{iL}{n}\right)^2 \tag{2.65}$$

The condition for hinge  $i + 1$  to snap out is that the vertical deflection of the tip of the flap,  $\delta v$ , due to a tip of force of  $F_A$  becomes equal to the initial overlap,  $L_o$ , between the clip and the hinge. The vertical and horizontal deflections of the flap  $\delta v$  and  $\delta h$  can be calculated as a function of the applied force  $F_A$  by treating the flap as an inextensional elastic rod. Using the equations that

describe the behavior of such rods from Appendix A:

$$\delta h = -\frac{2}{k} [\mathcal{E}(\phi_1; q) - \mathcal{E}(\pi/2; q)] - L_f \quad (2.66)$$

$$\delta v = \frac{2}{k} q \cos \phi_1 \quad (2.67)$$

Given a value of  $F_a$ ,  $k$  can be calculated from:

$$k^2 = \frac{F_a}{D} \quad (2.68)$$

The deflected length of the flap is constrained to remain equal to  $L_f$ :

$$L_f = -\frac{1}{k} [\mathcal{F}(\phi_1; q) - \mathcal{F}(\pi/2; q)] \quad (2.69)$$

$\phi_1$  is defined as in Eq. 2.64, with the value of  $\theta_1$  set to be  $\pi/2$  because the flap is held vertical at the root:

$$\sin \phi_1 = \frac{1}{q} \sin \left( \frac{\theta_1}{2} \right) = \frac{1}{q} \sin \left( \frac{\pi}{4} \right) \quad (2.70)$$

$q$  can be found by solving Eqs 2.69 and 2.70. Once  $q$  has been found,  $\delta v$  and  $\delta h$  can be calculated from Eqs 2.66 and 2.67.

This model predicts a sawtooth-like force profile: a series of smooth ramps up followed by sharp decreases in force as the flap disengages from the hinges. Figure 2.26 shows the evolution of a non-dimensional unfolding force  $F_A L_f^2 / D_f$  with respect to the deployment fraction  $d_A / L$  for a particular choice of model parameters.

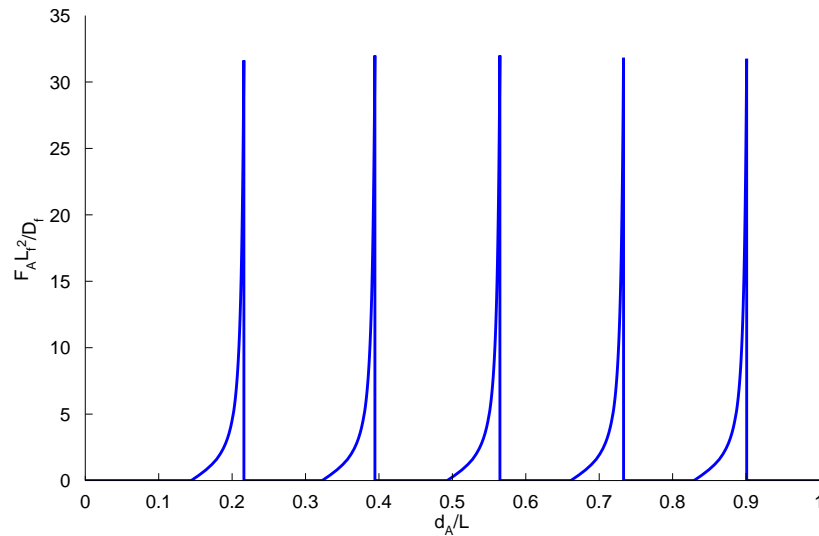


Figure 2.26: Non-dimensional unfolding force  $F_A L_f^2 / D_f$  as a function of deployment fraction  $d_A / L$ .

### 2.3.2 Deployment Experiments

A deployment test model was made using the same materials and techniques as described in Section 2.1.7. This model had scalloped edges, with a loading parameter of  $\sigma = 1$  and an aspect ratio of  $\gamma = 1$ . It was made with 25.4  $\mu\text{m}$ -thick Mylar<sup>®</sup>, had diagonal lengths  $L_A = L_B = 1.00$  m, and 26 strips. The ligaments had widths of 1.0 mm and lengths of 4.3 mm. The model was laser-cut as three separate pieces that were spliced together using Kapton<sup>®</sup> tape.

The deployment test apparatus shown in Figure 2.27 was used to test the deployment concept. The apparatus consisted of four independent linear actuators to provide the deployment forces  $F_B, F_{B'}, F_A, F_{A'}$ , four force sensors to measure these deployment forces, and a suspension system to partially offload the mass of the membrane.

Each linear actuator consisted of a lead screw (with a pitch of 2.54 mm) coupled to a stepper motor that drives a carriage back and forth along a rail. Each stepper motor (1.8° full step size) was driven by a microstepping driver (Allegro<sup>TM</sup>4988 driving the motor with 1/4 steps). A microcontroller (Arduino Leonardo based on an Atmel<sup>®</sup> ATmega32u4) synchronized the four motors, as well as providing logic, displacement data logging, and an interface to a laptop personal computer. One 1/4 step (corresponding to a motion of 0.003 175 mm) was taken every 500  $\mu\text{s}$ . Slight microcontroller delays led to a carriage speed of 5.93  $\text{mm s}^{-1}$ . The motion of each carriage was controlled in open-loop based on the number of steps commanded.

A six-axis force sensor (ATI Industrial Automation Nano17) was mounted on each carriage, to measure the components of the deployment force with a resolution of 3.1  $\mu\text{N}$ . Moment components were also measured by the sensor, but these measurements were not used.

Note that the model was not packaged as tightly as in the packaging tests. That is, it was packaged with a larger minimum radius of curvature  $R_{min}$  than dictated by Equation (2.18) and with gaps between layers. This is because the wrapping guides could not be included in this test; they would have to be removed before the unfolding stage, thus introducing mechanical complexity to the experiment. It is possible that a tightly packaged structure will deploy differently than a loosely packaged structure. The effect of packaging tightness on the deployment behavior warrants further experimentation.

Figure 2.28 shows the cage, with inner diameter of 37 mm and height of 49 mm, and the clip that were used for the deployment tests. The cage consisted of two laser-cut acrylic base plates, two 127  $\mu\text{m}$ -thick polyimide plates elastically bent into semicylinders by means of threaded rods that also attached the semicylinders to the base plates. The cage was constructed in two halves, which separate during the unfolding stage of the deployment. The inner faces of the semicylinders were coated with a spray-on PTFE-based dry lubricant (Saint-Gobain Fluoroglide<sup>®</sup>) to reduce friction between the cage and the membrane during unwrapping. The location of the edge of the cage in relation to its center was measured to be  $x_c = 19.6$  mm,  $y_c = 4.0$  mm.

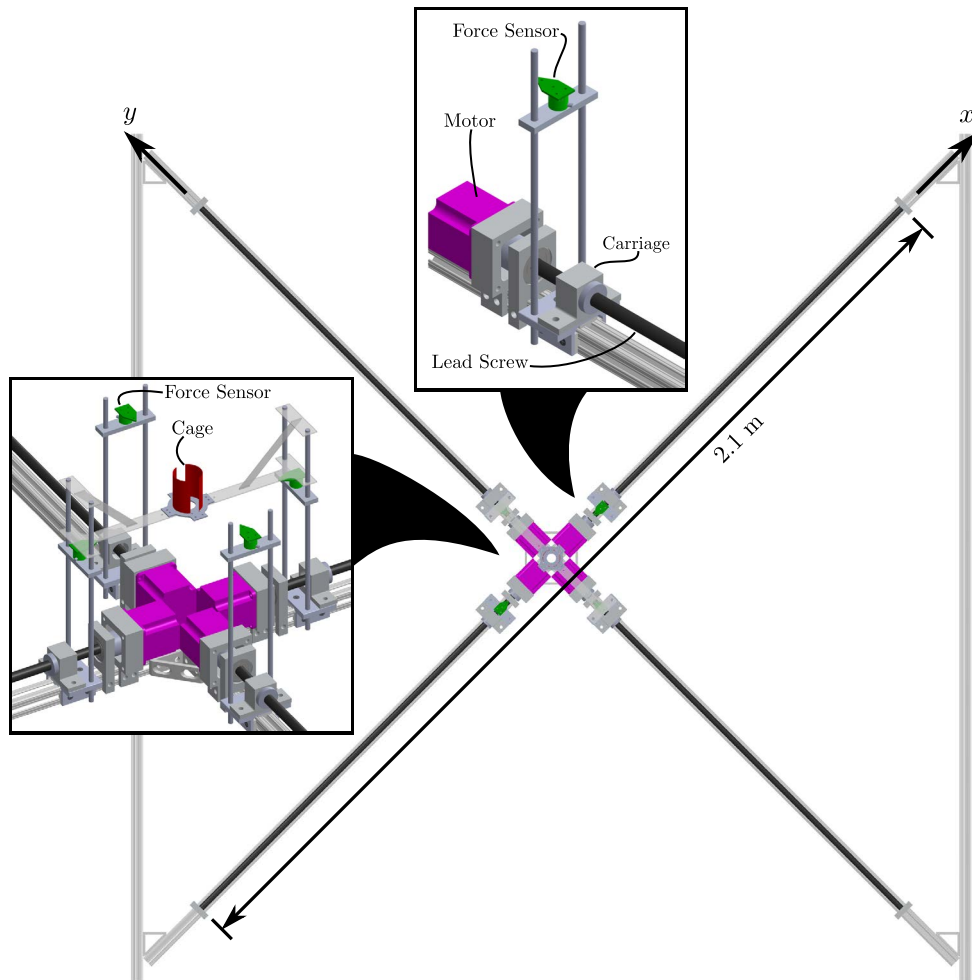


Figure 2.27: Two-axis deployment rig.

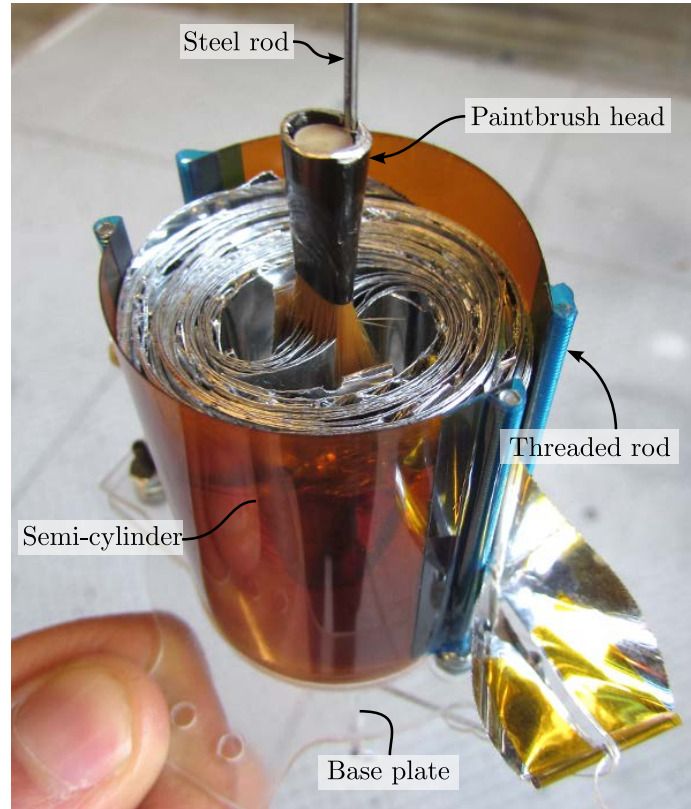


Figure 2.28: Membrane model, wrapped and inserted into the cage. The cage had a diameter of 37 mm and a height of 49 mm.

The clip was made using two paintbrush heads ( $7\text{ mm} \times 4\text{ mm}$  cross section, 11 mm length) connected by a steel rod. The paintbrush bristles were pushed into the wrapped membrane stack, introducing a small spacing between the membrane strips. This ensured that the membrane strips would deploy one by one.

The membrane was deployed horizontally, minimizing the effects of gravity by suspending the clip about 0.25 m above the base of the two-axis deployment rig. Since the clip holds the middle of the membrane during most of the deployment, suspending the clip helped offload some of the weight of the membrane. A 400 g weight was suspended from the bottom of the clip to stabilize its orientation.

The deployment was displacement controlled at a rate of about  $11.9\text{ mm s}^{-1}$ , which was chosen to avoid significant dynamic effects while achieving a full deployment in about 4 minutes.

The average deployment forces,  $(F_B + F_{B'})/2$  and  $(F_A + F_{A'})/2$ , measured during a single deployment are plotted in Figure 2.29 with respect to the unwrapping fraction  $b_d/L_b$  and the unfolding fraction  $a_d/L_a$ . As can be seen, the radial component of the deployment forces is dominant: the in-plane transverse deployment forces were about 20 times smaller than the radial force component, and the out-of-plane deployment forces were about 4 times smaller than the radial forces.

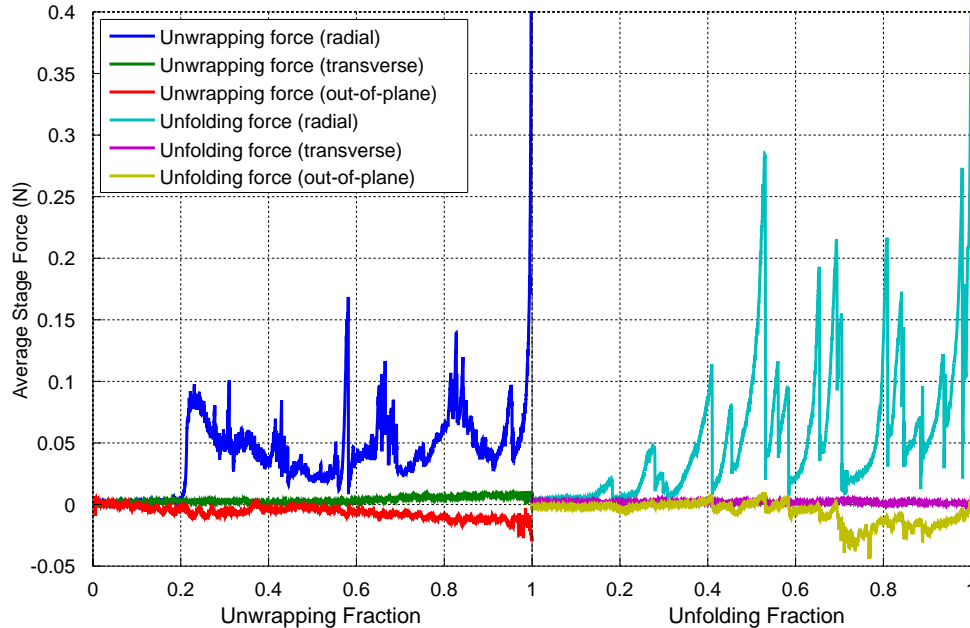


Figure 2.29: Deployment force profiles. During the first stage of unwrapping, the unfolding fraction is fixed at 0, and during the second stage of unfolding, the unwrapping fraction is fixed at 1.

Figure 2.30 plots the radial component of the average deployment forces  $(F_B + F_{B'})/2$  and  $(F_A + F_{A'})/2$  measured during three separate deployments, along with the predicted deployment forces, computed using the models presented in Section 2.3.1.

For the unwrapping force prediction, the elastic modulus was chosen as  $E = 3.5$  GPa, Poisson's ratio was  $\nu = 0.38$ , the coefficient of friction was  $\mu = 0.25$ . The elastic properties are from the manufacturer's specification [26].

The coefficient of kinetic friction between an aluminized Mylar<sup>®</sup> film (the model material) and a Kapton<sup>®</sup> film treated with the a PTFE-based dry lubricant (the material of the cage walls) was measured in a separate experiment. In brief, a disc of aluminized Mylar<sup>®</sup>, glued to a known mass, was dragged over a PTFE-treated flat Kapton<sup>®</sup> sample. This was done using one of the linear actuators described above, and the dragging forces were measured by the one of the force sensors described above. The coefficient of kinetic friction was extracted based on the force measurements and the known mass.

The unfolding force predictions use a clip length  $L_c = 11$  mm, and a clip overlap  $L_o = 8$  mm. The clip length was measured; the clip overlap was estimated. In generating the predicted unfolding force profile, a different clip bending stiffness  $D$  was used for each snap. This is because the clip in the experiment was a paintbrush, and the number of paintbrush bristles engaged with the fold increased with each snap.

Figure 2.30 shows that both the unwrapping and the unfolding force predictions capture both the overall trends in the experimentally measured data in magnitude, and in the case of the un-

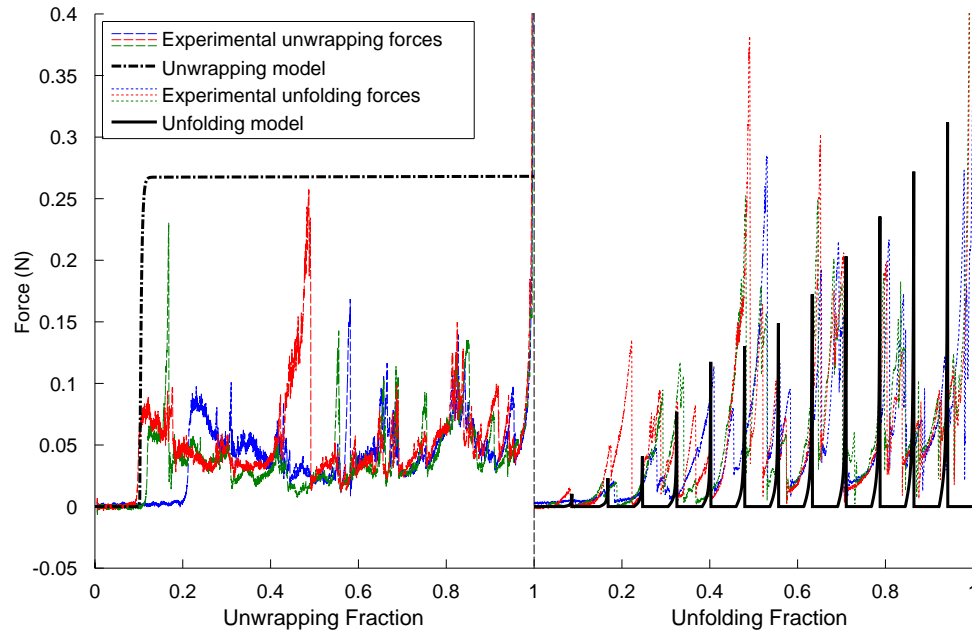


Figure 2.30: Experimentally measured deployment forces and model predictions.

folding stage, character. The good match between predictions and experiments suggests that the mechanisms underlying these models (that is, friction and stack bending for the unwrapping stage and clip bending for the unfolding stage) were indeed dominant during the deployment experiments.

There are many physical effects not captured by these simple mechanical models. These effects include gravity, contact and sliding between the strips, the non-uniform bending stiffness of the folded stack, the snagging of the folded ligaments against each other or the cage walls, and variations in the elastic and geometric properties of the crude clips. It is expected that these unmodeled effects account for some of the discrepancies between the predicted and measured deployment forces.

Figure 2.31 shows views from an overhead camera at the beginning of deployment, at the end of the unwrapping stage, during the unfolding stage, and at the end of the deployment. Controlled deployment was observed for each of the three deployments plotted in Figure 2.30.

## 2.4 Summary

In this chapter, a novel packaging scheme for structures of finite thickness has been proposed. This scheme divides the structure into parallel strips connected by slipping folds, and uses specially chosen base curves for the wrapping profile in order to avoid slippage along the outer edges of the structure. It has been shown that a highly efficient packaging can be achieved, and also that continuity of the structure along the edges can be maintained.

For structures with high length-to-thickness ratios, the packaging efficiency of this concept ap-

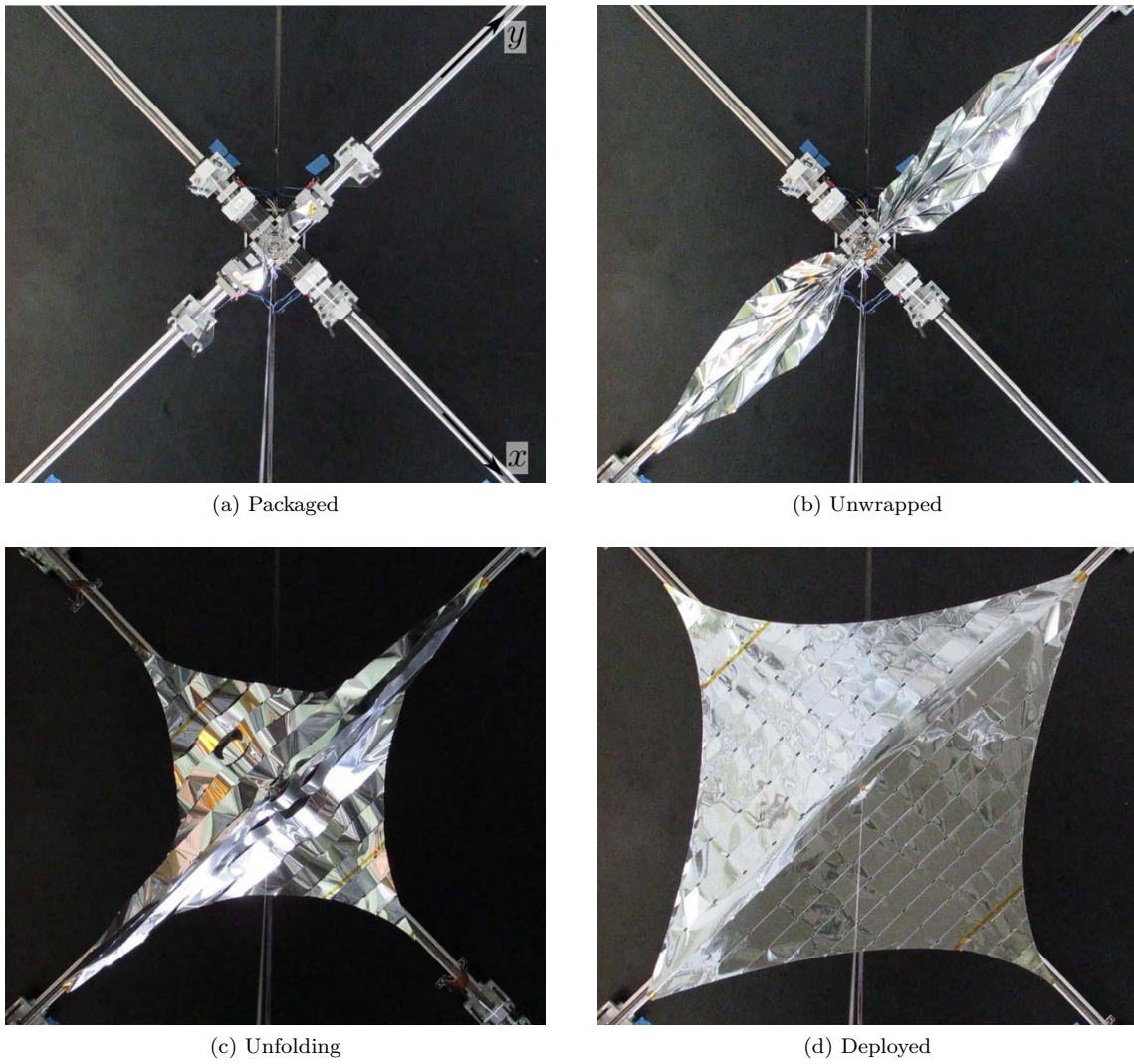


Figure 2.31: Deployment test for a membrane with  $L_a = L_b = 1$  m,  $h = 25$   $\mu$ m viewed from an overhead camera.

proaches 100%. Packaging tests on meter-scale models were conducted, and packaging efficiencies of up to 83% were demonstrated at this scale.

In the packaged configuration, the strips are pre-slipped by specific amounts and are then bent smoothly around the chosen wrapping profile. This approach avoids plastic deformations of the structure, and hence, after deployment, the structure can recover its initial shape.

A scheme to apply uniform uniaxial prestress to the deployed structure has also been proposed, suitable for membrane structures. This prestressing concept exploits the edge continuity of the structure to create a catenary-like boundary that equilibrates the internal pretension. This approach requires curved edges which, depending on the required level of pretension, results in a reduction in the available surface area.

A two-stage deployment process, in which the stacked strips are first unwrapped and then unfolded, has also been proposed, analyzed in detail, and demonstrated experimentally. It has been shown that the deployment is well controlled and that the corner forces required to deploy the structure can be estimated analytically.

## Chapter 3

# Polygonal Structures with Slipping Folds

The concept of slip wrapping can be applied to additional fold patterns; this chapter describes its application to a family of fold patterns known as *star folds* [31] where the folds are arranged in concentric polygons. A mathematical model is developed to describe the packaged configuration and predict packaging efficiencies. Two structural architectures are discussed; the first uses pretension to stabilize the deployed structure and the second relies on strip bending stiffness.

The structures described in this chapter have two key advantages over those discussed in Chapter 2: these structures have straight edges (and can be used to tile 2D planes and build larger arrays) and they admit structural architectures that reduce deployed area lost to scalloping.

Portions of this chapter were previously published as [32].

### 3.1 Packaging Concept

A star fold pattern, an example of which is shown in Figure 3.1, consists of two kinds of folds: 1) folds arranged as  $n - 1$  concentric regular  $N$ -sided polygons, alternating between mountains and valleys; and 2) folds that run along the diagonals of the polygons that also alternate between mountains and valleys. This fold pattern exhibits  $N$ -fold symmetry. The folds along the diagonals divide the structure into  $N$  *sectors*, each of which is a copy of its neighbor, rotated through an angle of  $\beta = 2\pi/N$ . In each sector, the fold pattern divides the membrane into  $n$  strips. The structure has side length  $L$ , with a polygonal hole in the center with side length  $L_0$ . The hole side length  $L_0$  is given by the following geometric relation:

$$L_0 = L - 2nw \tan \frac{\beta}{2} \tag{3.1}$$

where  $w$  is the width of each strip. Since the hole side length  $L_0$  has bounds  $0 \leq L_0 \leq L$ , the strip width  $w$  has corresponding bounds  $L/(2n \tan \frac{\beta}{2}) \geq w \geq 0$ .

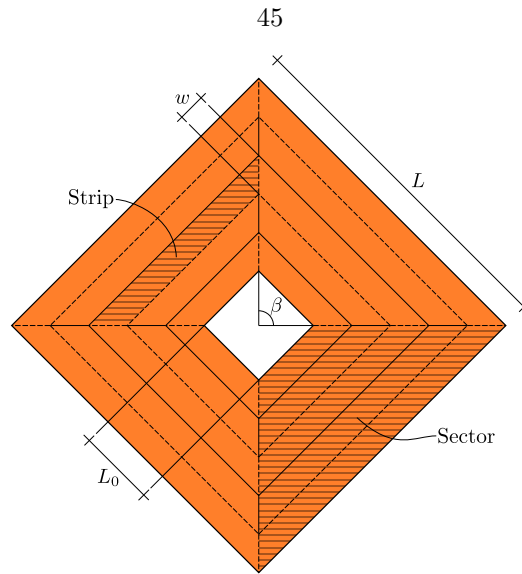


Figure 3.1: Star fold pattern for  $N = 4$  and  $n = 5$ . Mountain folds are shown as solid lines, and valley folds as dashed lines. The structure has side length  $L$ , central hole side length  $L_0$ , uniform strip width  $w$ , and sector angle  $\beta$ .

Folding along the fold lines produces a star-like shape with  $N$  arms, as shown in Figure 3.2a. Then, since the fold pattern is implemented with slipping folds, these arms can be wrapped around each other, resulting in a compact packaged cylindrical form, as shown in Figure 3.2b. There are  $N + 1$  voids in the packaged form; one in the center, and one associated with each wrapped arm.

Neither the folding nor the subsequent wrapping is novel. The fold pattern itself has been described and studied for the case of  $N = 4$  [33], and it was used, with  $N = 4$ , along with the wrapping step, to package the IKAROS solar sail [34]. Additionally, the stripped solar sail design [35] used an architecture consisting of strips arranged in concentric squares, and this architecture was realized as a physical model by [36]. However, the compact packaging of this structure was not considered.

The key innovative step here is the use of slipping folds to implement this fold pattern, which allows for compact wrapping. Without slipping folds, this method of packaging does not accommodate the thickness  $h$  of the material. Slipping folds allow for adjacent strips to slide past each other, accounting for the different radii of the strips in the wrapped configuration.

### 3.1.1 Volume-Based Model of Wrapping

Consider the configuration of the structure after folding but before wrapping, as depicted in Figure 3.3a. The intersection of a horizontal plane and the mid-surfaces of the strips produces a set of 2D curves that trace the location of every strip after folding. (To say that a curve “traces” the location of a strip is to say that the curve is the intersection of the mid-surface of the strip and a horizontal plane.) Similar curves that trace the strips after wrapping can be used to describe the fully packaged

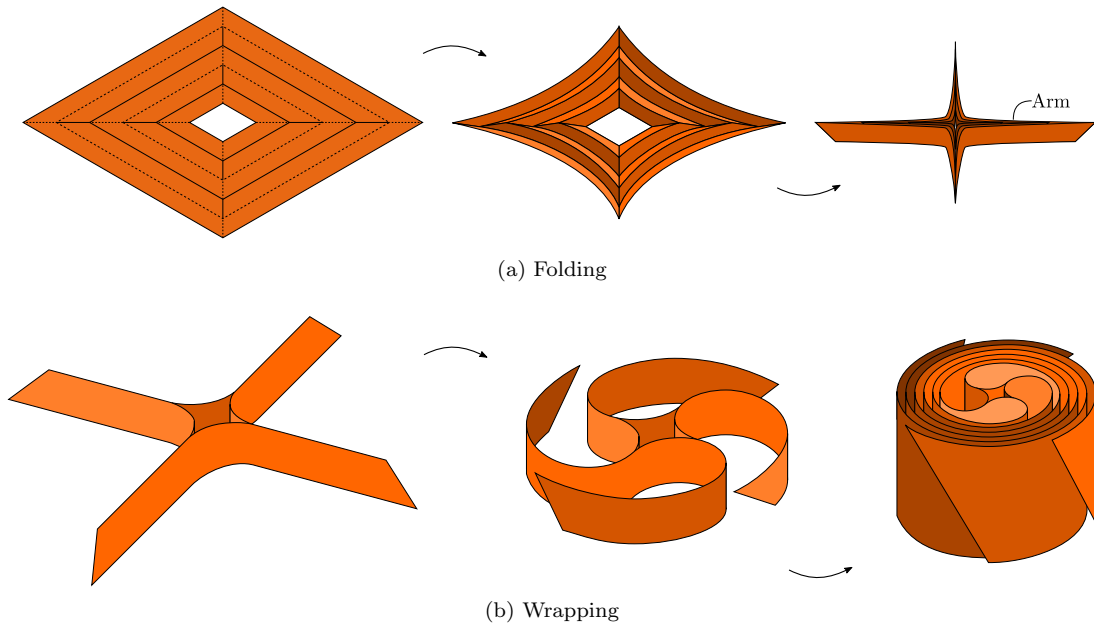


Figure 3.2: Star folding and wrapping, illustrated for  $N = 4$  and  $n = 5$ . For clarity, only the outermost strips are shown in (b).

structure.

Note how in Figure 3.3a the strips in a single sector have different lengths. This leads to an arm with variable thickness, and wrapping this variable-thickness arm produces a spiral-like shape where the pitch of the spiral decreases as one moves outwards. To leverage the technique in Section 2.1.2, where the wrapping of a stack with *uniform* thickness was modeled using an involute of a circle, assume that the strips have equal length  $L$ , as shown in Figure 3.3b. This leads to arms that have uniform thickness, and, in the wrapped state, can be described by an involute of a circle.

The assumption of equal strip length is unphysical and incompatible with the folding pattern. However, it simplifies the modeling of the wrapped form and, since it accounts for more material than is physical, it provides a conservative upper bound on the packaged diameter, and a conservative lower bound on packaging efficiency.

With this assumption, only a single 2D curve, called the *base curve*  $\mathbf{r}(s)$  need be described, as shown in Figure 3.4. All strips in a single sector are traced by curves that are parallel to this base curve, and the strips in the other sectors are related through  $N$ -fold rotational symmetry. The base curve is shown as the thick curve in Figure 3.4a. It consists of three parts: the dotted curve  $\mathbf{q}(s)$ ,

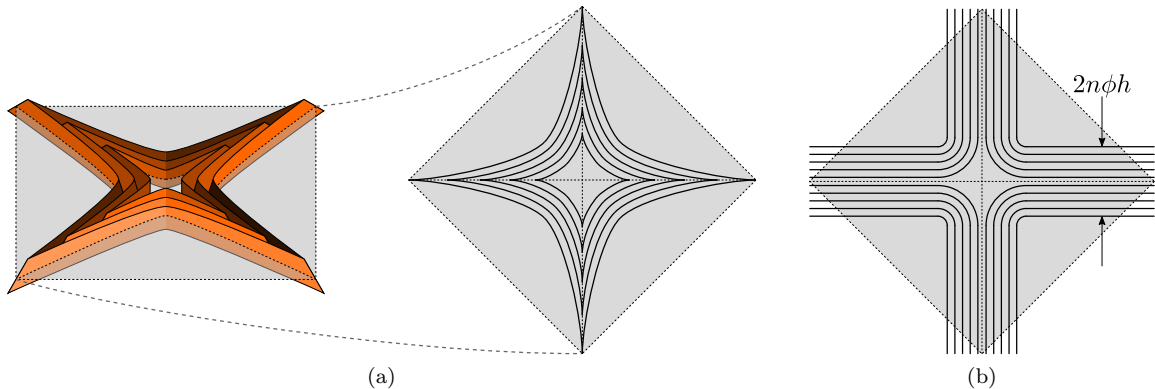


Figure 3.3: (a) The curves that trace the paths of the strips can be generated by taking a slice through the folded form. (b) Equal strip length  $L$  is assumed to produce arms of constant thickness  $2n\phi h$ .

the solid curve  $\mathbf{p}(s)$ , and a dashed curve that is copy of  $\mathbf{p}(s)$  rotated clockwise by the angle  $\beta$ .

$$\mathbf{r}(s) = \begin{cases} \mathbf{R}\mathbf{p}(-s) & \text{if } s \in [-L/2, -(L/2 + s_p)) \\ \mathbf{q}(s) & \text{if } s \in [-(L/2 + s_p), (L/2 + s_p)) \\ \mathbf{p}(s) & \text{if } s \in [(L/2 + s_p), L/2] \end{cases} \quad (3.2)$$

where  $\mathbf{R}$  is a rotation matrix that implements the clockwise rotation by  $\beta$ , and  $s_p$  is the arclength of the curve  $\mathbf{p}$ .

The  $i^{\text{th}}$  strip follows a curve  $\mathbf{r}(i; s)$  that is parallel to the base curve, separated by a distance  $(i - 1/2)\phi h$ :

$$\mathbf{r}(i; s) = \mathbf{r}(s) + \left(i - \frac{1}{2}\right) \phi h \mathbf{n}(s) \quad (3.3)$$

where  $\mathbf{n}(s)$  is the normal to the base curve,  $i$  is the integer index (between 1 and  $n$ ) of the strip, and  $\phi \geq 1$  is a thickness multiplier that accounts for any gaps between the strips.

Figure 3.5 shows the construction of  $\mathbf{q}(s)$  and  $\mathbf{p}(s)$ .  $\mathbf{q}(s)$  is a circular arc  $AB$  of radius  $R_0$  centered at a point  $O_0$ . It turns the base curve through an angle  $\pi - \beta$ .  $\mathbf{p}(s)$  is constructed in a piecewise manner; it consists of four pieces:

1.  $BC$ , a circular arc of radius  $R_0$ , centered at  $O_0$ , and a continuation of arc  $AB$
2.  $CD$ , a circular arc of radius  $R_1$ , centered at  $O_1$ , and tangent to  $BC$  at  $C$
3.  $DE$ , which is a vertical line segment, and
4.  $EF$ , which is an involute of a circle.

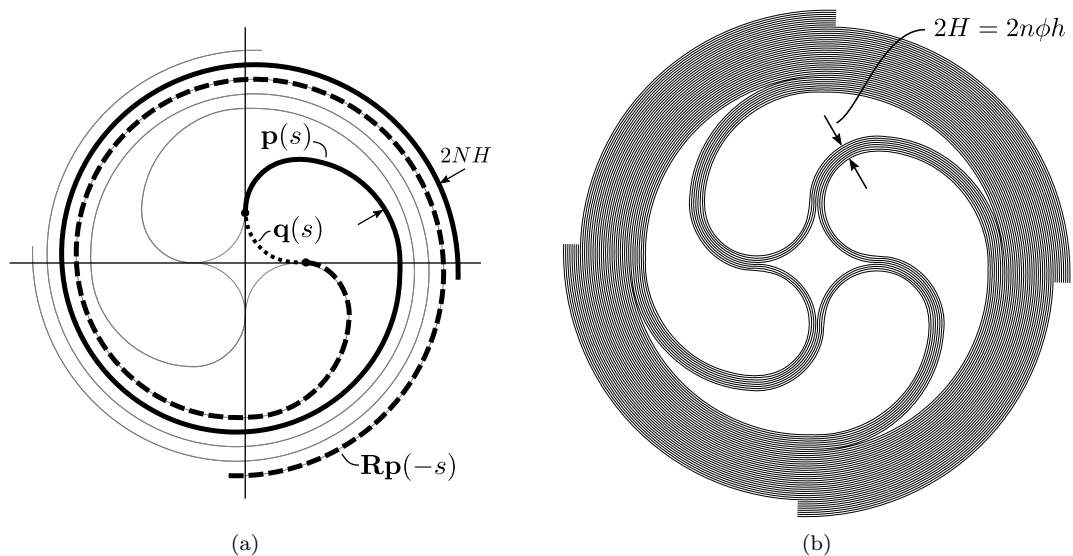


Figure 3.4: (a) Base curve  $\mathbf{r}$  used to model the wrapped strips, which consists of three generator curves:  $\mathbf{Rp}(-s)$ ,  $\mathbf{q}(s)$ , and  $\mathbf{p}(s)$ . (b) The strips are traced by curves parallel to the base curve.

The details of this geometry and the various conditions on these pieces that ensure continuity are discussed in Appendix C.

As shown in Figure 3.4, the spacing between the arms of the involute is  $2\pi c = 2NH$  where  $H = n\phi h$  is half the thickness of each arm. The factor of  $N$  accounts for the  $N$  arms being wrapped.

The radius  $R_0 = R_{min} + (n - 1/2)\phi h$  is such that the longitudinal curvature limit  $1/R_{min}$  for an initially flat strip does not exceed the Tresca yield criterion:

$$R_{min} \geq \frac{Eh}{2\sigma_y(1 - \nu^2)} \quad (3.4)$$

where  $E$  is the material modulus,  $\sigma_y$  is the yield stress, and  $\nu$  is the Poisson's ratio.

Note that this curve has discontinuous curvature at all points where two pieces meet. It is not expected that a wrapped membrane will follow this curve exactly; however, it is a simple curve that may be used to estimate key parameters. As was shown in Section 2.1.6, circular arcs can be a close approximation of the bent equilibrium shape of the stack for the case of wrapping a structure with parallel slipping folds.

The cross-sections of wrapped structures produced by this method have, by design,  $N$ -fold symmetry. Figure 3.6 shows examples of the wrapped configuration of structures with  $N = 3, 5, 9$ . Figure 3.6 also shows the increase in the number of voids with  $N$ ; there are  $N$  voids corresponding to the  $N$  arms, and 1 void in the very center.

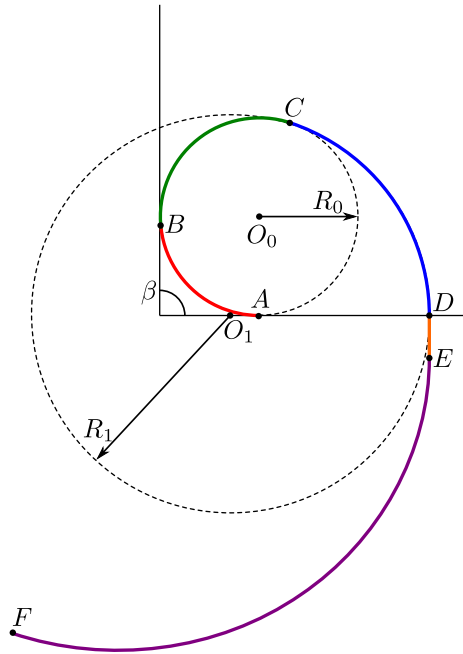


Figure 3.5: Components of the generator curves  $\mathbf{q}$  and  $\mathbf{p}$ .  $\mathbf{q}$  consists of the curve  $AB$ , and  $\mathbf{p}$  consists of the curve  $BCDEF$ .

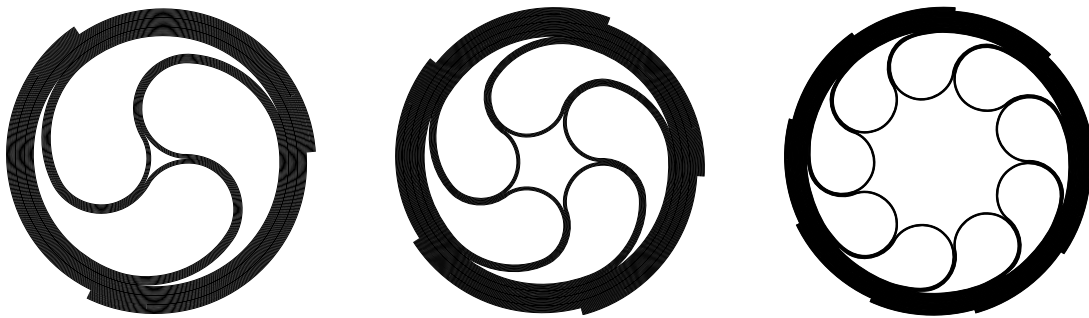


Figure 3.6: Wrapped configuration of structures with varying values of  $N$ . From left to right,  $N = 3, 5, 9$ .

### 3.1.2 Estimate of Maximum Slip

The slip  $l(i; s)$  between the  $(i+1)^{th}$  and the  $i^{th}$  strip in a sector is defined as before in Section 2.1.3 as the difference between the arc lengths  $s_{i+1}$  and  $s_i$  of the two curves at a point parameterized by arclength  $s$  along the base curve:

$$l(i; s) \equiv s_{i+1}(s) - s_i(s) \quad (3.5)$$

Using Equation (2.9), this slip can be expressed in terms of  $\kappa(s)$ , the signed curvature of the base curve:

$$l(s) = \phi h \int_{s_0}^s \kappa(\tilde{s}) d\tilde{s} \quad (3.6)$$

where  $s_0$  is a location where the slip is identically defined to be zero. As before in Section 2.1, the slip is independent of the strip index  $i$ .

The curvature  $\kappa(s)$  of the base curve can be expressed in terms of the curvature of its individual pieces. Following Equation (3.2):

$$\kappa(s) = \begin{cases} -\kappa_p(-s) & \text{if } s \in [-L/2, -(L/2 + s_p)) \\ \kappa_q(s) & \text{if } s \in [-(L/2 + s_p), (L/2 + s_p)) \\ \kappa_p(s) & \text{if } s \in [(L/2 + s_p), L/2] \end{cases} \quad (3.7)$$

where  $\kappa_p(s)$  is the curvature of  $\mathbf{p}(s)$  and  $\kappa_q(s)$  is the curvature of  $\mathbf{q}(s)$ . Note that the first piece of the base curve,  $\mathbf{Rp}(-s)$  from Equation (3.2), has the same absolute curvature at a point  $-s$  as  $\mathbf{p}(s)$ ; curvature is unaffected by the rigid body rotation implemented by the matrix  $\mathbf{R}$ . There is, however, a negation since  $\mathbf{Rp}(-s)$  is traversed in the opposite direction as  $\mathbf{p}(s)$ .

Based on Equation (3.7) and on Equation (3.6), the slip profile for a sector can be calculated:

$$l(s) = l(-L/2) + \begin{cases} -\phi h \int_{-L/2}^s \kappa_p(-\tilde{s}) d\tilde{s} & \text{if } s \in [-L/2, -(L/2 + s_p)) \\ -l_p + \phi h \int_{-(L/2 + s_p)}^s \kappa_q(\tilde{s}) d\tilde{s} & \text{if } s \in [-(L/2 + s_p), (L/2 + s_p)) \\ -l_p + l_q + \phi h \int_{L/2 + s_p}^s \kappa_p(\tilde{s}) d\tilde{s} & \text{if } s \in [(L/2 + s_p), L/2] \end{cases} \quad (3.8)$$

where  $l_p$  and  $l_q$  the total slips accumulated over  $\mathbf{p}(s)$  and  $\mathbf{q}(s)$ , respectively:

$$l_p = \phi h \int_{L/2 + s_p}^{L/2} \kappa_p(\tilde{s}) d\tilde{s} \quad (3.9)$$

$$l_q = \phi h \int_{-(L/2 + s_p)}^{(L/2 + s_p)} \kappa_q(\tilde{s}) d\tilde{s} \quad (3.10)$$

By evaluating Equation (3.8) at one end of the wrapped sector at  $s = L/2$ , a relation between the slip at the both ends of the wrapped sector (i.e., at  $s = -L/2$  and  $s = L/2$ ) can be determined:

$$l(L/2) = l(-L/2) - l_p + l_q + \phi h \int_{L/2+s_p}^{L/2} \kappa_p(\tilde{s}) d\tilde{s} \quad (3.11)$$

From Equation (3.9), the integral term in the expression above is simply the slip  $l_p$  accumulated over  $\mathbf{p}(s)$ . From this:

$$l(L/2) - l(-L/2) = l_q \neq 0 \quad (3.12)$$

This indicates that, unlike z-folding and wrapping, there cannot be zero slip at both ends of each wrapped sector. The slip created by the curve  $\mathbf{p}(s)$  is cancelled exactly by its rotated copy  $\mathbf{Rp}(-s)$  but the slip contribution of the section  $\mathbf{q}(s)$  persists. This slip is not created during the wrapping stage, but during the folding stage when the strips are turned through an angle of  $\pi - \beta$ . Using Equation (2.12), this excess slip  $l_q$  can be found:

$$l_q = \phi h(\pi - \beta) \quad (3.13)$$

A symmetric way to accommodate this slip is to allow one end of the sector to slip by  $-l_q/2$ , and the other by  $l_q/2$ . Note that this excess slip depends only on  $\beta$  and  $h$ , and not on the size of the structure given by strip length  $L$ . Thus a structure can be made bigger without requiring additional strip.

The maximum slip  $l_{max}$  at the center of the wrapped sector is the sum of  $l_q/2$  and the slip  $l_p$  generated by the curve  $\mathbf{p}(s)$ :

$$l_{max} = \frac{l_q}{2} + l_p \quad (3.14)$$

$l_p$  can be calculated using Equation (2.12):

$$l_p = \phi h \left( \beta + \frac{\pi}{2} + \alpha_{max} - \alpha_0 \right) \quad (3.15)$$

Substituting this and Equation (3.13) into Equation (3.14):

$$l_{max} = \phi h \left( \pi + \frac{\beta}{2} + \alpha_{max} - \alpha_0 \right) \quad (3.16)$$

Define the non-dimensional maximum slip  $\chi \equiv l_{max}/h$ . It can be calculated to be as follows:

$$\chi = \phi \left( \pi + \frac{\pi}{N} + \alpha_{max} \right) - \left( \frac{a}{h} \right) \frac{\pi}{nN} \quad (3.17)$$

$$\alpha_{max}^2 = \left( \frac{\pi}{\phi n N} \right) \left[ \lambda - 2 \left( \psi + \left( n - \frac{1}{2} \right) \phi \right) \left( \pi + \frac{\pi}{N} + \xi \csc \xi \right) \right] + \left( \frac{\pi}{\phi n N} \right)^2 \left( \frac{a}{h} \right)^2 - 2 \quad (3.18)$$

$$\left( \frac{a}{h} \right) = \left( \psi + \left( n - \frac{1}{2} \right) \phi \right) \left( \cot \left( \frac{\pi}{N} \right) - \cot \xi + 1 \csc \xi \right) \quad (3.19)$$

$$\cot \xi = \cot \left( \frac{\pi}{N} \right) - 4\phi n \left( 1 - \cos \left( \frac{2\pi}{N} \right) \right)^{-1} \left( \psi + \left( n - \frac{1}{2} \right) \phi \right)^{-1} \quad (3.20)$$

where  $\alpha_{max}$  is the maximum value of the angular parameter of the involute of the circle,  $a$  is x-coordinate of point  $D$  in Figure 3.5, and  $\xi$  is an angular parameter of the wrapping curve.  $a$  and  $\xi$  are defined and evaluated, based on maintaining slope continuity between the pieces of the base curve, in Appendix C.  $\lambda \equiv L/h$  is the length-to-thickness ratio, and  $\psi \equiv R_{min}/h$  is the dimensionless minimum radius of curvature.

Figure 3.7 plots this non-dimensional maximum slip  $\chi$  against the length-to-thickness ratio  $\lambda$ , for various values of  $N$  and  $\psi$ .

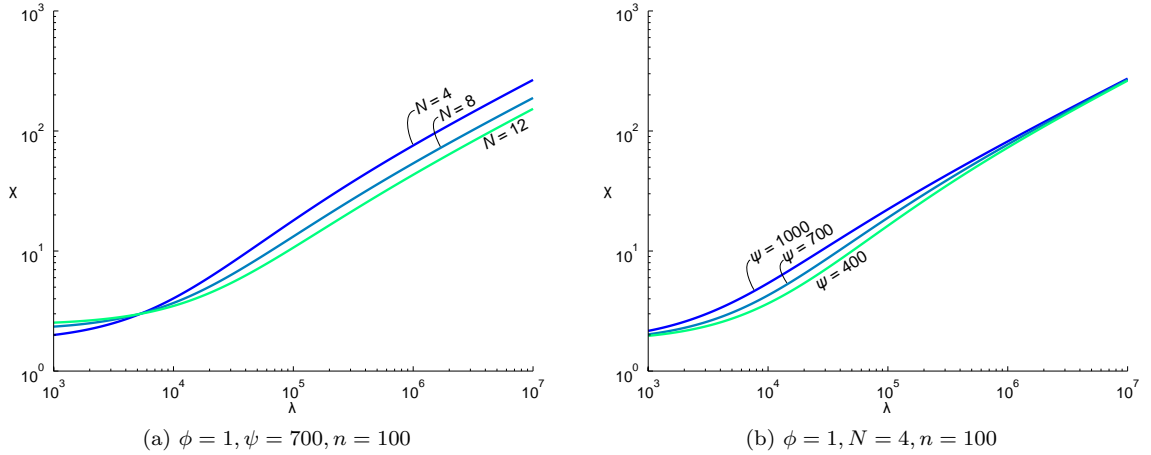


Figure 3.7: Non-dimensional maximum slip  $\chi$  as a function of the dimensionless deployed length  $\lambda = L/h$ , the polygonal degree  $N$ , and the dimensionless minimum bend radius  $\psi = R_{min}/h$ . For (a),  $\phi$ ,  $\psi$ , and  $n$  are held constant, and for (b),  $\phi$ ,  $N$ , and  $n$  are held constant.

It is interesting to consider how the maximum slip grows for large  $\lambda$ . As  $\lambda \rightarrow \infty$  the first term in Equation (3.18) and the third term in Equation (3.17) dominate and thus

$$\alpha_{max}^2 \rightarrow \frac{\lambda\pi}{\phi n N} \quad (3.21)$$

$$\chi \rightarrow \left( \frac{\phi\pi\lambda}{nN} \right)^{1/2} \quad (3.22)$$

Thus it is found that a growth in  $\lambda$  leads to a less-than-proportional increase in the maximum slip required.

Note that because of the assumption of equal arm length, the maximum slip estimates given in this subsection are lower bounds on the expected maximum slip. This is because in the physical case, the base curve will have higher curvature at any given point than is predicted by the present model. In the physical case, the spacing between successive turns of the base curve decreases as the arm thickness decreases, producing higher curvatures. This results in a greater amount of slip generated.

### 3.1.3 Packaging Efficiency

As in Section 2.1.4, the packaging efficiency  $\eta$  is defined as the ratio of the material volume  $V_m$  of the structure to the volume of the container  $V_p$  into which it is packaged. The material volume  $V_m$  is evaluated by multiplying the structure area  $A$  and its uniform thickness  $h$ :

$$V_m = Ah \quad (3.23)$$

The structure area is the area of an  $N$ -sided polygon with side-length  $L$ , less the area of the central polygonal hole with side length  $L_0$ :

$$A = \frac{N}{4} \cot \frac{\beta}{2} (L^2 - L_0^2) \quad (3.24)$$

Substituting Equation (3.1) for  $L_0$ , and using non-dimensional terms  $\lambda$  the length-to-thickness ratio, and  $\Omega \equiv w/L$  the non-dimensional strip width:

$$V_m = h^3 n N \lambda^2 \Omega \left( 1 - n \Omega \tan \frac{\beta}{2} \right) \quad (3.25)$$

The container that holds the packaged structure is taken to be a cylinder of height  $H_p$  and radius  $R_p$ . The cylinder height  $H_p$  is exactly the strip width  $w$ , and the radius of the cylinder  $R_p$  is the radius of the outermost point on any strip:

$$R_p = \max_{i,s} \|\mathbf{r}(i; s)\| \quad (3.26)$$

This gives the container volume  $V_p$ :

$$V_p = \pi R_p^2 w \quad (3.27)$$

Using these, the packaging efficiency  $\eta$  can be calculated to be

$$\eta = \frac{\pi\lambda}{nN\phi^2} \left(1 - n\Omega \tan \frac{\beta}{2}\right) \left[1 + \left(\alpha_{max} + \frac{\pi}{N}\right)^2\right]^{-1} \quad (3.28)$$

To simplify this expression somewhat, consider the special case where the central hole vanishes. Using Equation (3.1):

$$L_0 = 0 \Rightarrow w = \frac{L}{2n \tan(\beta/2)} \quad (3.29)$$

$$\Rightarrow \Omega n \cot \frac{\beta}{2} = \frac{1}{2} \quad (3.30)$$

$$\Rightarrow \eta = \frac{\pi\lambda}{2nN\phi^2} \left[1 + \left(\alpha_{max} + \frac{\pi}{N}\right)^2\right]^{-1} \quad (3.31)$$

Figure 3.8 plots this special case of packaging efficiency as a function of  $\lambda$ , for a variety of values of  $N$  and  $\phi$ .

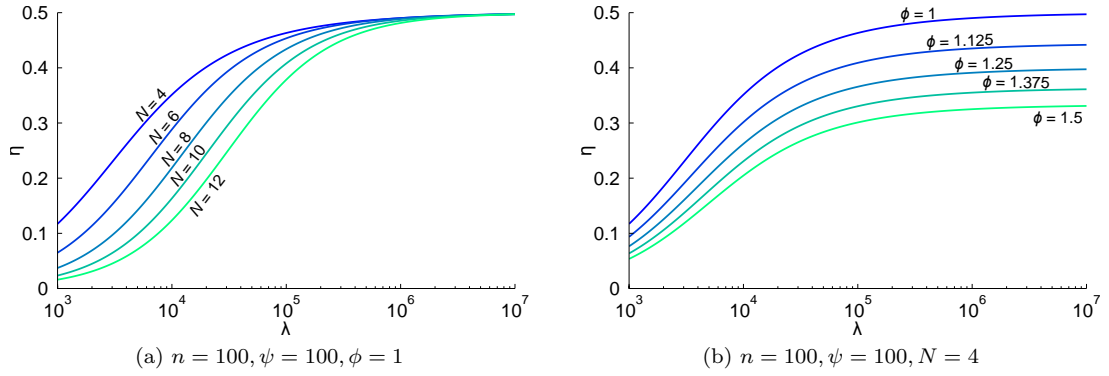


Figure 3.8: Packaging efficiency  $\eta$  as a function of the dimensionless deployed length  $\lambda = L/h$ , the polygonal degree  $N$ , and the strip thickness multiplier  $\phi$ . For (a),  $n$ ,  $\psi$ , and  $\phi$  are held constant, and for (b),  $n$ ,  $\psi$ , and  $N$  are held constant.

As can be seen Figure 3.8, for the same  $\lambda$ , the packaging efficiency is lower for higher values of  $N$ . That is, for the same side length and thickness, a triangular structure will package more efficiently than a square structure, which in turn will package more efficiently than a hexagonal structure. This is because as  $N$  increases, the number of voids in the center of the wrapped structure increases, and more volume is lost to these voids.

It is important to note that the packaging efficiencies plotted in Figure 3.8 are *lower bounds* for the expected experimental values. This is due to the assumption of equal strip length in Section 3.1.1, which results in the mathematical model of packaging accounting for more material than is physical. As such, the maximum packaging efficiency obtained from Equation (3.31) and plotted in Figure 3.8 is 50%.

Intuitively, as the length-to-thickness ratio  $\lambda$  increases and more material is wrapped in the outer

sections of the package, the volume lost to the central voids decreases in comparison to the material volume and the packaging efficiency should approach 1. This asymptote to  $\eta \rightarrow 1$  is what was seen in Section 2.1.4. However, it is not seen here because the present model is capable of generating only lower bounds on packaging efficiency.

This asymptotic behavior can be recovered by accounting for the increased volume of material considered in the mathematical model. By taking the material volume to equal that of the  $nN$  strips of equal length  $L$ , width  $w$ , and thickness  $h$ , the corrected material volume  $V'_m$  can be calculated:

$$V'_m = nNLwh \quad (3.32)$$

The packaged volume is still given by Equation (3.27). From this, the corrected packaging efficiency  $\eta'$  can be calculated:

$$\eta' = \frac{\pi\lambda}{nN\phi^2} \left[ 1 + \left( \alpha_{max} + \frac{\pi}{N} \right)^2 \right]^{-1} \quad (3.33)$$

This corrected expression for the packaging efficiency  $\eta'$  is a factor of 2 greater than the one obtained in Equation (3.31). Thus, it recovers the expected trend toward  $\eta' \rightarrow 1$  for large  $\lambda$ .

### 3.1.4 Packaging Experiments

Three test articles, summarized in Table 3.1, were made for performing packaging experiments. Models S1 and S2 were made from aluminized Mylar<sup>®</sup> films, and model S3 was made from uncoated Kapton<sup>®</sup> HN film. The slipping folds were implemented using ligaments, which were cut into the membrane substrate using a computer-controlled laser cutter (Universal Laser Systems<sup>®</sup> ILS9.75). The ligament dimensions are given in Table 3.2.

For model S3, the diagonal fold lines were implemented as slipping folds with ligaments. The diagonal fold lines in models S1 and S2 were implemented as standard non-slipping folds. These models were able to be packaged because the amount of slip needed at the ends of the wrapped sectors is very small, on the order of the thickness of the membrane, as indicated by Equation (3.13). These standard fold lines were defined by perforations (with hole diameters of roughly 150  $\mu\text{m}$  and hole spacing of roughly 550  $\mu\text{m}$ ) laser-cut into the membrane substrates.

<b>Model ID</b>	$N$	$h$ ( $\mu\text{m}$ )	$L$ (m)	$\log_{10} \lambda$	$n$	$\psi$
<b>S1</b>	4	50.8	0.99	4.29	11	29.3
<b>S2</b>	3	25.4	0.67	4.42	6	58.7
<b>S3</b>	4	50.8	0.47	3.97	5	29.3

Table 3.1: Experimental Test Articles

Model S1 was too large to be cut as a single piece on the laser cutter; it was cut in four separate

<b>Model ID</b>	Ligament Width (mm)	Ligament Length (mm)
<b>S1</b>	1.0	7.3
<b>S2</b>	1.0	3.6
<b>S3</b>	2.0	5.0

Table 3.2: Ligament characteristics for the experimental test articles

parts and then joined together using lengths of Kapton<sup>®</sup> tape.

Unlike in Section 2.1.7, where the maximum slip could be calculated and induced in the stack, the mathematical models presented in Section 3.1.1 only provide lower bounds of the maximum slip needed for star-folding and wrapping. As such, it was impossible to pre-slip these models to the exact amount required for packaging.

To package, plugs with circular cross-sections were used. These plugs were steel rods with a diameter of 2.98 mm. As the model was wrapped, initially loosely, around the plugs, the strips were allowed to slip as needed by ensuring that the plugs did not tightly clamp the membrane strips. As the folded arms were wrapped further, contact between the strips and the plugs was difficult to avoid. Toward the final stages of wrapping, it was difficult to allow the strips to slip freely.

After wrapping, the membrane models were held clamped by a loop of string. The diameter of the wrapped membrane was measured using digital calipers at the middle, away from the ligaments and near the restraining string.

Unlike in the case of z-folded wraps, where circular plugs would have resulted in the membrane stack following a figure-8 profile and specially shaped plugs were required, plugs with circular cross sections were deemed to be sufficient.

The experimental packaging efficiencies are plotted in Figure 3.10. These packaging efficiencies were calculated by assuming the height of the package to be the strip width. Also plotted are three curves with the same  $N$ ,  $n$ ,  $\psi$ , and  $\omega$  values, with the  $\phi$  values for which the theoretical curves pass through the experimental points. Since the predicted packaging efficiencies are conservative upper bounds for expected experimental efficiencies,  $\phi \leq 1$  must be chosen for the theoretical curves to pass through the experimental points. For the three star-folded and wrapped models,  $\phi = 0.778, 0.700, 0.657$  were obtained, indicating the degree to which the models underpredict the packaging efficiency.

Another measure of the degree of underprediction is simply the ratio of predicted packaging efficiency (for  $\phi = 1$ ) and the measured packaging efficiency. This is shown in Table 3.3.

<b>Model ID</b>	$\eta_{predicted}$	$\eta_{measured}$	$\frac{\eta_{predicted}}{\eta_{measured}}$
<b>S2</b>	53%	67%	0.79
<b>S3</b>	47%	64%	0.72
<b>S4</b>	54%	80%	0.68

Table 3.3: Measured and predicted packaging efficiencies

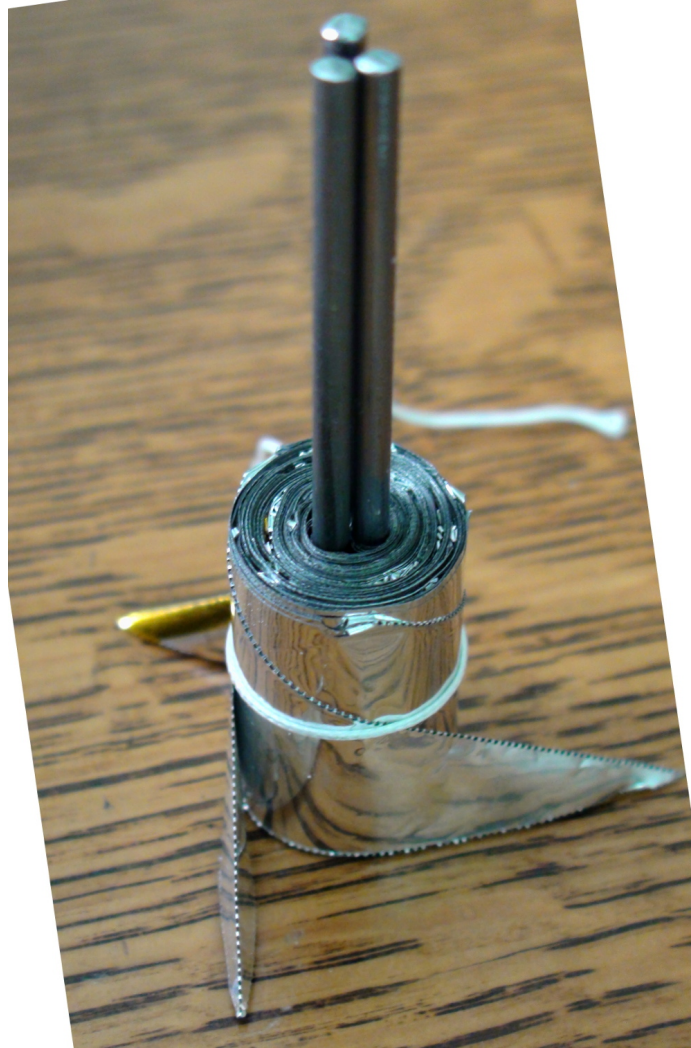


Figure 3.9: Model S2 packaged to a diameter of 18 mm and a height of 30 mm.

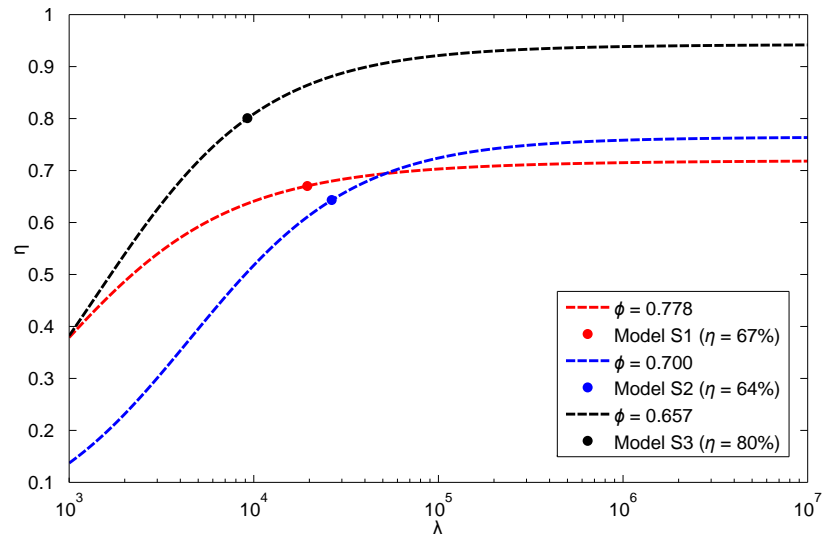


Figure 3.10: Packaging test results for star-folded and wrapped membrane test articles.

## 3.2 Structural Architectures

### 3.2.1 Pretensioning with Scalloped Edges

The technique described in Section 2.2 of using scalloped edges to pretension a structure with parallel slipping folds can be modified to work with the polygonal structures under discussion. As shown in Figure 3.11 for an example case of  $N = 6$ , each individual sector of the structure can be implemented with parabolic scallops. The structure as a whole can be tensioned by applying  $N$  radially outwards forces  $F_c$  at each of the  $N$  outer corners. The parabolic edges distribute this applied tension to uniform uniaxial distributed tension in the sector.

Due to the symmetry of this structure, the required tensioning forces are equal; this allows for the  $N$  booms (or  $N/2$  booms if  $N$  is even) to be identical, or, if the structure is pretensioned by centrifugal forces [37], for the  $N$  tensioning masses to be the same.

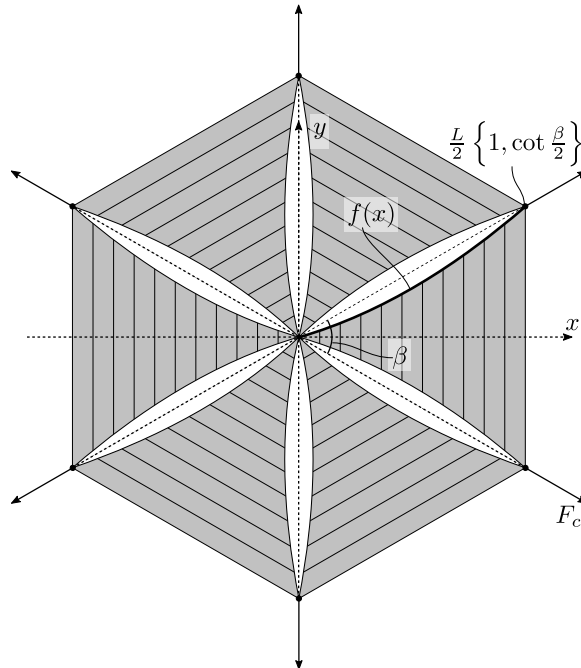


Figure 3.11: Each sector has scalloped edges to redistribute corner tensioning forces into uniaxial uniform tension in the arms.

Through symmetry, the profile of only one scalloped edge for a sector needs to be described. The profile of the other edge for that sector is obtained through reflection about the  $x$  axis, and the profiles of the other sectors are obtained through  $N$ -fold symmetry. For this one sector, the edge

profile  $f(x) : [0, \frac{L}{2} \cot \frac{\beta}{2}] \rightarrow [0, \frac{L}{2}]$  is

$$f(x) = \left(\frac{2\sigma}{L}\right)x^2 + \left(\tan \frac{\beta}{2} - \sigma \cot \frac{\beta}{2}\right)x \quad (3.34)$$

$$\sigma \equiv \frac{PL}{4F_x} \geq 0 \quad (3.35)$$

where  $\sigma$  is the dimensionless loading parameter,  $P$  is the force per unit length induced in the structure,  $\beta = \frac{2\pi}{N}$  is the sector angle, and  $F_x$  is the constant horizontal component of the tension in the parabolic edge.

Since  $f(x)$  must remain above the  $x$ -axis, it is required that

$$f'(x=0) \geq 0 \quad (3.36)$$

$$\Rightarrow \sigma \leq \tan^2 \frac{\beta}{2} \quad (3.37)$$

This gives the upper limit for the loading parameter  $\sigma$  given a polygonal degree  $N$ . The maximal value of  $\sigma$  for any  $N$  occurs at  $N = 3$ , for which  $\sigma \leq 3$ .

The ratio between the area of the scalloped structure and the polygon area  $\rho \equiv A/A_{polygon}$  is

$$\rho = 1 - \frac{\sigma}{3} \cot^2 \frac{\beta}{2} \quad (3.38)$$

This area ratio depends only on the loading parameter  $\sigma$  and the sector angle  $\beta$ . As the loading parameter  $\sigma$  increases, the area ratio  $\rho$  decreases. This is because as  $\sigma$  increases, the curvature of the scalloped edges increases, leading to a larger degree of scalloping and more lost area. The upper bound for  $\sigma$ , given by Equation (3.37), determines the lower bound for  $\rho$ :

$$\rho \geq \frac{2}{3} \quad (3.39)$$

From this, it can be seen that at most, a third of the polygonal area may be lost to scalloping. For the structure area to completely fill the parent polygon (i.e.,  $\rho = 1$ ) requires  $\sigma = 0 \Rightarrow P = 0$  which means that the structure is not pretensioned. Therefore,  $\rho < 1$  and some area must always be lost.

The magnitude of the radially outwards force applied at each outer corner is

$$F_c = 2F_x \left( \sec \frac{\beta}{2} + \sigma \cos \frac{\beta}{2} \right) \quad (3.40)$$

Figure 3.12 shows examples of structures with  $N = 3, 4, 5$  with scallop-edge sectors for  $\sigma = \frac{1}{2} \tan^2 \frac{\beta}{2}$ .

As discussed in Section 2.2, the use of scalloped edges to tension membranes is not novel; the

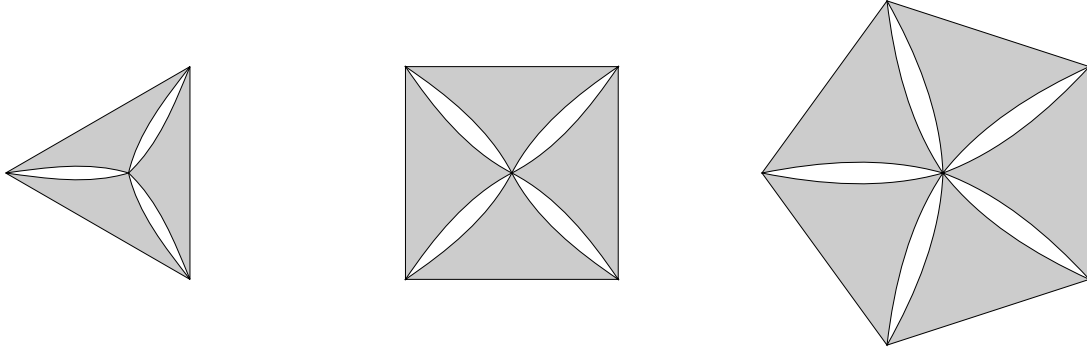


Figure 3.12: Examples of structures with scalloped sectors for (from left to right)  $N = 3, 4, 5$ .

novelty here lies in the highly anisotropic in-plane stiffnesses of the structure being prestressed, and the resulting need for an anisotropic pretension field.

### 3.2.2 Strips with Bending Stiffness

The architecture discussed in Section 3.2.1 was developed for membrane structures, i.e., structures with negligible out-of-plane bending stiffness. To react out-of-plane loading, these structures need to be pretensioned. This subsection proposes a structural architecture that is intended for strips with non-negligible bending stiffness.

The packaging schemes proposed in Section 3.1 require strips to be flattened and rolled; strips can be designed so that when they are unrolled, they have much higher bending stiffness than when they are flattened. The simplest example of such a strip is a carpenter's tape measure, which is a thin-shell structure that can be flattened and then rolled [38]. Other strip cross-sections are also possible, with more corrugations, or with other structural elements that pop out of plane to increase the deployed plane bending stiffness.

As shown in Figure 3.13, these bending-stiff strips can be arranged in a geometry favorable to the packaging schemes described in Section 3.1. In this geometry, they can be configured to react a normal pressure loading  $B$ .

The strips are pinned at either end to diagonal cords. The diagonal cords, in turn, are attached to a central hub at one end, and to the tips of deployable booms at the other. The booms are clamped to the hub at the center. After deployment, the diagonal cords are tensioned to a value  $T$ .

This particular arrangement of structural components was designed to be applied to space solar power satellites; further discussion on this application is included in Chapter 4.

A simple static model of this architecture is developed below for a structure with no central hole (i.e.,  $L_0 = 0$ ) and for small deflections. The strips are modeled as Euler-Bernoulli beams with uniform bending stiffness  $(EI)_{strip}$ . The ligament connections between the strips are not accounted for in this simplified model. The diagonal cords are modeled as lines under tension  $T$ , and the booms

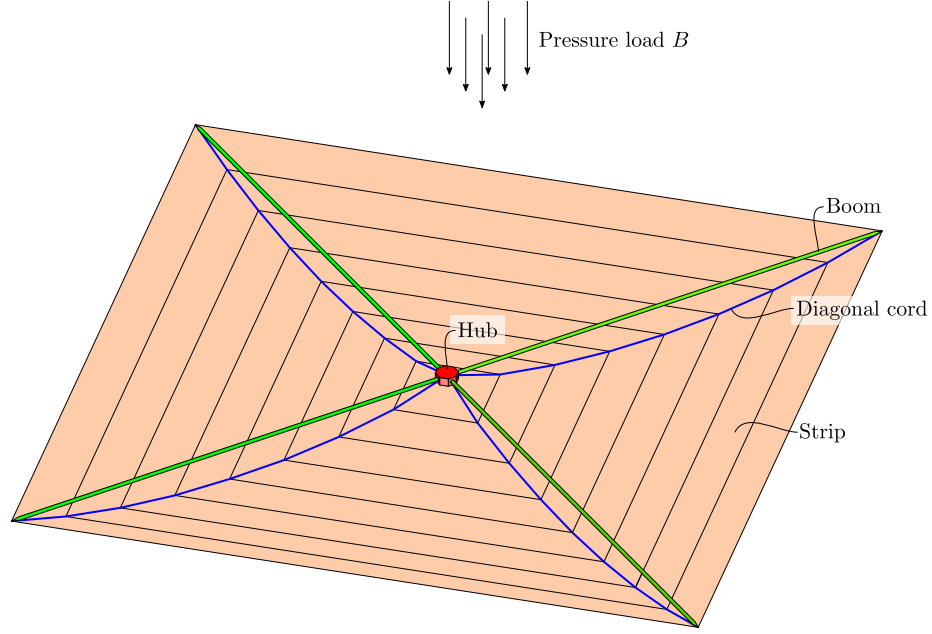


Figure 3.13: Structural architecture where the strips have bending stiffness to react out-of-plane pressure loading  $B$ .

are modeled as beam-columns with bending stiffness  $(EI)_{boom}$ .

The strips are simply supported and loaded normally by a distributed loading given by the pressure loading  $B$  multiplied by the strip width  $w$ . The vertical deflection of the  $i^{th}$  strip is

$$u_{strip,i}(x) = -\frac{BwL_i^4}{8(EI)_{strip}} \left[ \frac{1}{3} \left( \frac{x}{L_i} \right)^4 - \frac{1}{2} \left( \frac{x}{L_i} \right)^2 + \frac{5}{48} \right] + u_{DC,i} \quad (3.41)$$

where  $(EI)_{strip}$  is the strip bending stiffness,  $x \in [-L_i/2, L_i/2]$  is a coordinate along the strip,  $L_i = L/n(i - 1/2) + L_0$  is the length of the  $i^{th}$  strip, and  $u_{DC,i}$  is the vertical deflection of the point at which the strip is attached to the diagonal cord.

The distance between these attachment points is  $v \equiv w \sec \frac{\beta}{2}$ . As shown in Figure 3.14, these attachment points are assumed to deflect only vertically; an attachment point cannot deflect in the circumferential direction if  $N$ -fold rotational symmetry is assumed, and the deflection in the radial direction is assumed to be negligible.

The vertical deflection of the  $i^{th}$  attachment point on the diagonal cord  $u_{DC,i}$  can be computed by assuming small angles, and thus uniform tension  $T$  throughout the diagonal cord. From vertical equilibrium at the  $i^{th}$  attachment point:

$$T \left( \frac{u_{DC,i} - u_{DC,i+1}}{v} \right) + T \left( \frac{u_{DC,i} - u_{DC,i-1}}{v} \right) = BwL_i \quad (3.42)$$

$$\Rightarrow u_{DC,i+1} - 2u_{DC,i} + u_{DC,i-1} = -\frac{BvwL_i}{T} \quad (3.43)$$

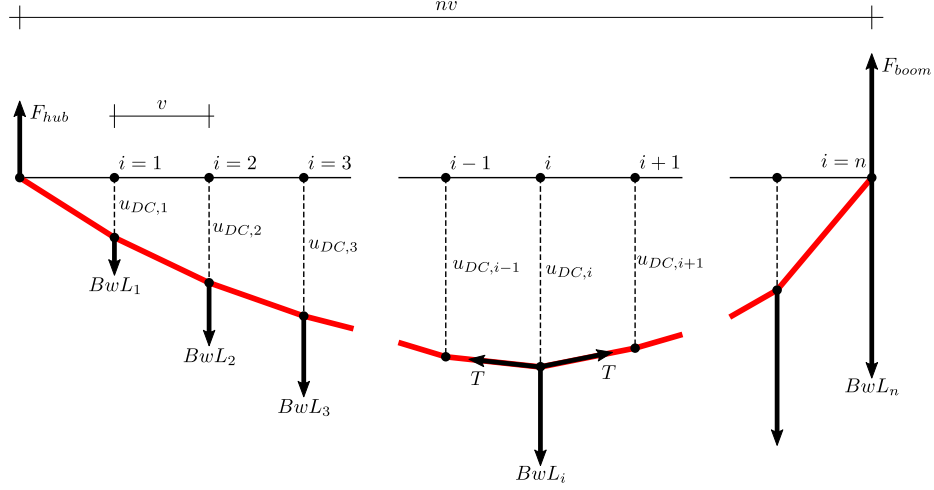


Figure 3.14: Diagonal cord equilibrium.

The innermost attachment point (i.e.,  $i = 0$ ) is fixed to the hub, thus  $u_{DC,0} = 0$ . The outermost attachment point is pinned to the tip of the boom, thus  $u_{DC,n} = u_{boom}$ . The diagonal cord deflections are computed by a shooting method to satisfy these boundary conditions.

Through global force and moment equilibrium for the diagonal cord, the end forces at the hub  $F_{hub}$  and the boom tip  $F_{boom}$  can be found to be

$$F_{boom} = BwL \frac{(n+1)(2n+1)}{6n} \quad (3.44)$$

$$F_{hub} = BwL \frac{(n+1)(2n-2)}{4n} \quad (3.45)$$

The booms are modeled as beam-columns, with the following relation between the end moments  $M_1, M_2$ , tip shear load  $2F_{boom}$ , end rotations  $\theta_1, \theta_2$ , and tip deflection  $u_{boom}$ :

$$\begin{bmatrix} M_1 \\ M_2 \\ -2F_{boom} \end{bmatrix} = \mathbf{K} \begin{bmatrix} \theta_1 \\ \theta_2 \\ u_{boom} \end{bmatrix} \quad (3.46)$$

The stiffness matrix  $\mathbf{K}$  is a function of the boom bending stiffness  $(EI)_{boom}$ , the boom length  $L_{boom} = \frac{L}{2} \cot \frac{\beta}{2}$ , and the axial compressive load  $T$ . It can be found in standard texts [39].

The booms are clamped at the hub and pinned to the diagonal cords; thus the boundary conditions are  $\theta_1 = 0$  and  $M_2 = 0$ . Using these, Equation (3.46) can be reduced and inverted to find the tip deflection  $u_{boom}$ :

$$\begin{bmatrix} \theta_2 \\ u_{boom} \end{bmatrix} = \tilde{\mathbf{K}}^{-1} \begin{bmatrix} 0 \\ -2F_{boom} \end{bmatrix} \quad (3.47)$$

The stiffness and length of this boom determine its Euler buckling load [40]; this gives the upper bound for the tension  $T$  in the diagonal cord:

$$T < \frac{\pi^2(EI)_{boom}}{4L_{boom}^2} \quad (3.48)$$

Figure 3.15 shows examples of deflected shapes obtained from this model for  $N = 3, 4, 6$ . The construction of this simple model decouples the deflections along the diagonals and the deflections along the strips. The diagonal cord deflections are dictated by diagonal cord tension  $T$  and the boom stiffness alone, and the strip deflections are controlled by the strip bending stiffness alone.

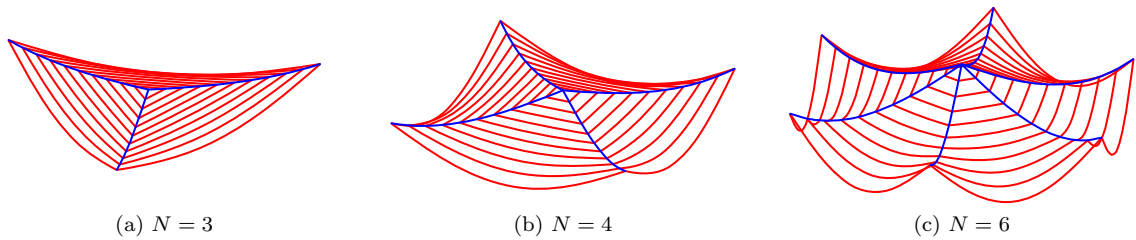


Figure 3.15: Examples of deflected shapes produced by the simple static model of a polygonal structure with strips that have finite bending stiffness. For clarity, the booms are not shown, and the strips are represented by their midlines. The strips are shown as red lines, and the diagonal cords are blue.

### 3.3 Deployment Concept

A two-stage deployment process, consisting of an unwrapping stage followed by an unfolding stage, is described in this section. The unwrapping stage is shown in Figure 3.16. A cage is used to hold the packaged structure constrained. This cage has  $N$  slots through which the  $N$  ends of the arms can protrude. Pulling at the  $N$  endpoints of these arms, labeled as  $A_1, A_2, A_3, A_4$  for the  $N = 4$  example in Figure 3.16, unwraps the structure. To reduce the effects of friction between the unwrapping structure and the cage, a set of rollers may be used, as is shown in Figure 3.16.

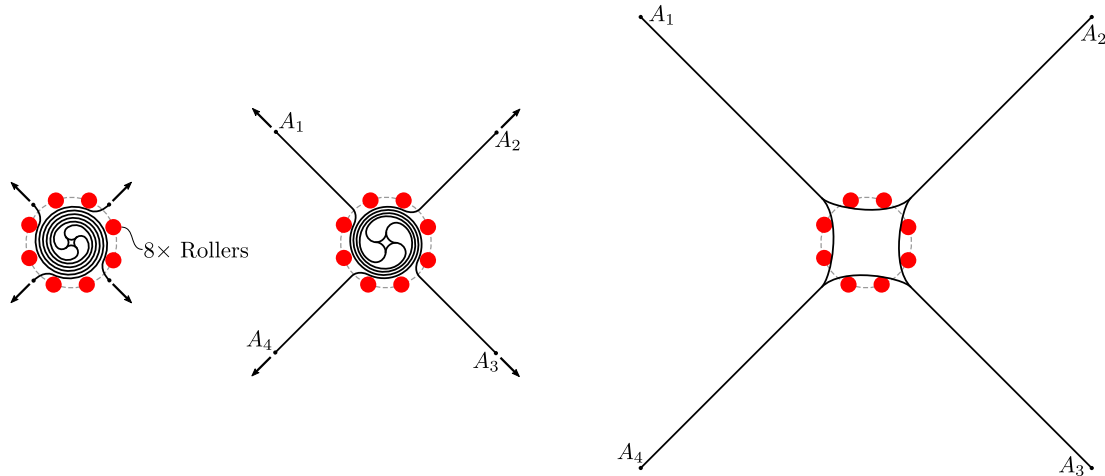


Figure 3.16: The first stage of deployment, unwrapping, shown for a model with  $N = 4$ . The  $N$  ends of the arms are pulled radially outwards to unwrap. A number of rollers can be used to reduce frictional sliding between the structure and the cage. For clarity, only one strip per sector is shown.

The second stage of deployment is unfolding, as shown in Figure 3.18. For this stage, the cage needs to be removed from the plane of deployment. This may be done, for example, by hinging the rollers out of the plane of deployment.

The unfolding must be sequential, from the inside out. This is a kinematic constraint on a 2D in-plane deployment; inner polygons must be unfolded before outer polygons can be unfolded. This can be seen by considering the intersection of the mid-surfaces of the strips in a single sector and a horizontal plane during the unfolding process.

Consider the resulting curves for two strips indexed  $i$  and  $i + 1$ , as depicted in Figure 3.17. Since the length of the  $i^{th}$  strip is smaller than the length of the  $(i + 1)^{th}$  strip, the arclength of the  $i^{th}$  curve is less than the arclength of the  $(i + 1)^{th}$  curve. The deployment is done by pulling a point radially outwards along the diagonal. Figure 3.17 shows the structure in two states: one with this point at position  $A$ , and the other with this point at position  $A'$ .

If the separation between the two points  $A$  and  $B$  (and correspondingly  $A'$  and  $B'$ ) remains constant, the  $i^{th}$  curve must straighten before the  $(i + 1)^{th}$  curve. A strip must be straight before it can unfold, and for it to be straight, all horizontal slices through the strip, such as the curve

depicted in Figure 3.17, must be straight. Since the  $i^{\text{th}}$  curve straightens before the  $(i+1)^{\text{th}}$  curve, the  $i^{\text{th}}$  strip can unfold before the  $(i+1)^{\text{th}}$  strip.

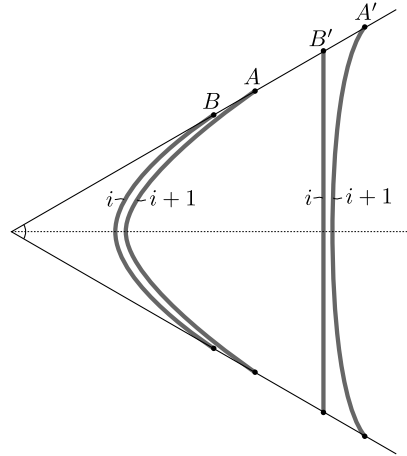


Figure 3.17: A cross-section of an unfolding sector produced by taking the intersection of the mid-surfaces of strips  $i$  and  $i+1$  and a horizontal plane. The strips are shown in two states during unfolding, showing that strip  $i$  must straighten before strip  $i+1$ .

To prevent the strips from unfolding rapidly, a constraining mechanism is required to hold them folded, and release them at appropriate times as the ends of the arms  $A_1$  through  $A_4$  are pulled further outwards. This mechanism is an analog of the clip used in the unfolding of the z-folded-and-wrapped structure as described in Section 2.3. However, there need to be  $N$  clips, one per sector, and each clip needs to move with the outermost strips. Figure 3.18 represents the clips as 4 red rectangles, one per sector, that move outwards as the structure unfolds.

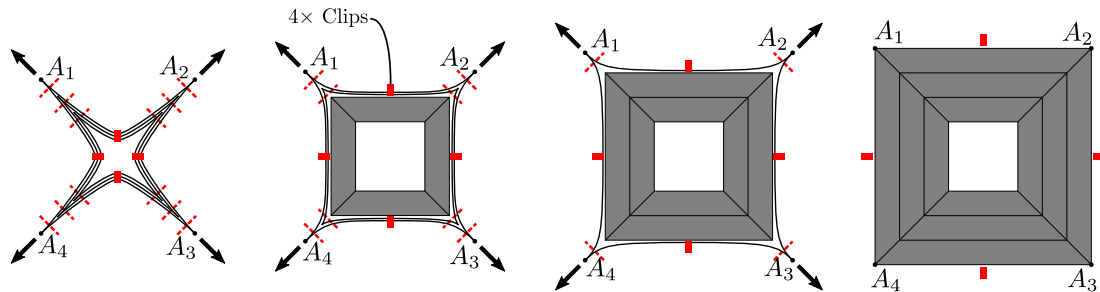


Figure 3.18: The second stage, unfolding, of deploying a star-folded slip wrap shown for  $N = 4$ ,  $n = 3$ . Folds must be undone sequentially, from the inside out. 4 clips, drawn as red rectangles, are required to ensure this sequential unfolding. Alternatively, a number of constraints along the folded arms can be used, drawn as dashed lines, that disengage in sequence to control unfolding.

An alternative method to achieve orderly unfolding is to constrain the unwrapped structure at multiple points along the diagonal arms. During deployment, these constraints can be removed in sequence, from the innermost to the outermost, as the ends of the diagonal arms are pulled outwards. In the example case depicted in Figure 3.18, these constraints are shown as 12 dashed lines, 3 per

diagonal arm. Each ring of constraints holds a number of strips in a bent configuration, preventing them from unfolding. Once a ring of constraints is removed, the strips can straighten and unfold.

These constraints can be realized in a variety of ways, e.g., a breakable adhesive layer between strips, straps that loop around the diagonal arms to hold them closed, or a clip-like mechanism that pinches the strips to keep them folded. Once disengaged, a constraint is no longer required, and can be discarded.

### 3.4 Physical Model with Bending-Stiff Strips

To experimentally demonstrate some of the packaging techniques, structural architectures, and deployment concepts described in this chapter, a lab-scale structure was constructed using carbon fiber reinforce plastic (CFRP) composite material. This model, dubbed C1, was square (i.e.,  $N = 4$ ), with side length  $L = 0.60$  m, 4 strips per quadrant (i.e.,  $n = 4$ ), and strip width  $w = 60$  mm.

This model was built to validate, and to conceptualize at a small scale, the structural design and deployment concept for a much larger space solar power satellite. The design of these satellites is discussed in further detail in Chapter 4. The structural architecture of this satellite is as described in Section 3.2.2, with the strips having bending stiffness to resist out-of-plane loading. These strips are supported at their edges by TRAC booms [41], which is a type of collapsible and rollable structure that, when unfurled, has much higher bending stiffness than when flattened. A TRAC boom cross-section is shown in Figure 3.19a; the two curved flanges can be flattened elastically to be parallel to the  $x$ -axis, allowing the boom to be rolled. The strips for the small-scale model were designed to have cross sections that mimic these edge TRAC structures, as illustrated in Figure 3.19b.

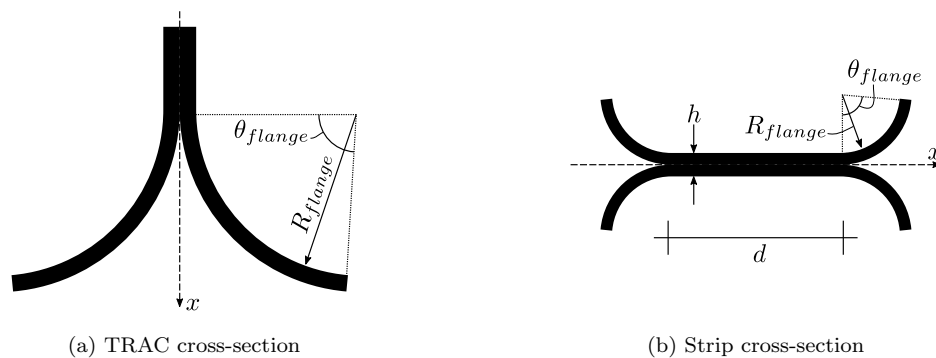


Figure 3.19: Cross sections of (a) a TRAC boom and (b) a strip for model C1.

The physical small-scale model had strips of center thickness  $h \approx 75 \mu\text{m}$ , flat section width  $d = 38.1$  mm, flange radius  $R_{flange} = 10$  mm, and flange angle  $\theta_{flange} = 57^\circ$ .

The strips were constructed by adhering together, along the flat section, a top carbon fiber half and a bottom carbon fiber half. Each half had an open “C” cross-section, comprising two

circular-arc flanges and a flat section. Each half consisted of two unidirectional carbon fiber plies, arranged in a  $[0^\circ/90^\circ]$  orientation such that when adhered together, the strip had a central layup of  $[90^\circ/0^\circ/0^\circ/90^\circ]$ , where  $0^\circ$  corresponds to the longitudinal strip direction. This layup was chosen to reduce the longitudinal bending stiffness of the strip, and thus reduce the minimum radius of curvature of the flattened strip.

The strips were connected to each using ligaments to implement slipping folds. The ligaments consisted of thin polymer threads sandwiched between the top and bottom halves of the strips.

Deployment experiments were conducted according to the concept described in Section 3.3. Mechanisms and restraints were designed and fabricated to enable the realization of these concepts, and then tested on the 2-axis deployment rig described in Section 2.3.2.

### 3.4.1 Fabrication Process

Preimpregnated tapes of unidirectional plies (Toray T800 fibers in a ThinPreg<sup>TM</sup> 120EPHTg-402 epoxy resin matrix, with a fiber volume fraction of  $\approx 50\%$ ) arranged in a  $[0^\circ/90^\circ]$  stack were obtained from North Thin Ply Technologies [42]. These plies, produced using a spread-tow technique [43], were lightweight (with per-ply areal of density of  $\approx 17\text{ g m}^{-2}$  compared to traditional composites which may be a factor 4 to 10 heavier) and thin (with ply thickness of  $\approx 20\text{ }\mu\text{m}$ ). This material is lightweight but has in-plane fiber-parallel stiffnesses ( $E_1 = 128\text{ GPa}$  [44]) much greater than polymer films of these thicknesses.

The fabrication process is illustrated in Figure 3.20. To produce the top and bottom halves of the strips, these tapes were laid up on 1.5-m-long aluminum molds. The mold cross-section was 12.7 mm thick, 50.4 mm wide, and had semi-circular ends with 6.35 mm radius; this cross-section dictated the strip cross-section. (However, due to the unbalanced layup in the flange sections, the as-manufactured flange radius was measured to be  $\approx 10\text{ mm}$ , larger than the mold radius.) The halves were vacuum bagged and cured in an autoclave at  $120^\circ\text{C}$  for 2 hours.

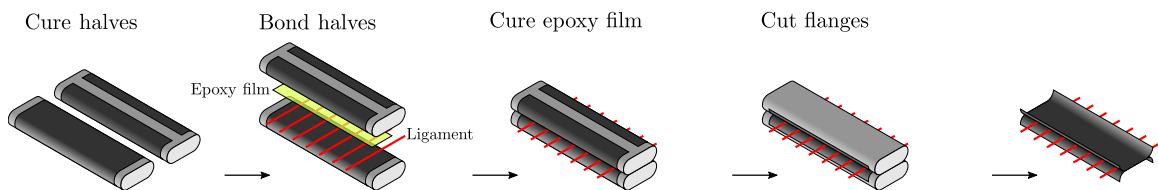


Figure 3.20: Strip fabrication process for the small-scale model.

After curing the top and bottom strip halves were not removed from the molds. Lengths of braided Spectra<sup>®</sup> line ( $\approx 100\text{ }\mu\text{m}$  diameter) were placed on the bottom half at the desired regular spacing. A layer of Patz PMT-F4 epoxy film was applied to the flat section of the top half, and the two strip halves were clamped together, sandwiching the ligaments. The length of the ligaments was greater than flattened width of the strip; this allowed strips to be knotted together later. This

assembly was vacuum-bagged and the epoxy film was cured at 120 °C for 2 hours. Once cured, the extra tape width was cut off to produce flanges of the correct size. Individual trapezoidal strips were cut from these 1.4 m-long parent structures.

The strips were connected together, as needed, by knotting ligaments together, thus forming the individual sectors or quadrants. The quadrants were assembled together by integrating the diagonal cords. The diagonal cords were Zebco Omniflex monofilament fishing line (279  $\mu\text{m}$  diameter), that were connected to the strips using a sliding hinge connection as shown in Figure 3.21. The fishing line was passed through 10 mm-long polyimide tubes with a 320  $\mu\text{m}$  inner diameter, which were attached to the strips using polyimide tape. This design allows the diagonal cords to be tensioned without tensioning the strips, as desired by the structural architecture described in Section 3.2.2.

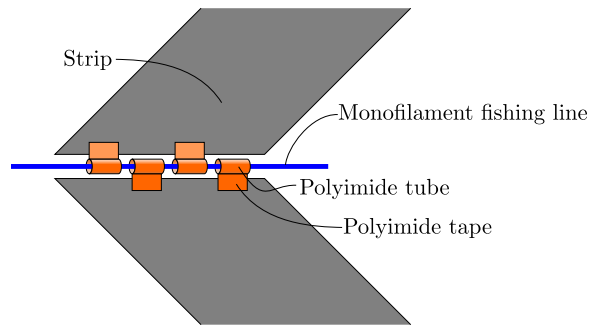


Figure 3.21: Diagonal cord construction.

Figure 3.22 shows a completed 0.6 m  $\times$  0.6 m model in its unfolded state.

### 3.4.2 Packaging Experiment

Model C1 was packaged manually according to the scheme described in Section 3.1. The three sets of folds arranged in squares were folded one at a time, from the outside inwards. For each set of folds arranged in a square, all four quadrants were folded simultaneously. As such, four human folders were required to achieve this simultaneity. The folds were held closed by using standard clip-style metal hair pins.

Once folded, the model C1 was wrapped. Four wooden dowels of 12.7 mm diameter were used as wrapping guides, to ensure that a minimum radius of curvature was not violated. As mentioned in Section 3.1.4, determining the exact amount of pre-slip required for star-folded structures is not possible with the currently available analytical tools; as such, slip was allowed to develop during wrapping by relaxing, at several points in time along the wrapping process, the pinching of the four wooden dowels on the structure. The wrapping was done manually, with four humans wrapping the four folded arms. The wrapped structure was restrained by a loop of string.

Figure 3.23 shows model C1 packaged to a diameter of 52 mm. The mathematical model of wrapping presented in Section 3.1 predicts a packaged diameter (for  $h = 80 \mu\text{m}$ ,  $R_{min} = 6.35 \text{ mm}$ ,

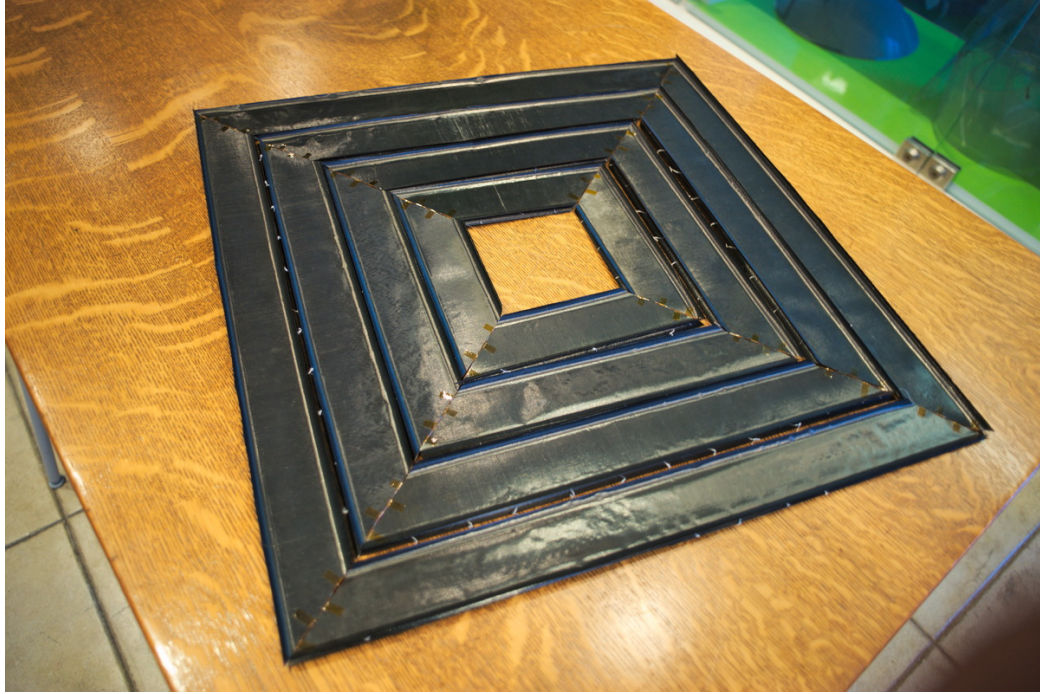


Figure 3.22: Model C1 unfolded to a size of 0.6 m  $\times$  0.6 m.

and  $\phi = 1$ ) of 49.6 mm. It is believed that this discrepancy between the predicted and the measured diameter is a result of the manual method of packaging a structure with non-negligible bending stiffness. A more systematic and controlled method of packaging (e.g., using a dedicated wrapping jig) is likely to reduce this error.



Figure 3.23: Model C1 packaged to a diameter of 52 mm.

### 3.4.3 Deployment Experiments

Deployment experiments were conducted to demonstrate feasibility of a smooth and controlled deployment of a structure with strips that have non-negligible (and, indeed, variable) bending stiffness. This behavior is different from the deployment experiments conducted in Section 2.3.2, where the strips were made from uniform-thickness membrane material and had very small, constant, and uniform bending stiffness.

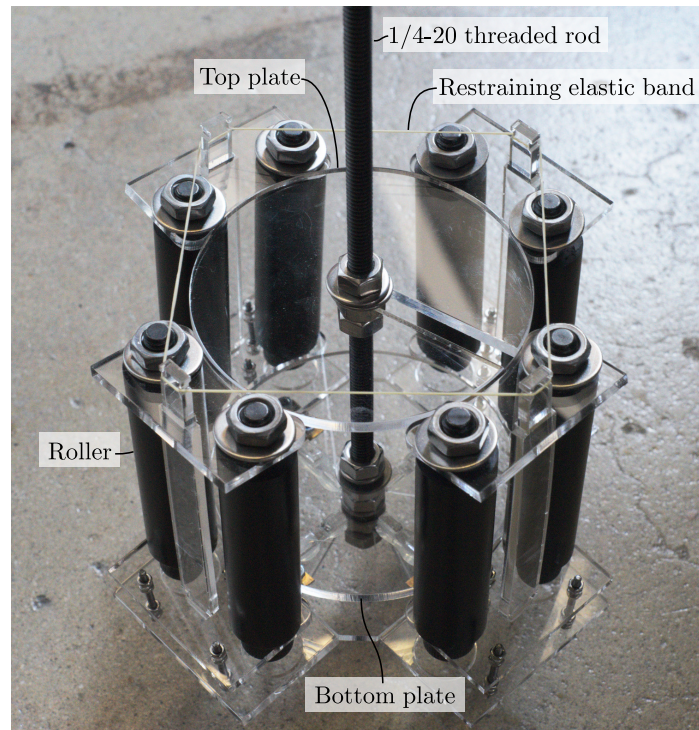


Figure 3.24: Cage for the deployment of star-folded slip wraps.

A cage was built to hold the models in a packaged configuration and to control the unwrapping process. The cage, shown in Figure 3.24, was constructed using laser-cut 3.18 mm-thick acrylic plates, which were held together by a central 1/4 – 20 threaded rod. 8 rollers, 2 per quadrant, were implemented using shoulder screws and Nylon tubes of 15.9 mm outer diameter and 63.5 mm length. These rollers constrained the packaged models circumferentially, and reduced friction between the cage and the model during the unwrapping stage of deployment. The rollers were placed such that the model had a packaged diameter of 85 mm.

A top plate and a bottom plate provided axial support to the models, preventing large motions in the axial direction. The separation between these plates was 75 mm.

The rollers were hinged to the bottom plate assembly, so that they could swing out of the plane of deployment for the second stage of unfolding. The rollers were held in a vertical orientation for the first stage of unwrapping by a restraining elastic band; cutting this elastic band allowed the

hinges to swing out of the plane of deployment.

To control the second stage of unfolding, 12 paper straps, 3 per arm, were used to hold the arms folded, as described in Section 3.3. As folded arms were pulled radially outwards, tension was transferred into these straps. These straps were notched, and broke at a certain level of tension. Because of the geometry of this unfolding process, these straps broke in sequence, from the inside out. As such, the strips were released in sequence, resulting in a sequential and ordered unfolding.

The 2-axis deployment rig described in Section 2.3.2 was used to conduct these deployment tests. The deployment was displacement controlled; the ends of the diagonal arms were attached to the carriages which were moved apart at a rate of about  $11.9 \text{ mm s}^{-1}$ .

The model was deployed in a horizontal plane about 0.25 m above the surface of the table on which the 2-axis deployment rig rested. To do this, the cage was suspended by a string from an overhead support. A 400 g weight was suspended from the bottom of the cage to stabilize its orientation.

Figure 3.25 plots the measured components of the average deployment forces  $(\mathbf{F}_1 + \mathbf{F}_3)/2$  and  $(\mathbf{F}_2 + \mathbf{F}_4)/2$  for a single deployment. Here,  $\mathbf{F}_1$  and  $\mathbf{F}_3$  are the forces measured along one diagonal, and  $\mathbf{F}_2$  and  $\mathbf{F}_4$  are the forces measured along the other diagonal.

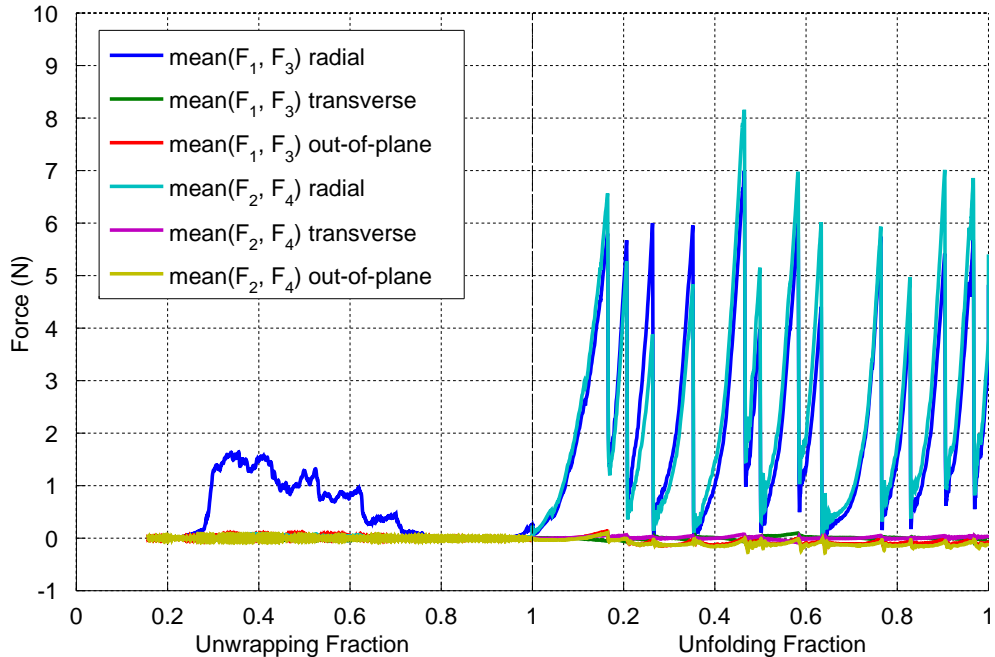


Figure 3.25: Deployment force profiles for model C1. During the first stage of unwrapping, the unfolding fraction is fixed at 0, and during the second stage of unfolding, the unwrapping fraction is fixed at 1.

As can be seen from Figure 3.25, the radial components of the forces are dominant. During unwrapping, tension is being applied only along of the two diagonals; this is because the unwrapping along the diagonals is coupled, and pulling along one diagonal also unwraps the other. Therefore, any motion lag between the carriages on either diagonal will result in one diagonal being taut,

and the other slack. (This is an effect of the deployment being displacement-controlled, and not force-controlled.)

During unfolding, the deployment force profile has a sawtooth character. This corresponds to the structure being tensioned, the tension being transmitted to the paper straps along the diagonals, and the straps breaking, one at a time. In this particular set of experiments, 12 straps were used, 3 per diagonal, and 12 peaks can be counted in Figure 3.25.

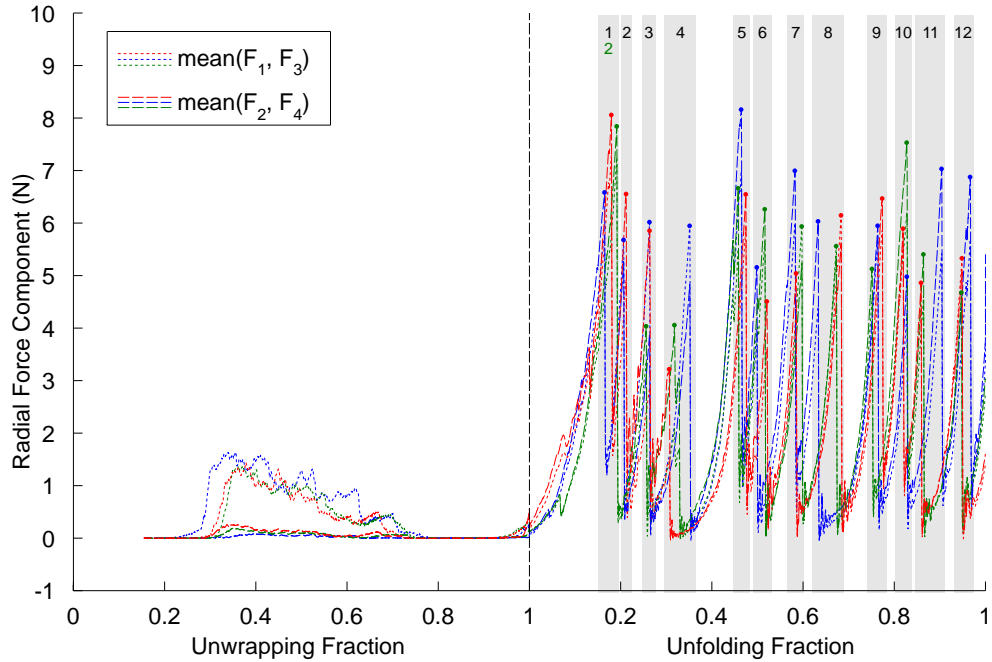


Figure 3.26: Deployment force profiles for model C1. Lines of the same color are from the same deployment. Dotted and dashed lines distinguish the forces measured along the two diagonals.

Figure 3.26 shows the deployment force profiles for a set of three deployments of model C1. For clarity, only the radial components of the average deployment forces  $(\mathbf{F}_1 + \mathbf{F}_3)/2$  and  $(\mathbf{F}_2 + \mathbf{F}_4)/2$  are plotted. The lag between the motion of the deployment carriages is again evident; the majority of the work of unwrapping is being performed along the 1-3 diagonal alone.

In the unfolding stage of deployment, the force peaks are marked by dots. The shaded rectangles group the force peaks from the three separate deployments, and show good separation between the breaking of the straps. A grouping of the force peaks into three sets of four can be seen; each set of four corresponds to the four straps in a single ring. This indicates, as desired, a sequential unfolding from the inside out. For one of the deployments (indicated by the set of green lines in Figure 3.26), the first force peak corresponds to the breaking of two straps simultaneously; this accounts for the lack of a force peak in the second group for that particular deployment.

Figure 3.27 shows views from an overhead camera, showing the start of deployment and the end of the unwrapping stage for model C1. In both these photographs, the 8 rollers are oriented

vertically, and have not yet been hinged out of the plane of deployment.

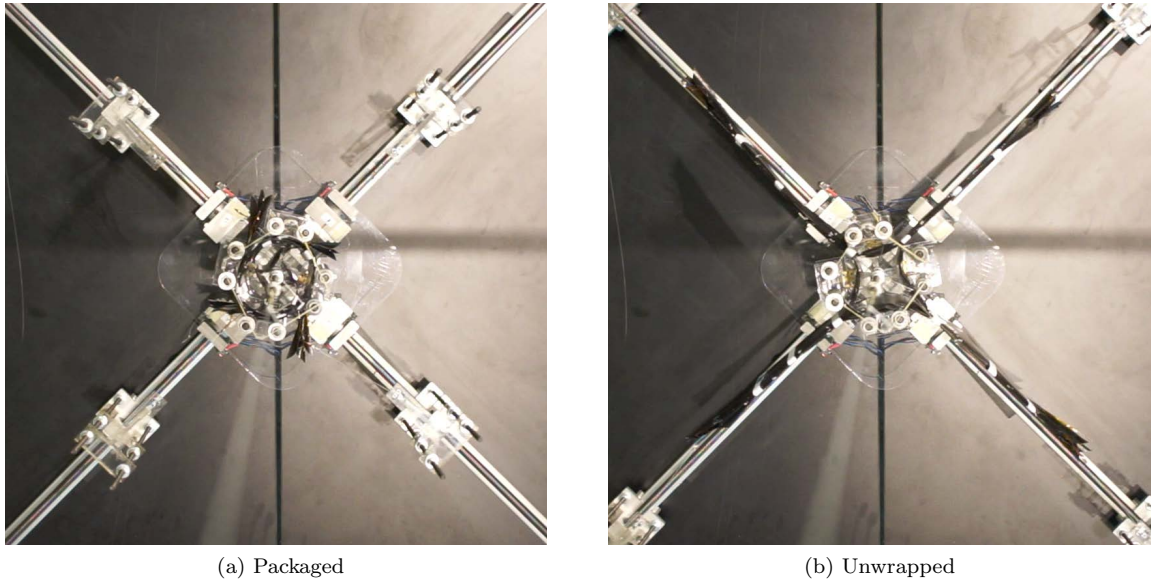


Figure 3.27: The unwrapping stage of the deployment of model C1.

Figure 3.28 shows overhead photographs of the second stage of the deployment of model C1. (a) shows the 8 rollers having been hinged out of plane; this was done by cutting, using scissors, the elastic band that held the rollers in their vertical positions. (b) shows the first ring of paper straps broken, and the innermost polygon of strips unfolded. (c) shows the second ring of paper straps broken, with two polygons of strips unfolded. Finally, (d) shows the final ring of paper straps having been disengaged, and the model fully deployed.

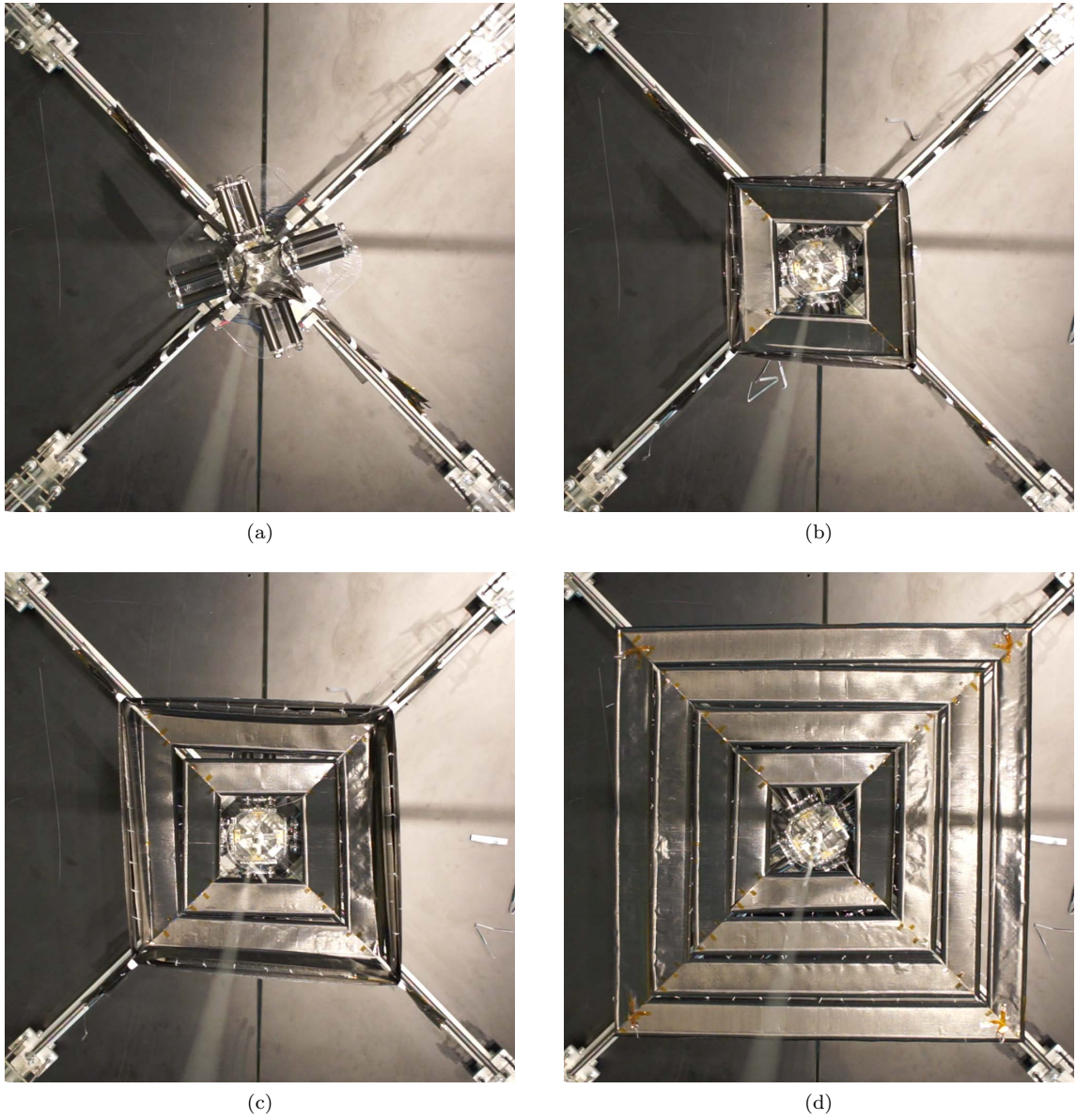


Figure 3.28: The unfolding stage of the deployment of model C1.

### 3.5 Summary

This chapter presented a family of packaging schemes that used the essential ideas from Chapter 2 – slipping folds and slip wrapping – and applied them to another set of fold patterns. These fold patterns consist of concentric  $N$ -sided polygons; folding produces  $N$  arms of strips, which can be wrapped to produce a tightly packaged cylindrical configuration. Packaging was demonstrated using physical lab-scale membrane models. The wrapping can be designed such that the maximum bending strains are bound by predictable values and the structure is not permanently deformed.

Two structural architectures were described. One was an extension of the scalloped-edge pretensioning scheme discussed in Section 2.2, and the other used bending-stiff strips. The advantage of using the bending-stiff architecture is that deployed area is not lost to scalloping, as it is in the pretensioned alternative.

A deployment process was proposed, in which the structure is first unwrapped and then unfolded. A physical model of the bending-stiff structural architecture were fabricated. This was used to successfully demonstrate the packaging and deployment schemes for such structures.

## Chapter 4

# Structures for Space Solar Power Satellites

This chapter describes the preliminary structural design of a space solar power satellite. Space solar power is a proposed [45, 46] method of generating power for terrestrial applications: solar power is collected in space, converted to radio frequency (RF) energy, beamed to a ground station at Earth, where it is rectified and delivered to the power grid. This chapter describes in brief a concept for space solar power station, and then moves on to the structural design considerations of a single satellite that is part of this station.

The structural architecture described in Section 3.2.2 will be used here to prescribe the preliminary design of this satellite. The final sections of this chapter will use this architecture to arrive at preliminary mass and packaged size estimates for this space solar power satellite.

Portions of this chapter were previously published as [32].

### 4.1 The Need for Space Solar Power

Climate change is a pressing issue; global temperatures have risen by  $0.85\text{ }^{\circ}\text{C} \pm 0.20\text{ }^{\circ}\text{C}$  over the period 1880-2012 [47]. This has been attributed primarily to radiative forcing from greenhouse gases, especially carbon dioxide, the concentration of which has increased from  $278 \pm 5\text{ppm}$  in 1750 to  $390.5 \pm 0.1\text{ppm}$  in 2011 [47]. The energy supply sector is the largest contributor to global greenhouse gas emissions, and its contributions are growing at an accelerated pace [48]. There is therefore a desperate need for methods of electrical power generation that do not produce, as by-products, greenhouse gases [48].

Renewable energy sources such as terrestrial solar power systems and wind power systems produce power intermittently, and sources such as hydroelectric power and geothermal power require geographical access to useful sites, which limits their applicability. The intermittency of terrestrial solar power and wind power systems means that they must be paired with energy storage sys-

tems or other power sources to provide reliable supply. Additionally, these power sources are not dispatchable; i.e., supply cannot be adjusted quickly to match changes in demand [49].

Space solar power can be made available continuously, without being affected by the day/night cycle, cloud coverage, seasonal variations, and atmospheric conditions. It is dispatchable: power can be directed to one of many ground stations, where demand is highest.

Aside from the myriad technical challenges, there are two primary high-level challenges associated with space solar power: cost and complexity. The cost is dominated by the expense of launching the system into a geosynchronous orbit; this cost depends strongly on the total amount of mass being launched. Complexity arises from the traditionally proposed approaches to the construction of space solar power stations, involving assembly of systems by humans or robots in orbit. The concept described herein addresses the issues of cost and complexity by keeping mass low and by eliminating the need for in-space construction.

## 4.2 Space Solar Power Concept

The proposed space solar power station, as illustrated in Figure 4.1, comprises a large number of independent identical spacecraft flying in formation in geosynchronous orbit. Each spacecraft is composed primarily of a large number of independent multifunctional elements. These elements, called *tiles*, are capable of photovoltaic power generation, synthesis of a microwave-frequency signal, and wireless power transmission. This particular space solar power concept was developed as a product of a collaboration between the Atwater, Hajimiri, and Pellegrino research groups at the California Institute of Technology.

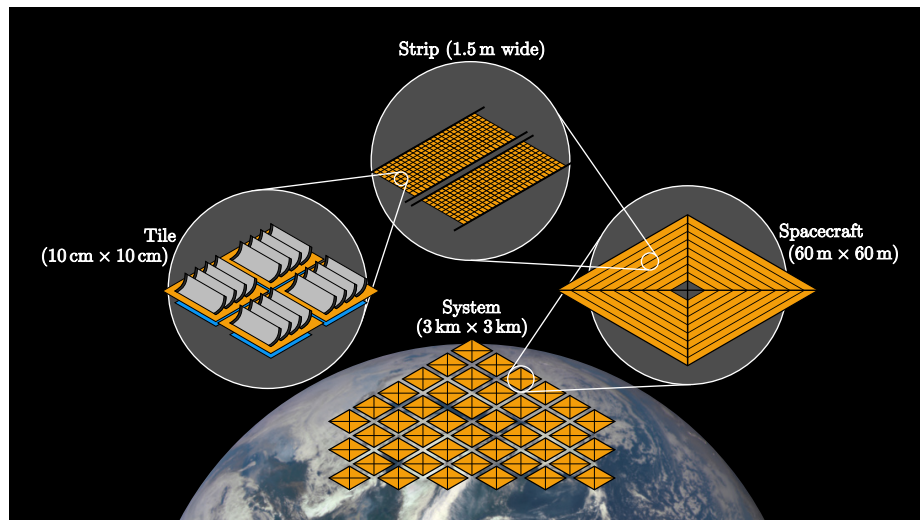


Figure 4.1: Overview of Space Solar Power System.

The tiles are interconnected and held in a planar configuration by a light, stiff structural frame-

work, creating a spacecraft that measures  $60\text{ m} \times 60\text{ m}$  and carries approximately 300,000 tiles. The geometry of this spacecraft is sheet-like: it has large in-plane dimensions (to collect solar power and to provide sufficient aperture for microwave power transmission), but comparatively small out-of-plane dimensions. For launch, the bulk of the spacecraft can be packaged into a  $\approx 1\text{ m}$  diameter,  $1.5\text{ m}$  tall cylinder.

Compaction is enabled by the ability of each tile to be flattened, and to spring back into the original configuration when it is deployed. This flattening reduces the wrapping thickness  $h$ , as defined in Chapter 3, thus increasing the length-to-thickness ratio  $\lambda$  and the packaging efficiency  $\eta$ . One particular design of a multifunctional tile capable of such flattening is briefly described.

This chapter deals exclusively with the preliminary structural design of a single spacecraft. The design of this space solar power system is a collaborative effort, and there are many aspects of the design, construction, and operation of such a space solar power system that are outside the scope of this chapter (e.g., the design of lightweight photovoltaic cells, large-scale phased arrays across independent spacecraft, integrated circuits for microwave signal synthesis, and formation flying).

Similarly, there are many performance metrics that must be considered in the design of such a system (e.g., overall system power efficiency, total mass, capacity factor, specific power). However, the concern herein is purely structural design, and, as such, only relevant metrics will be considered. The key structural drivers are areal density, packaged volume, deployed stiffness, and deployment precision. Low areal density ( $100\text{ g m}^{-2}$ ) and low packaged volume are needed to reduce launch costs. Additionally, the spacecraft must be deployed to a precise shape, and maintain this shape within acceptable levels under applied loading. This chapter will present a preliminary structural design of a spacecraft that has low areal density, small packaged volume, and is sufficiently stiff.

## 4.3 Background

This section provides a brief survey of two relevant bodies of work: the architecture and design of structures for space solar power systems and the design of concentrating photovoltaic power systems for spacecraft.

### 4.3.1 Structures for Space Solar Power Systems

Early structural concepts for space solar power systems (see Figure 4.2a) tended to be massive and complex [46, 50]. These concepts comprise structural systems (e.g., truss systems) that are designed to be assembled (by astronauts, robots, or a combination thereof) in orbit. The photovoltaic and power transmission systems are physically separate; the power transmission system is mounted on a gimbal that allows it to point to the ground station on Earth.

Later space solar power concepts have driven toward modular and lightweight structures.

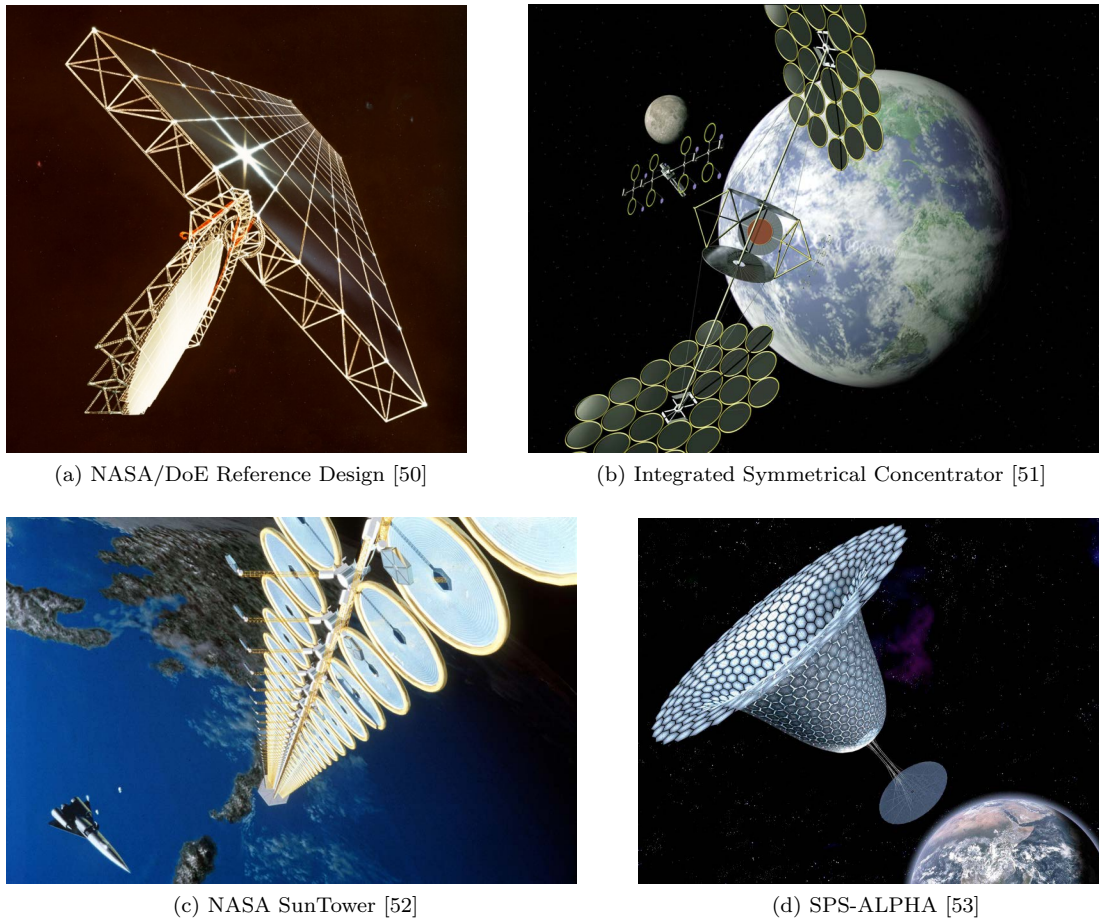


Figure 4.2: Space solar power system concepts.

The Integrated Symmetrical Concentrator concept [51] (see Figure 4.2b) consists of two reflector assemblies that direct sunlight to a central photovoltaic array, which is situated adjacent to the wireless power transmitter. The reflector assemblies can rotate about the axis of the system to direct sunlight onto the photovoltaic array. A later JAXA concept [54] envisions the reflectors and the power-generation-and-transmission segment as separate spacecraft, flying in formation. This reduces structural complexity by removing the gimbal system.

The NASA SunTower concept [52] (see Figure 4.2c) employs a gravity-gradient-stabilized structure that consists of a long central spine with many power-generating units arranged along its length. Each power-generating unit consists of a thin-film Fresnel concentrator (deployed and stabilized by an inflatable ring on the edge) and a photovoltaic unit. At the end of the spine is a wireless power transmission unit. The ESA SailTower concept [55] is similar in architecture; however, the concentrating photovoltaics are replaced by thin-film photovoltaic blankets.

The SPS-ALPHA concept [53] (see Figure 4.2d) is modular and robotically assembled in space. It comprises a large reflector system, a power-generation-and-transmission segment, and a connecting

truss structure. The reflector system directs sunlight onto the power-generation-and-transmission segment, which converts it to electricity, and beams it to Earth. The reflector system is composed of many individual membrane reflective surfaces (akin to solar sails) that can be individually pointed.

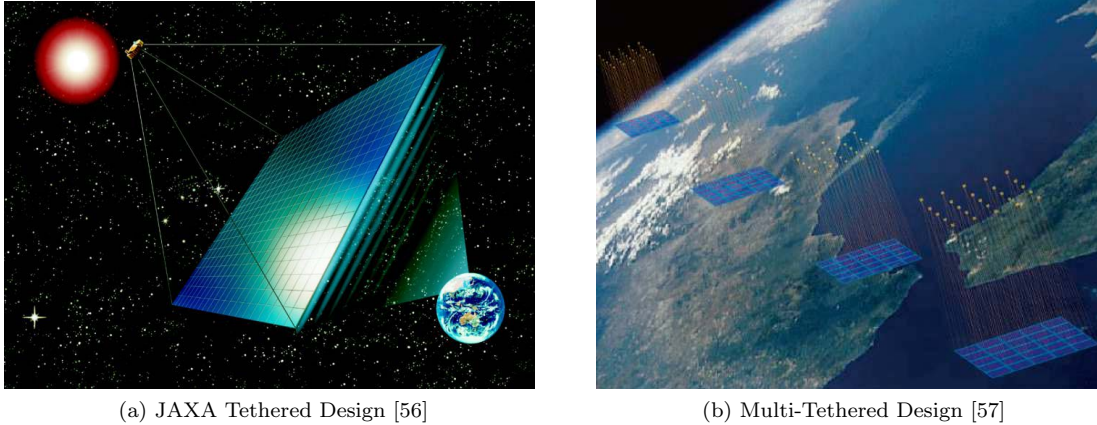


Figure 4.3: JAXA Tethered Concepts.

The tethered JAXA concept [56], shown in Figure 4.3, consists of a single square plate-like structure that has photovoltaic elements on one side, and a phased array of antennas on the other. The structure is stabilized by gravity gradient forces; four tethers from the corners of the square plate are connected to a satellite bus that acts as a counterweight. The phased array can electronically steer the microwave beam, precluding the need for a gimbal system.

A modular architecture, consisting of many tethered plates, has also been proposed [57]. It is envisioned to launch many individual modules, deploy them separately, and then assemble them together into a single monolithic structure by physically docking modules together.

### 4.3.2 Concentrating Photovoltaic Systems for Spacecraft

Using concentrating photovoltaic systems in space applications is attractive because of the potential for mass and cost savings. Without concentration, the power collection area is filled completely with photovoltaic cells, which are massive and expensive. Concentration reduces the cell area by the concentration factor, and it can be achieved by optical elements that have less areal density than photovoltaic cells. Here, a brief survey of concentrating photovoltaic systems for space applications is provided.

The SCARLET solar array on the Deep Space 1 mission [58] uses an array of linear concentrators to illuminate photovoltaic cells. The concentrators are arched Fresnel lenses, 1 cm wide and 4 cm long. They operate at a concentration factor of 8. The lenses are molded silicone with glass substrates, and are supported by graphite/epoxy frames. These frames stow against the plane of the photovoltaic cells, and are deployed to the functional focal length by lenticular tape springs [59].

The Stretched Lens Solar Array [60] has a similar optical configuration, but uses lighter flexible Fresnel lenses made from silicone rubber, without the glass substrate. These lenses can be flattened against the photovoltaic cells, and pop back up using spring-loaded arches at the ends of the lenses. Additionally, the Stretched Lens Solar Array uses thin composite material to support the photovoltaic cells, as compared to the honeycomb panel used in the SCARLET array [61]. Recent developments [62] allow panels comprising many such refractive concentrators to be flattened and then rolled (or folded) for additional compaction.

The FAST solar concentrator array [63] uses reflective linear concentrators to focus light onto photovoltaic cells on the backside of the adjacent linear concentrator. These concentrators operate at a concentration factor of 12.5. No flattening mechanism is proposed for this array, however.

## 4.4 Tile Design Concept

In the present satellite design concept, a tile is the basic unit of power generation and transmission. Each tile measures  $10\text{ cm} \times 10\text{ cm}$  in plane. The out-of-plane deployed dimension has a strong dependence on the transmitting frequency, which is as yet undecided, but is expected to be around 10 GHz. For this choice of transmission frequency, the tile has an out-of-plane dimension of around 3 cm. This tile concept was generated as a collaborative effort between the Atwater, Hajimiri, and Pellegrino research groups at the California Institute of Technology.

As shown in Figure 4.4, each tile has five half-parabolic linear trough concentrators that focus light onto thin-film photovoltaic cells attached to the edge of the adjacent concentrator. This optical configuration is similar to that of the FAST array [63], though the tiles operate at a higher concentration factor, and are capable of flattening. The concentrators focus light onto a narrow photovoltaic cell, as shown in Figure 4.4. In addition to focusing light, each concentrator also acts as a thermal conduit and radiator; the thermally conductive reflective layer transports waste heat away from the PV cell at the tip and radiates it to space.

These concentrators are supported by a ground layer. The ground layer provides an attachment point for the rest of the tile components, houses the antenna ground plane, and is used for routing generated power and signals. It also holds an integrated circuit that synthesizes a microwave signal, and amplifies it using generated power. The ground plane antenna also acts a thermal conduit and radiator, removing waste heat from the integrated circuit at the center. Below the ground layer is an antenna, through which the amplified signal is transmitted.

The tile can flatten for packaging. As shown in Figure 4.5, the concentrator consists of a thin, aluminized polymer film supported at either end by carbon fiber springs. The concentrator edge springs have the appropriate parabolic profile needed for concentration. At the top edge, there is a thin carbon fiber rod attached to the concentrator that maintains straightness. Each concentrator

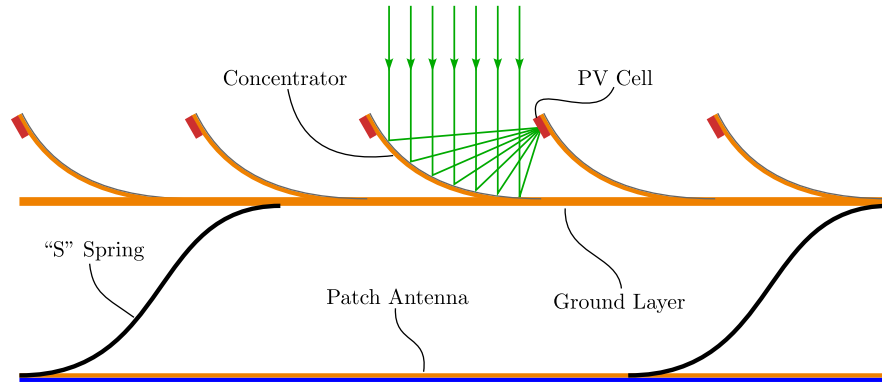


Figure 4.4: Cross section of a single tile. Each tile has five linear parabolic trough concentrators that focus light onto PV cells, a ground layer, and an antenna layer.

is able to elastically flatten; the edge springs deform from their unstressed parabolic shape to flat. The patch antenna is held below the ground layer by four carbon fiber springs that have an “S” profile, and these springs can flatten such that the patch antenna plane rests directly below the ground layer. Figure 4.5 shows an initial mechanical mockup.

These tiles are functionally independent, and require no bulky power interconnections. Power generated by a tile is transmitted by the same tile. Only low-power data and timing signals need to be exchanged between tiles.

Initial tile mockups, shown in Figure 4.5, were constructed thus: the ground layer was constructed using 7.5  $\mu\text{m}$ -thick polyimide film (Dupont Kapton<sup>®</sup> HN film), supported at the edges by a frame of 120  $\mu\text{m}$ -thick pultruded carbon fiber rods. The patch antenna layer was built using a similar technique, using 7.5  $\mu\text{m}$ -thick polyimide film and a pultruded carbon fiber rod frame. The ground and antenna layers have representative conductive aluminum layers deposited on them. The “S” springs were constructed using carbon fiber composite material.

The concentrators were made using aluminized 25  $\mu\text{m}$ -thick polyester film (Mylar<sup>®</sup>), supported at the edges by carbon fiber composite springs. A pultruded carbon fiber rod was attached to the front surface, along the top edge of the concentrator, and a strip of photovoltaic material was attached to the back surface, along the top edge. The tile mockup can flatten and then elastically pop back into its operational state.

This mockup includes an integrated circuit and five photovoltaic cells. However, these components are simply mass and structural simulators, and not intended for operation.

The initial 10 cm  $\times$  10 cm tile mockup has a mass of 1.56 g. The tile mass is expected to decrease to at least 0.8 g, allowing the overall spacecraft areal density to reach its goal of 100 g m<sup>-2</sup>.

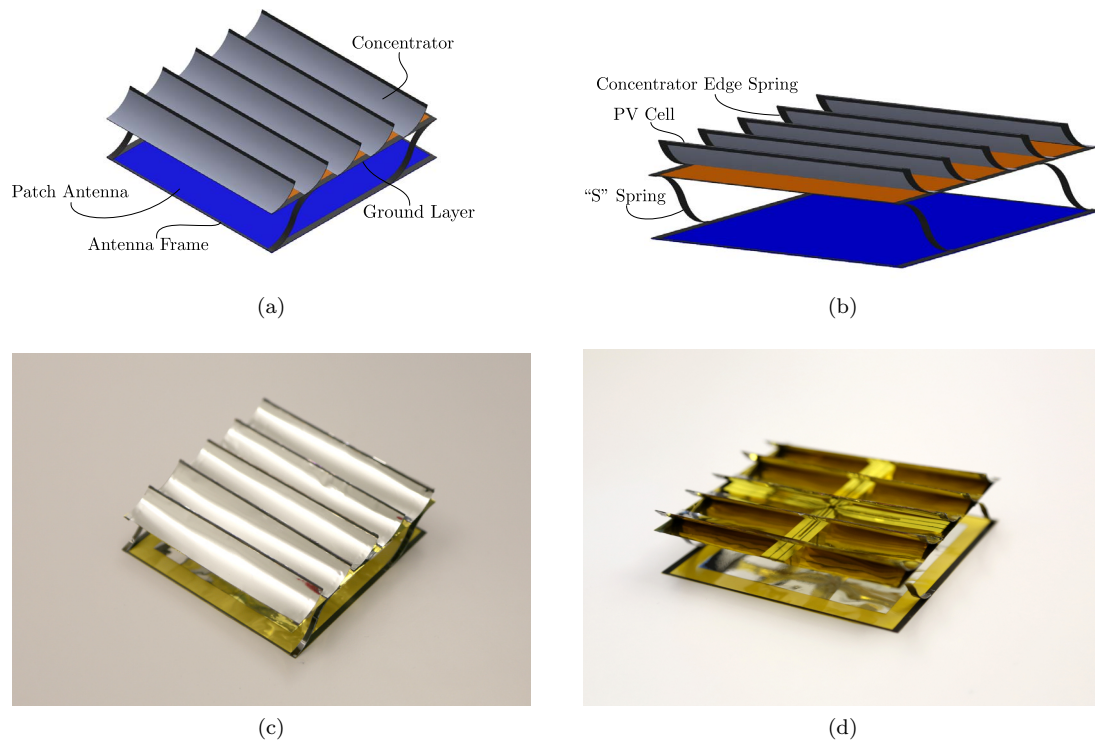


Figure 4.5: Tile design and mockup.

## 4.5 Space Solar Power Satellite Structural Design

The spacecraft is designed to be packaged by star folding and wrapping, as described in Section 3.1. It consists of many strips, arranged in concentric squares, as shown in Figure 4.6. Its structural architecture is as described in Section 3.2.2; these strips have out-of-plane bending stiffness, and they are pinned at either end to diagonal cords. At one end, the diagonal cords are attached to a central hub, and at the other end, the diagonal cords are connected to tips of deployable booms. After deployment, the diagonal cords are tensioned. The booms, clamped to the hub at the center, are located along the diagonals of the squares. In addition to supporting the diagonal cords when deployed, these booms provide the motive action during deployment. Each strip is connected to its neighboring strips using ligaments, which implement the slipping folds crucial to the packaging scheme.

The strips carry the tiles; Figure 4.7 shows a segment of a strip. Two *longerons* run the entire length of the strip and support its edges. *Battens* connect the tiles to the longerons, and the longerons to each other. The out-of-plane bending stiffness of the strips is provided primarily by the edge longerons. To enable the spacecraft packaging scheme, these longerons can be flattened and rolled [64]. There are many existing structural elements that would suffice as longerons, e.g., STEM booms [65], lenticular booms [66], and TRAC booms [41]. The current strip design calls for carbon

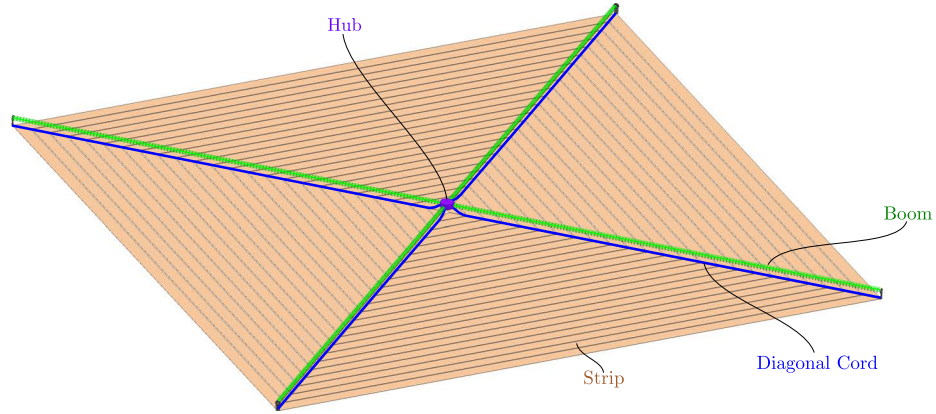


Figure 4.6: Spacecraft structural architecture.

fiber reinforced polymer (CFRP) TRAC longerons, since the TRAC structure is simpler and has a smaller packaged height.

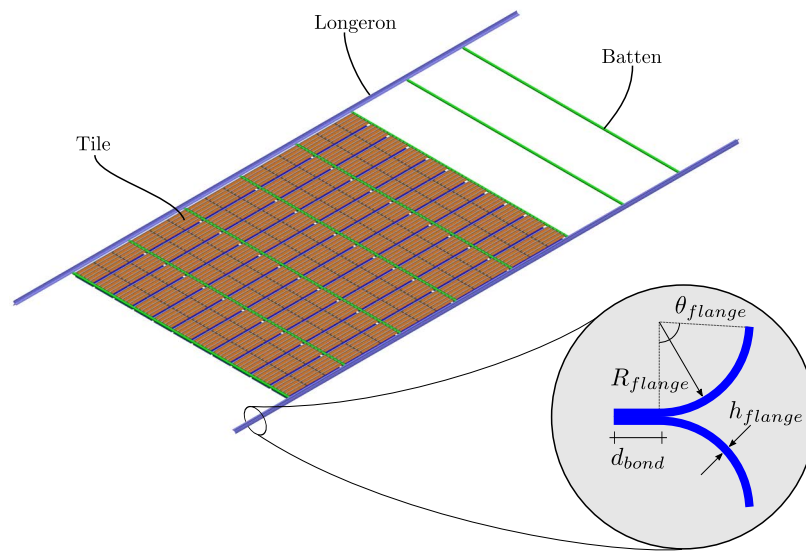


Figure 4.7: A short segment of a single strip. The longeron has a cross-section similar to a TRAC boom. For clarity, some of the tiles have been omitted.

As shown in the inset in Figure 4.7, the TRAC cross-section has the following controlling parameters: the flange thickness  $h_{flange}$ , the flange radius  $R_{flange}$ , the flange opening angle  $\theta_{flange}$ , and the bond section width  $d_{bond}$ . Appendix D calculates the relevant properties for a TRAC cross-section.

#### 4.5.1 Numerical Structural Model

To design the individual structural elements that comprise this architecture, the structural model that was described in Section 3.2.2 was implemented in MATLAB. This numerical model was used

to optimize the spacecraft structure, using a loading case and performance metric described below.

The strips were modeled as beams. The ligament connections between the strips were not accounted for in this initial model. The diagonal cords were modeled as lines under tension, and the booms were modeled as beam-columns. For fixed side length  $L = 60$  m, this simplified model has only four structural parameters that control the deflected shape of the spacecraft: the bending stiffness of the boom  $EI_{boom}$ , the bending stiffness of a strip  $EI_{strip}$ , the number of strips in a quadrant  $n$ , and the diagonal cord tension  $T$ .

The spacecraft side length is not taken to be a design parameter; it is fixed at 60 m. This is because the choice of this dimension has effects beyond what can be captured using the present performance metrics. It affects, for instance, the total number of launches needed to build a  $3 \text{ km} \times 3 \text{ km}$  array in orbit, the attitude control strategies for each spacecraft, and the formation flying algorithms. The effects of varying this dimension are not solely structural concerns, and they must be captured by a system-level model, which is outside the scope of this chapter.

### 4.5.2 Spacecraft Loading

The loading experienced by the spacecraft during operations can be divided into two classes: dynamic and quasi-static.

Expected sources of dynamic loading during operations are attitude control forces (e.g., impulse thruster firings), vibrational noise from attitude control actuators (e.g., reaction wheels or control moment gyros), and thermal shocks as the satellite moves in and out of eclipse.

Many aspects of the satellite attitude control system are not yet fully specified, and therefore it is difficult to estimate the amplitude and frequency content of the associated loads. However, it will be assumed that the attitude control system has been designed to decouple structural dynamics from the spacecraft attitude dynamics, and thus the attitude control forces will be small. This is a standard technique in the design of attitude control system for flexible spacecraft [67]. Additionally, the actuators can be isolated from the structure using dampers, and thus the vibrational noise from these sources can be reduced. This class of loads will not be considered for this preliminary analysis.

Thermal shocks occur each time the satellite transitions from being in the shadow of a celestial body (e.g., the Earth or the Moon) to being in sunlight, or vice versa. For a satellite in a geostationary orbit, there are two eclipse periods, situated around the vernal and autumnal equinox, during which the satellite is in eclipse for periods up to 70 minutes. It is expected that the satellite will not operate during these eclipses; it can also be left inoperational for a period of time following the eclipse to return to a steady thermal state. Thus thermal shocks will not be considered for this preliminary analysis.

Expected sources of quasi-static loading are either external, e.g., solar radiation pressure (SRP), gravity gradient, and inertial forces produced during accelerations, or internal, e.g., thermal loads,

mechanical loads due to manufacturing errors, or electrostatic self-attraction. The internal forces are highly dependent on the construction of these satellites and will not be considered here. The other three sources of loading – SRP, gravity gradient, and inertial forces – are considered below. SRP is found to be the dominant loading case.

A perfectly reflective surface, 1 AU from the Sun, with a solar incidence angle  $\alpha$  relative to the surface normal, is subject to radiation pressure  $B_{SRP}$  that acts normal to the surface [68]:

$$B_{SRP} = \frac{2E_f}{c} \cos^2 \alpha \quad (4.1)$$

where  $E_f = 1361 \text{ W m}^{-2}$  is the solar energy flux at 1 AU, and  $c = 3.00 \times 10^8 \text{ ms}^{-1}$  is the speed of light. Assuming the spacecraft surface to be a perfect reflector, and oriented normal to the sun angle, a surface-normal SRP load of  $B_{SRP} = 9.1 \times 10^{-6} \text{ Pa}$  is obtained.

The inertial forces due to rotational acceleration can be estimated by assuming a minimum-time acceleration profile to slew the satellite through an angle  $\Delta\theta$  in a given time  $\Delta t$ . These calculations are based on similar analysis performed by Dr. Nicolas Lee while he was a postdoctoral fellow at the California Institute of Technology. For this maneuver the angular acceleration is some value  $\ddot{\theta}_{max}$  for half the time  $t \in [0, \Delta t/2]$  and its negative  $-\ddot{\theta}_{max}$  for the other half of the time  $t \in (\Delta t/2, \Delta t]$ :

$$\ddot{\theta}(t) = \begin{cases} \ddot{\theta}_{max} & \text{if } t \in [0, \Delta t/2] \\ -\ddot{\theta}_{max} & \text{if } t \in (\Delta t/2, \Delta t] \end{cases} \quad (4.2)$$

Integrating, this gives the following angular velocity profile (assuming no initial angular velocity, i.e.,  $\dot{\theta}(0) = 0$ ):

$$\dot{\theta}(t) = \begin{cases} \ddot{\theta}_{max} t & \text{if } t \in [0, \Delta t/2] \\ \ddot{\theta}_{max} (\Delta t - t) & \text{if } t \in (\Delta t/2, \Delta t] \end{cases} \quad (4.3)$$

Integrating once more to obtain the angle profile:

$$\theta(t) = \begin{cases} \frac{1}{2} \ddot{\theta}_{max} t^2 + \theta(0) & \text{if } t \in [0, \Delta t/2] \\ \frac{1}{2} \ddot{\theta}_{max} (-t^2 + 2\Delta t t - \frac{1}{2} \Delta t^2) + \theta(0) & \text{if } t \in (\Delta t/2, \Delta t] \end{cases} \quad (4.4)$$

The total slew angle for this maneuver  $\Delta\theta$  is obtained as

$$\Delta\theta = \theta(\Delta t) - \theta(0) = \frac{1}{4} \ddot{\theta}_{max} \Delta t^2 \quad (4.5)$$

Given these angular acceleration and velocity profiles, the associated inertial forces acting on the

satellite can be calculated. To compare to the SRP value obtained above, these forces are expressed as pressures, i.e., forces per unit planar area. At a point some distance  $r$  from the axis of rotation, the pressure due to the centrifugal forces  $B_{I,\parallel} = \rho_A \dot{\theta}^2 r$  acts in the plane of the satellite, and the pressure from the Euler forces  $B_{I,\perp} = \rho_A \ddot{\theta} r$  acts out of the plane [69].  $\rho_A$  is the satellite areal density; it is assumed to be uniform. Maximum pressures occur at the largest distance from the axis of rotation; this happens when the module slews about one of the diagonals, and  $\max(r) = L/\sqrt{2}$ . The maximum in-plane pressure  $B_{I,\parallel}$  occurs when angular velocity  $\dot{\theta}$  is maximum; from Equation (4.3) this happens at  $t = \Delta t/2$  and  $\max(\dot{\theta}) = \ddot{\theta}_{max} \Delta t/2$ . Since  $|\ddot{\theta}|$  is constant, the centrifugal pressure is constant in time. Thus, the maximum pressures are as follows:

$$\max B_{I,\parallel} = \rho_A \frac{L}{\sqrt{2}} \left( \frac{\ddot{\theta}_{max} \Delta t}{2} \right)^2 \quad (4.6)$$

$$\max B_{I,\perp} = \rho_A \frac{L}{\sqrt{2}} \ddot{\theta}_{max} \quad (4.7)$$

Using Equation (4.5) to substitute for  $\ddot{\theta}_{max}$ ,

$$\max B_{I,\parallel} = \rho_A \frac{L}{\sqrt{2}} \left( \frac{2\Delta\theta}{\Delta t} \right)^2 \quad (4.8)$$

$$\max B_{I,\perp} = \rho_A \frac{L}{\sqrt{2}} \left( \frac{4\Delta\theta}{\Delta t^2} \right) \quad (4.9)$$

Figure 4.8 plots these maximum pressures due to inertial forces for slew angles  $\Delta\theta \in [0^\circ, 90^\circ]$  and slew times  $\Delta t \in [0.5 \text{ h}, 6 \text{ h}]$ , for a spacecraft areal density  $\rho_A = 100 \text{ g m}^{-2}$  and  $L = 60 \text{ m}$ . In the current operational scenario, the spacecraft is not expected to slew by more than  $45^\circ$  in 1 h; for these values, Equation (4.8) and Equation (4.9) provide upper bounds on in-plane pressure  $\max B_{I,\parallel} = 8 \times 10^{-7} \text{ Pa}$  and out-of-plane pressure  $\max B_{I,\perp} = 1 \times 10^{-6} \text{ Pa}$ , respectively. These loads are about 9 times smaller than the SRP loading.

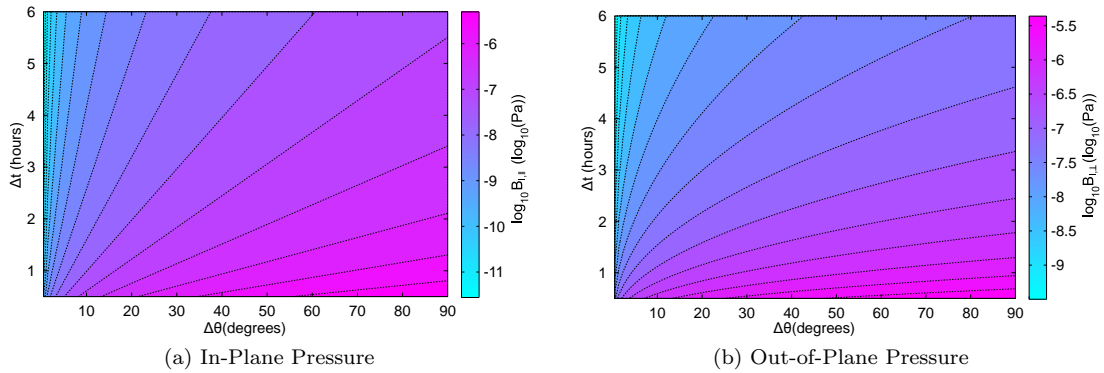


Figure 4.8: Inertial pressures on a spacecraft with  $L = 60 \text{ m}$  and areal density  $\rho_A = 100 \text{ g m}^{-2}$  for a variety of minimum-time slew maneuvers. The pressures are plotted in logarithmic form.

Turning to the task of estimating the gravity gradient loads, consider the spacecraft to have tilted from the local horizontal plane by an angle  $\theta$ . Again, these calculations closely follow similar analysis performed by Dr. Nicolas Lee. As shown in Figure 4.9, this tilt produces differential gravity at all locations that rotate out of the local horizontal plane. The center of mass of the spacecraft is located at  $\vec{R}_0$  relative to the center of the Earth. It is subject to gravitational acceleration  $\vec{a}$ :

$$\vec{a} = GM_{\oplus} \frac{\vec{R}_0}{R_0^3} \quad (4.10)$$

where  $G = 6.674 \times 10^{-11} \text{ N m kg}^{-2}$  is the gravitational constant, and  $M_{\oplus}$  is the mass of the Earth. Define a point on the spacecraft by the vector  $\vec{r}$  relative to the center of mass; thus its location relative to Earth's center is

$$\vec{R} = \vec{R}_0 + \vec{r} \quad (4.11)$$

The differential acceleration felt by this point at  $\vec{r}$  is

$$\vec{a}_{GG} = GM_{\oplus} \left( \frac{\vec{R}_0}{R_0^3} - \frac{\vec{R}}{R^3} \right) \quad (4.12)$$

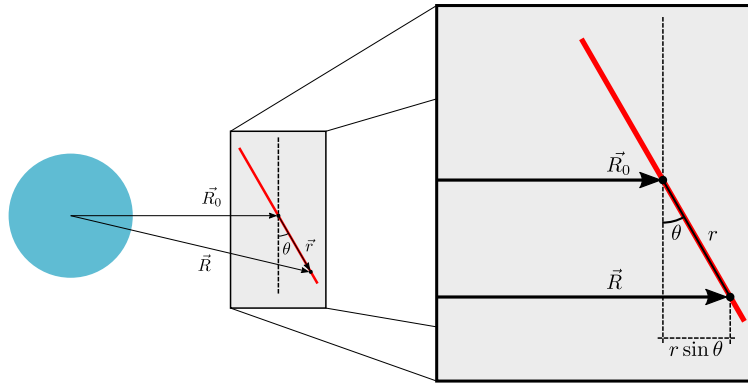


Figure 4.9: A tilt  $\theta$  from the local horizontal (indicated by the dashed lines) produces a gravity gradient pressure.

Since the spacecraft is much smaller than the orbital radius (i.e.,  $r \ll R_0$ ), Equation (4.12) can be linearized. This is done by zooming into the local horizontal frame of reference, as shown in the inset in Figure 4.9, where  $\vec{R}$  and  $\vec{R}_0$  are nearly parallel, and their lengths differ by  $r \sin \theta$ :

$$R = R_0 + r \sin \theta \quad (4.13)$$

Using this, Equation (4.12) can be cast into a scalar form:

$$a_{GG} = GM_{\oplus} \left( \frac{1}{R_0^2} - \frac{1}{(R_0 + r \sin \theta)^2} \right) \quad (4.14)$$

Multiplying the above expression by the areal density  $\rho_A$  gives a gravity gradient pressure that can be used to compare this loading case to SRP and rotational inertial pressures:

$$B_{GG} = GM_{\oplus} \rho_A \left( \frac{1}{R_0^2} - \frac{1}{(R_0 + r \sin \theta)^2} \right) \quad (4.15)$$

Decomposing this pressure into in- and out-of-plane components:

$$B_{GG,\parallel} = GM_{\oplus} \rho_A \left( \frac{1}{R_0^2} - \frac{1}{(R_0 + r \sin \theta)^2} \right) \sin \theta \quad (4.16)$$

$$B_{GG,\perp} = GM_{\oplus} \rho_A \left( \frac{1}{R_0^2} - \frac{1}{(R_0 + r \sin \theta)^2} \right) \cos \theta \quad (4.17)$$

These expressions attain their maxima at extremal points on the spacecraft, i.e., at  $r = L/\sqrt{2}$ . The parallel component of the gravity gradient pressure,  $B_{GG,\parallel}$  is maximum at  $\theta = 90^\circ$ , and the perpendicular component  $B_{GG,\perp}$  is maximum at  $\theta = 45^\circ$  (for  $r \ll R_0$ ):

$$\max B_{GG,\parallel} = GM_{\oplus} \rho_A \left( \frac{1}{R_0^2} - \frac{1}{(R_0 + L/\sqrt{2})^2} \right) \quad (4.18)$$

$$\max B_{GG,\perp} = \frac{1}{\sqrt{2}} GM_{\oplus} \rho_A \left( \frac{1}{R_0^2} - \frac{1}{(R_0 + L/2)^2} \right) \quad (4.19)$$

Evaluating these expressions for a geostationary orbit i.e.,  $R_0 = 42\,164$  km, module side length  $L = 60$  m, and an areal density of  $\rho_A = 100$  g m<sup>-1</sup>:

$$\max B_{GG,\parallel} = 4.5 \times 10^{-8} \text{ Pa} \quad (4.20)$$

$$\max B_{GG,\perp} = 2.3 \times 10^{-8} \text{ Pa} \quad (4.21)$$

These gravity gradient pressures are two orders of magnitude less than the SRP. Given that the rotational inertial pressures are also lower than the SRP, by about a factor of 9, SRP will be taken as the dominant loading case for which the preliminary structural design will be constructed.

### 4.5.3 Performance Metric

A key metric in the design of the spacecraft is the specific power, which is the amount of power delivered to the ground station per unit mass of spacecraft. Since the present exercise deals exclu-

sively with the structural design, the effects of the structural design on the specific power will be isolated and considered independently. In particular, the effects of structural deflections on power generation and transmission are considered, as is the mass of the structural components.

The most efficient tile arrangement is with all tiles pointed directly at the sun (which maximizes power generation efficiency), arrayed regularly in a single plane (which maximizes power transmission efficiency). Any angular deviations from such an arrangement will reduce the performance of the concentrators, and any translational deviations will reduce the performance of the microwave phased array.

If the translational deviations are small enough and slow enough, they can be measured and corrected for by introducing appropriate phase delays at each tile location. A system to perform these measurements and corrections will need to be implemented. Thus, the present structural design exercise will consider only the effect of angular deviations from the nominal planar configuration of the tiles.

The performance metric used to evaluate the structural design is the *specific concentrated power*: the total power concentrated on the photovoltaic cells divided by the total mass of the spacecraft. The total concentrated power depends on the incoming solar power flux (taken to be constant at  $1361 \text{ W m}^{-2}$ ) and the average tile concentrating efficiency.

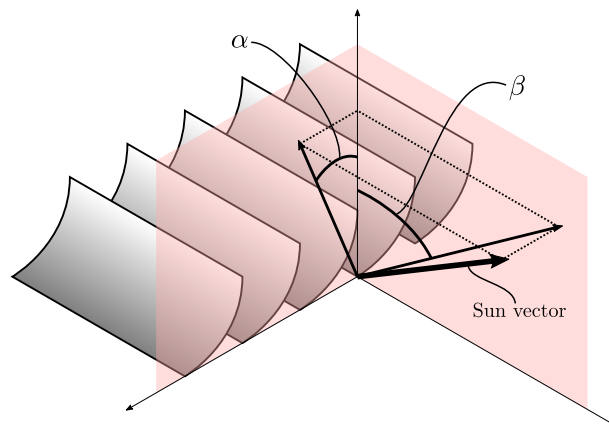


Figure 4.10: The sun vector at each tile is decomposed into a component in the plane of concentration, at an angle  $\alpha$  to the tile normal, and a component perpendicular to the plane of concentration, at an angle  $\beta$ .

The performance of the concentrators in the tiles depends on the local sun angle. As shown in Figure 4.10, the local sun vector can be decomposed into a component within the plane of concentration, and a component perpendicular to this plane. The optical efficiency of the concentrators depends on the  $\alpha$  and  $\beta$  angles these components make with the local tile normal. As seen in Figure 4.11, the sensitivity of the concentrating efficiency to  $\alpha$  is much greater than the sensitivity to  $\beta$ .

In the present study, the concentrators across the entire spacecraft were arranged to be all

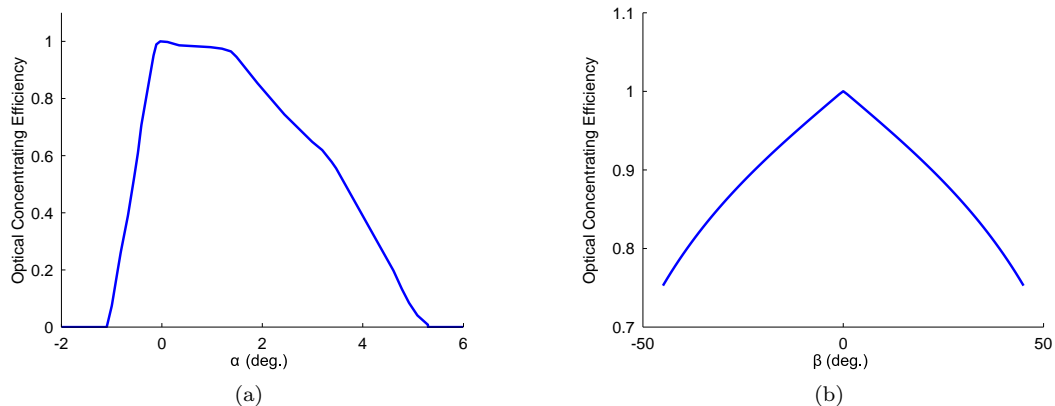


Figure 4.11: Tile concentrating efficiency variation with incident sun angles  $\alpha$  and  $\beta$ . The data for these plots was provided by Drs. Pilar Espinet and Dennis Callahan from the research group of Dr. Harry Atwater.

parallel. This is because the concentrators are much more sensitive to the  $\alpha$  angle than the  $\beta$  angle. Thus, the spacecraft can slew in a manner that changes the  $\beta$  angle without greatly affecting the concentrating efficiency. If (as an alternative) the tiles were arranged in a 4-fold symmetric manner, the spacecraft would have to remain very closely sun-pointed (being able to deviate less  $1^\circ$  in either axis) to generate any power from more than half the tiles. But since the concentrators are all parallel, the spacecraft can slew  $\pm 20^\circ$  in the  $\beta$  direction allowing for operational freedom.

For this initial analysis, it is assumed that the spacecraft is pointed directly at the sun. Due to solar radiation pressure, the structure deflects out-of-plane. To compute these deflections, the structural model in Section 3.2.2 was used.

To find the  $\alpha$  and  $\beta$  angles at a tile on the  $i^{th}$  strip at a location  $x$  along the strip, the local tile normal  $\mathbf{n}_t(x; i)$  was computed by tilting the undeflected normal  $\{0, 0, 1\}^T$  through two rotations:  $\mathbf{R}_1$  due to the diagonal cord deflections by an angle  $(u_{DC,i-1} - u_{DC,i}) / \sqrt{2}w$ , and  $\mathbf{R}_2$  due to the strip deflections by an angle  $u'_{strip,i}(x)$ .  $u_{DC,i}$  is the vertical deflection of the  $i^{th}$  node of the diagonal cord, and  $u_{strip,i}(x)$  is the vertical deflection of the  $i^{th}$  strip at a point  $x$  along the strip. These variables are defined and evaluated in Section 3.2.2.

Using the curves shown in Figure 4.11, the efficiencies due to these angular deformations were found, and the tile concentrating efficiency was computed as the product of these efficiencies. The average tile concentrating efficiency over the entire spacecraft was then evaluated, and multiplied by the spacecraft area and solar flux to compute the total concentrated power.

The other component of the performance metric is the spacecraft mass  $m$ . It was estimated by accounting for the mass of the tiles ( $m_{tiles}$ ), the hub ( $m_{hub}$ ), the strip structure (excluding the tiles)

( $m_{strips}$ ), the booms ( $m_{booms}$ ), and the diagonal cords ( $m_{cords}$ ).

$$m = m_{tiles} + m_{hub} + m_{strips} + m_{booms} + m_{cords} \quad (4.22)$$

The tile mass was calculated by multiplying the expected tile areal density of  $80 \text{ g m}^{-2}$  by the total spacecraft area. The tile mass does not change with changes in the structural design of the spacecraft:

$$m_{tiles} = \sigma_{tiles} L^2 = 80 \text{ g m}^{-2} \times (60 \text{ m})^2 = 288 \text{ kg} \quad (4.23)$$

The hub mass was assumed to be fixed:  $m_{hub} = 50 \text{ kg}$ . This estimate is based on the use of nanosatellite components and includes the propulsion system.

The mass of the strip structure was calculated by multiplying the mean linear density of the strip  $\lambda_{strip}$  and the total strip length  $L_{strip}$ . The total strip length  $L_{strip}$  is four times the sum of the lengths of the  $n$  strips in a single quadrant:

$$L_{strip} = 4 \sum_{i=1}^n L_i \quad (4.24)$$

where  $L_i$  is the length of the  $i^{th}$  strip, measured at the center line of the strip. Assuming that there is no hole in the center of the module, this length is

$$L_i = \frac{L}{n} \left( i - \frac{1}{2} \right) \quad (4.25)$$

By substituting Equation (4.25) into Equation (4.24), the total strip length can be calculated from

$$L_{strip} = 2Ln \quad (4.26)$$

The average strip linear density  $\lambda_{strip}$  accounts for the linear density of the each longeron  $\lambda_{longeron}$ , and also the mass of the battens. The mass of a batten is  $\lambda_{batten} w$  where  $\lambda_{batten}$  is the linear density of the batten, and its length is the strip width  $w$ . (For this module with no central hole, the strip width is  $w = L/2n$ .) To include this batten mass into the strip linear density, it must be spread out over distance between successive battens. This distance, the batten pitch  $p_{batten}$ , is taken to be constant over the module. This gives the average strip linear density:

$$\lambda_{strip} = 2\lambda_{longeron} + \lambda_{batten} \frac{L}{2n} \frac{1}{p_{batten}} \quad (4.27)$$

The batten linear density  $\lambda_{batten}$  was taken to be  $0.16 \text{ g m}^{-1}$  based on a CFRP construction (with volumetric density  $1600 \text{ kg m}^{-3}$ ) and a rectangular cross section of  $100 \mu\text{m} \times 1 \text{ mm}$ . The batten pitch

was fixed at  $p_{batten} = 30$  cm. The longeron linear density  $\lambda_{longeron}$  is calculated as the product of the longeron cross-sectional area and the material volumetric density (taken to be CFRP at  $1600 \text{ kg m}^{-3}$ ). CFRP was used as a material for the battens and longerons in this initial analysis due to its stiffness, strength, and low density.

The boom mass was estimated by using a homogenized linear density ( $\lambda_{boom}$ ).

The diagonal cord mass was calculated by estimating an appropriate cross-sectional area (taken to be the area that results in 0.1% strain given the desired diagonal cord pre-tension  $T$ ), and using this area to calculate the diagonal cord linear density (using a volumetric density of  $1600 \text{ kg m}^{-3}$ ).

#### 4.5.4 Structural Design Results

For initial modeling efforts, the booms were assumed to have the properties of the ATK Coilable Boom for the ST8 Sailmast with  $(EI)_{boom} = 8035 \text{ N m}^2$  and  $\lambda_{boom} = 70 \text{ g m}^{-1}$  [70]. Coilable booms such as the ST8 Sailmast are attractive due to their low linear densities and design maturity; they can serve as initial design points. Thus, the number of inputs to the optimization procedure is reduced to three: number of strips per quadrant  $n$ , diagonal cord tension  $T$ , and strip bending stiffness  $(EI)_{strip}$ . Additionally,  $n$  can only take on integer values. Given this, a simple grid search was able to find the optimal design at  $n = 20$ , diagonal cord tension  $T = 3.84 \text{ N}$ , and strip bending stiffness  $(EI)_{strip} = 10.78 \text{ N m}^2$ . Figure 4.12 shows how the specific concentrated power changes with  $(EI)_{strip}$  and  $T$  around this optimum.

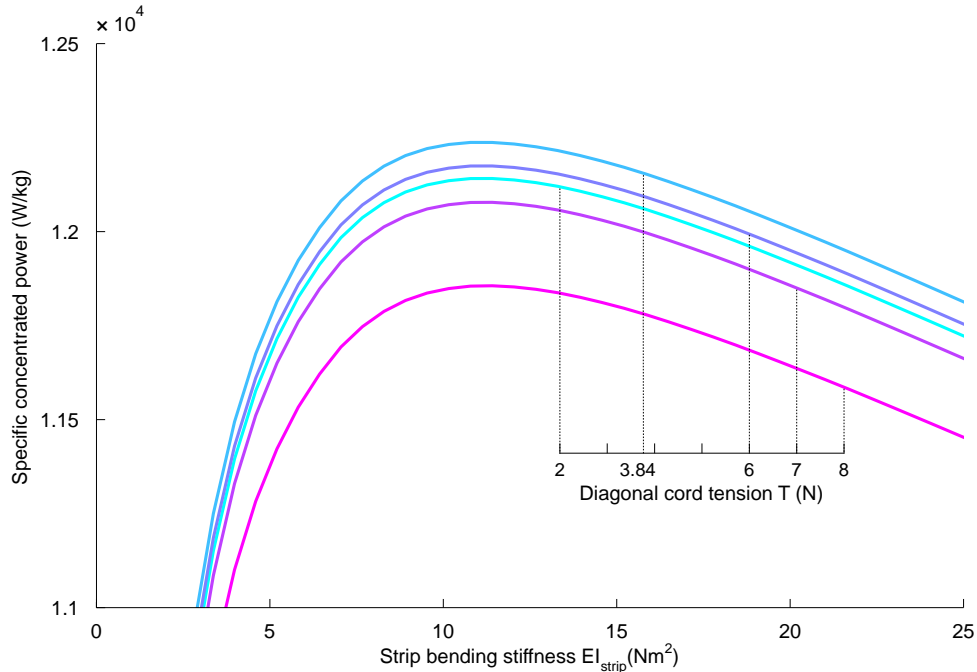


Figure 4.12: Specific concentrated power as a function of diagonal cord tension  $T$  and strip bending stiffness  $(EI)_{strip}$ .

Component	Mass (kg)	Mass fraction
Tiles	288.00	78%
Hub	50.00	14%
Strip structure	19.00	5%
Booms	11.88	3%
Diagonal cords	0.01	0.003%
<b>Total</b>	<b>368.89</b>	

Table 4.1: Spacecraft mass breakdown.

Increasing the diagonal cord tension initially stiffens the spacecraft; after a certain point, however, increased compression in the boom reduces its effective bending stiffness, resulting in greater deflections. Increasing the strip bending stiffness also results in initial increases in specific concentrated power, but after a certain point, the mass growth due to larger TRAC boom cross-sections outpaces the growth in collected power from lower deflections.

To achieve the desired strip bending stiffness of 10.78 N m, the two longerons supporting the strip each have a bending stiffness of half this value, i.e., 5.39 N m. Assuming a longitudinal material modulus of 140 GPa (typical of carbon fiber composites), a TRAC cross-section with a flange radius of 10 mm and a flange thickness of 68.5  $\mu\text{m}$  was designed to provide this bending stiffness.

The mass breakdown of the spacecraft is shown in Table 4.1. This mass breakdown does not include margins; it represents a theoretically attainable lower limit on the mass of such spacecraft.

## 4.6 Spacecraft Packaging

A TRAC flange thickness of 68.5  $\mu\text{m}$  leads to a flattened longeron thickness of 137  $\mu\text{m}$ . Assuming the flattened tiles and the flattened battens are thinner than the flattened longerons, the flattened strip thickness can be taken to be  $h = 137 \mu\text{m}$ . Since  $L = 60 \text{ m}$ , the length-to-thickness ratio is  $\lambda = 10^{5.64}$ .

The minimum radius  $R_{min}$  can be calculated by considering the maximum strain in the wrapped longerons. The longerons are assumed to have a uniaxial strain limit of 1%, with an additional factor of safety of 2 against material failure, thus  $\epsilon_{max} = 0.5\%$ . This gives the minimum radius of curvature  $R_{min}$ :

$$\frac{R_{min}}{h} = \frac{1}{2\epsilon_{max}} = 100 \Rightarrow R_{min} = 13.7 \text{ mm} \quad (4.28)$$

The upper bounds on the packaged dimensions of the spacecraft can be estimated using the kinematic model presented in Section 3.1.3 for a structure with  $N = 4$ ,  $n = 20$ ,  $\lambda = 10^{5.64}$ , and  $R_{min}/h = 100$ : a cylinder with diameter of 0.92 m and a height of 1.50 m. A cross-sectional view of this cylinder is shown in Figure 4.13. In this packaged form, the maximum slip can be estimated

using Equation (2.22) to be at least  $l_{max} = 16.8$  mm. This informs the design of the ligaments connecting the strips, as they must be able to provide at least this degree of slip.

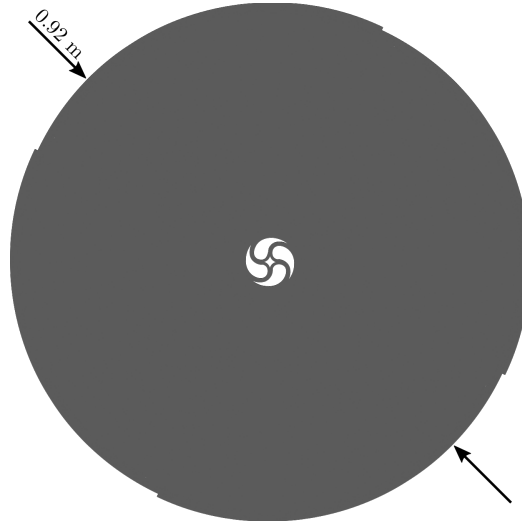


Figure 4.13: Cross-section of the packaged spacecraft.

## 4.7 Spacecraft Design Summary

This chapter has presented a preliminary structural design of a spacecraft that carries many modular multifunctional tiles. A formation of these spacecraft is envisioned to capture solar power in space, and transmit it to a ground station on the Earth.

A design concept for these multifunctional  $10\text{ cm} \times 10\text{ cm}$  tiles, each of which is capable of power generation and transmission, was described. These tiles are expected to be very lightweight; an initial mockup with a mass of  $1.56\text{ g}$  was constructed, and this mass is expected to decrease by a factor of about 2. A structural framework was designed, using solar radiation pressure as a loading case and specific concentrated power as a performance metric, to hold these tiles in a planar configuration.

The final result is an ultra-lightweight spacecraft that measures  $60\text{ m} \times 60\text{ m}$ , has a mass of  $369\text{ kg}$ , and can be packaged into a cylinder with diameter of  $0.92\text{ m}$  and a height of  $1.50\text{ m}$ .

## Chapter 5

# Conclusions

At the outset, four challenges associated with the packaging and deployment of large planar structures were posed: biaxial compaction, efficient packaging, packaging without permanent deformation, and deployment with low and predictable forces. This thesis presented two novel classes of methods for packaging large planar structures that simultaneously address each of these challenges.

These methods provide biaxial compaction by packaging structures with comparable in-plane dimensions and large area into cylindrical forms. In both of the classes of packaging methods, slipping folds are used to fold the structure; the first class of methods uses parallel slipping folds to z-fold the structure, and the second class uses folds arranged in concentric polygons to star-fold the structure. Once folded, the structure can be wrapped into a cylindrical package.

These methods are highly efficient at packaging; there are minimal voids in the packaged form, and the volume of these voids decreases in comparison to the volume of the packaged material for very large or very thin structures. At these scales, packaging efficiencies approach 100%. These packaging methods were demonstrated experimentally using meter-scale test articles. These tests demonstrated the feasibility of these packaging methods and validated the analytical tools that were developed to predict packaged shapes. Packaging efficiencies of up to 83% were obtained for these lab-scale models.

The maximum strains in the packaged form can be predicted analytically and thus packaging can be achieved such that the structure remains elastic throughout. This allows a structure to be packaged and deployed without damage or permanent deformation. These packaging methods scale according to the material thickness, and are applicable to a wide range of material thicknesses. This allows for the packaging of not only membrane structures, but also thicker structures with finite bending stiffness.

Methods for deploying these structures were also described. These methods were experimentally demonstrated, showing controlled and repeatable deployment. Deployment was conducted on both membrane test articles and test articles with thin-shell elements that provide structural bending stiffness.

Structural architectures were put forward that are compatible with these methods of packaging and deployment. One set of architectures pretension the structure to obtain out-of-plane stiffness; these architectures are suitable for membrane structures. A second type of architecture uses the bending stiffness of strips with thin-shell elements to react out-of-plane loads. Preliminary analytical models were constructed to describe these structural architectures. Meter-scale physical models that typify these architectures were constructed; these models demonstrated feasibility of these structural architectures, and their compatibility with the packaging and deployment schemes.

These concepts, analytical tools, and methods enable the design of large space structures, such as solar power arrays, reflectarray antennas, solar sails, and drag sails. This thesis applied a particular packaging concept and structural architecture to the initial structural design of a  $60\text{ m} \times 60\text{ m}$  space solar power satellite. The resulting spacecraft design concept is lightweight, with areal density of  $\approx 100\text{ g m}^{-2}$ , stiff enough to enable operation under dominant loading conditions, and packages into a cylindrical volume  $\approx 1\text{ m}$  in diameter and  $1.5\text{ m}$  in height.

## 5.1 Open Questions

Over the course of this study, several questions were raised that are outside the scope of this thesis. These questions warrant further investigation.

To eye, the physical models used throughout this thesis appeared undamaged after packaging and deployment, but the degree to which they recovered their shape and stiffness was not quantitatively measured. The as-deployed shape and stiffness of these structures must be measured, and comparisons must be made to the pre-packaged shape and stiffness.

The magnitude and distribution of forces required to hold the proposed structures in a wrapped state ought to be calculated, simulated, and measured. The proposed structures are elastically bent in the packaged configuration, storing strain energy, and forces must be applied to hold these structures contained. In order to design the containers for these structures, these forces must be known.

The packaging tests performed throughout this thesis were done, to a large extent, by hand. This manual packaging leads to variability, uncertainty, and inefficiency. More systematic and deterministic packaging methods, e.g., using mechanical wrapping apparatuses or jigs, ought to be designed and used to ensure tight packaging.

The imperfection sensitivity of the packaging and deployment behavior of such structures should be studied. For instance, the effects of the rupture of a ligament during unfolding should be considered. During deployment testing for this study, such ruptures were observed and their effects were minimal. The degree to which these structures are robust to imperfections should be quantified.

The structural analysis used in the design of the space solar power satellites should be further

advanced by considering non-linear effects e.g. the buckling of the TRAC longerons in bending, dynamic loading cases, and thermo-mechanical effects.

## 5.2 Future Work

The wrapping geometries used here are among the simplest possible. There exists a variety of forms into which such structures could be packaged that preserve the condition of zero-slip at the ends of the wrapped stack. For instance, if the available packaging volume is rectangular in form, a z-folded stack could be wrapped into a form as shown in Figure 5.1a. This form is less efficient at packaging; it has more than two voids if packaged into a rectangular form. However, the locations where the wrapped stack sees the highest curvature are at the ends of the stack, as opposed to the very center.

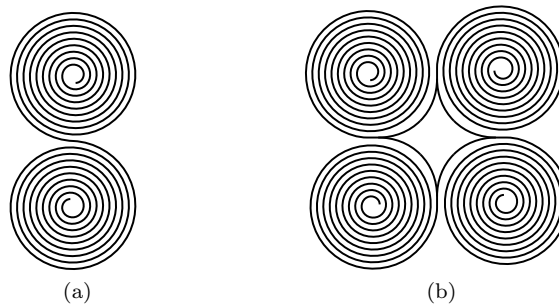


Figure 5.1: Alternative wrapping geometries for (a) a z-folded structure and (b) a star-folded structure.

These alternative wrapping geometries require alternative approaches to deployment. Some of these alternative deployment approaches may be simpler than the ones proposed here. For instance, a star-folded structure can be wrapped as shown in Figure 5.1b. This structure, held by four independent cages, can be unwrapped and unfolded in a single synchronous deployment stage.

A limitation of the mathematical model used to capture star folding and wrapping is the assumption of equal strip length. This assumption, although useful for these initial modeling efforts, limits the predictive power of the mathematical model; only lower bounds on packaging efficiency and maximum slip, and upper bounds on packaged dimensions can be provided. This assumption can be avoided by using a different kind of spiral curve that has linearly decreasing pitch with arclength, to capture the linearly decreasing thickness of the arm.

Many of the mechanical models used herein for the wrapped stack are elastic rods in bending, with the stiffness of the rod being the sum of the stiffnesses of the individual strips. In reality, each strip has slightly different curvature, and the mechanical behavior of a stack of strips is more complicated. The limits of the current modeling approach need to be identified and, if possible, a more suitable model developed.

Another possible area of exploration is using curved fold lines to simultaneously fold and wrap structures. Curved creases have been demonstrated for simple wrappings [11], but using them for symmetric wrappings would be an interesting study. Using curved fold lines may decrease the amount of slipping required during wrapping, and allow for stronger and stiffer connections between strips.

## Appendix A

# Large Deflections of an Elastic Rod in Bending

Several calculations in this thesis rely on the mechanics of an inextensible elastic rod bending through large deflections. This rod is confined to a plane, pinned at one end, and clamped at the other.

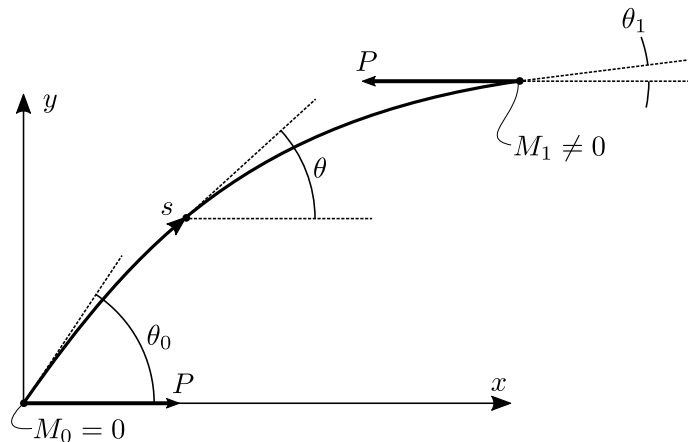


Figure A.1: An elastic rod in bending, loaded by horizontal force  $P$ .

As shown in Figure A.1, it is loaded by a point force  $\mathbf{P} = \{P, 0\}^T$ ,  $P \geq 0$  at the pinned end, has uniform bending stiffness  $D$ , and length  $L$ . The solution to this problem is given by elastica theory. Its derivation, which closely follows that of Timoshenko and Gere [40], is presented below.

The shape of the bent rod  $\{x(s), y(s)\}^T$  is parametrized by arclength  $s \in [0, L]$ . Without loss of generality, the pinned end at  $s = 0$  is taken to be the origin.

Moment equilibrium about  $\{x(s), y(s)\}^T$  of a section  $\{x(\tilde{s}), y(\tilde{s})\}^T : \tilde{s} \in [0, s]$  of the elastica dictates that

$$M = -Py \tag{A.1}$$

where  $M$  is the internal bending moment of the rod, and is related linearly to the curvature  $\kappa$  of the rod:

$$M = D\kappa = D\frac{d\theta}{ds} = -Py \quad (\text{A.2})$$

$\theta$  is the tangent angle of the rod at  $s$ . Taking a derivative with respect to  $s$ , and defining  $k^2 \equiv \frac{P}{D}$ :

$$\frac{d^2\theta}{ds^2} = -k^2 \frac{dy}{ds} \quad (\text{A.3})$$

From the theory of plane curves,  $\frac{dy}{ds} = \sin \theta$ , and thus

$$\frac{d^2\theta}{ds^2} = -k^2 \sin \theta \quad (\text{A.4})$$

Taking an indefinite integral over  $\theta$ :

$$\int \frac{d^2\theta}{ds^2} d\theta = -k^2 \int \sin \theta d\theta \quad (\text{A.5})$$

$$\Rightarrow \int \frac{d^2\theta}{ds^2} \frac{d\theta}{ds} ds = k^2 \cos \theta + C \quad (\text{A.6})$$

$$\Rightarrow \frac{1}{2} \left( \frac{d\theta}{ds} \right)^2 = k^2 \cos \theta + C \quad (\text{A.7})$$

where  $C$  is a constant that can be found by evaluating the above at the pinned end,  $\frac{d\theta}{ds} = 0 \Rightarrow C = -k^2 \cos \theta_0$ .  $\theta_0$  is the tangent angle at the origin  $\theta(s=0)$ . Continuing

$$\frac{d\theta}{ds} = \pm \sqrt{2k^2 (\cos \theta - \cos \theta_0)}^{\frac{1}{2}} \quad (\text{A.8})$$

Implementing, using  $q \equiv \sin \frac{\theta_0}{2}$ , a transformation from  $\theta$  to angular parameter  $\omega$ , defined as

$$q \sin \omega = \sin \frac{\theta}{2} \quad (\text{A.9})$$

$$\Rightarrow q \cos \omega = \frac{1}{2} \cos \frac{\theta}{2} \frac{d\theta}{d\omega} \quad (\text{A.10})$$

$$\Rightarrow \frac{d\theta}{d\omega} = 2q \cos \omega \left( \cos \frac{\theta}{2} \right)^{-1} \quad (\text{A.11})$$

$$= 2q \cos \omega \left( 1 - \sin^2 \frac{\theta}{2} \right)^{-\frac{1}{2}} \quad (\text{A.12})$$

$$= 2q \cos \omega (1 - q^2 \sin^2 \omega)^{-\frac{1}{2}} \quad (\text{A.13})$$

Using these relations to transform Equation (A.8):

$$\frac{d\theta}{ds} = \pm\sqrt{2}k (\cos\theta - \cos\theta_0)^{\frac{1}{2}} = \pm\sqrt{2}k \left(2\sin^2\frac{\theta_0}{2} - 2\sin^2\frac{\theta}{2}\right)^{\frac{1}{2}} \quad (\text{A.14})$$

$$= \pm\sqrt{2}k (2q^2 - 2q^2\sin^2\omega)^{\frac{1}{2}} \quad (\text{A.15})$$

$$= \pm 2kq \cos\omega \quad (\text{A.16})$$

Integrating to solve for  $s$ , and noting that when  $\theta = \theta_0$ ,  $\sin\omega_0 = 1$  and  $\omega_0 = \frac{\pi}{2}$ :

$$s(\theta) = \int_{\theta_0}^{\theta} \left(\frac{d\theta}{ds}\right)^{-1} d\tilde{\theta} \quad (\text{A.17})$$

$$= \int_{\pi/2}^{\omega} (\pm 2kq \cos\tilde{\omega})^{-1} \frac{d\theta}{d\omega} d\tilde{\omega} \quad (\text{A.18})$$

$$= \pm \frac{1}{k} \int_{\pi/2}^{\omega} (1 - q^2 \sin^2\tilde{\omega})^{-\frac{1}{2}} d\tilde{\omega} \quad (\text{A.19})$$

$$= \pm \frac{1}{k} (\mathcal{F}(\omega; q) - \mathcal{F}(\pi/2; q)) \quad (\text{A.20})$$

where  $\mathcal{F}(\omega; q)$  is the incomplete elliptic integral of the first kind, defined as

$$\mathcal{F}(\omega; q) \equiv \int_0^{\omega} (1 - q^2 \sin^2\tilde{\omega})^{-\frac{1}{2}} d\tilde{\omega} \quad (\text{A.21})$$

Now, solving for the  $y$ -coordinate of the bent rod:

$$\frac{dy}{ds} = \sin\theta \quad (\text{A.22})$$

$$\Rightarrow y = \int_0^s \sin\theta(\tilde{s}) d\tilde{s} \quad (\text{A.23})$$

$$= \int_{\theta_0}^{\theta} \sin\tilde{\theta} \frac{ds}{d\tilde{\theta}} d\tilde{\theta} \quad (\text{A.24})$$

Making the transformation from  $\theta$  to  $\omega$ :

$$\sin\theta = 2\sin\frac{\theta}{2}\cos\frac{\theta}{2} = 2q\sin\omega(1 - q^2\sin^2\omega)^{\frac{1}{2}} \quad (\text{A.25})$$

$$y = \pm \int_{\pi/2}^{\omega} 2q\sin\omega(1 - q^2\sin^2\omega)^{\frac{1}{2}} (2kq\cos\omega)^{-1} \frac{d\theta}{d\omega} d\tilde{\omega} \quad (\text{A.26})$$

$$\Rightarrow y = \pm \frac{2q}{k} \int_{\pi/2}^{\omega} \sin\tilde{\omega} d\tilde{\omega} \quad (\text{A.27})$$

$$\Rightarrow y = \mp \frac{2q}{k} \cos\omega \quad (\text{A.28})$$

Solving for the  $x$ -coordinate of the bent rod:

$$\frac{dx}{ds} = \cos \theta \quad (\text{A.29})$$

$$\Rightarrow x = \int_0^s \cos \theta(\tilde{s}) d\tilde{s} \quad (\text{A.30})$$

$$= \int_{\theta_0}^{\theta} \cos \tilde{\theta} \frac{ds}{d\tilde{\theta}} d\tilde{\theta} \quad (\text{A.31})$$

Making the transformation to  $\omega$ ,

$$\cos \theta = 1 - 2 \sin^2 \frac{\theta}{2} = 1 - 2q^2 \sin^2 \omega \quad (\text{A.32})$$

$$x = \pm \int_{\pi/2}^{\omega} (1 - 2q^2 \sin^2 \tilde{\omega}) (2kq \cos \tilde{\omega})^{-1} \frac{d\theta}{d\tilde{\omega}} d\tilde{\omega} \quad (\text{A.33})$$

$$= \pm \frac{1}{k} \int_{\pi/2}^{\omega} (1 - 2q^2 \sin^2 \tilde{\omega}) (1 - q^2 \sin^2 \tilde{\omega})^{-\frac{1}{2}} d\tilde{\omega} \quad (\text{A.34})$$

$$= \pm \frac{1}{k} \left[ \int_{\pi/2}^{\omega} 2(1 - q^2 \sin^2 \tilde{\omega})^{\frac{1}{2}} d\tilde{\omega} - \int_{\pi/2}^{\omega} (1 - q^2 \sin^2 \tilde{\omega})^{-\frac{1}{2}} d\tilde{\omega} \right] \quad (\text{A.35})$$

$$= \pm \frac{2}{k} (\mathcal{E}(\omega; q) - \mathcal{E}(\pi/2; q)) - \left[ \pm \frac{1}{k} (\mathcal{F}(\omega; q) - \mathcal{F}(\pi/2; q)) \right] \quad (\text{A.36})$$

$$\Rightarrow x = \pm \frac{2}{k} (\mathcal{E}(\omega; q) - \mathcal{E}(\pi/2; q)) - s \quad (\text{A.37})$$

where  $\mathcal{E}(\omega; q)$  is the incomplete elliptic integral of the second kind, defined as follows:

$$\mathcal{E}(\omega; q) = \int_0^{\omega} (1 - q^2 \sin^2 \tilde{\omega})^{\frac{1}{2}} d\tilde{\omega} \quad (\text{A.38})$$

Often, it is useful to have Equation (A.20), Equation (A.37), and Equation (A.28) evaluated at the clamped end of the rod  $\{x(s=L), y(s=L)\}^T = \{x_1, y_1\}^T$ , where the tangent angle is  $\theta(s=L) = \theta_1$  and  $\omega_1 = \omega(s=L)$ :

$$L = \pm \frac{1}{k} (\mathcal{F}(\omega_1; q) - \mathcal{F}(\pi/2; q)) \quad (\text{A.39})$$

$$x_1 = \pm \frac{2}{k} (\mathcal{E}(\omega; q) - \mathcal{E}(\pi/2; q)) - L \quad (\text{A.40})$$

$$y_1 = \mp \frac{2q}{k} \cos \omega_1 \quad (\text{A.41})$$

$$q \sin \omega_1 = \sin \frac{\theta_1}{2} \quad (\text{A.42})$$

The upper branch of these equations represents the case where the curvature  $\kappa$  of the rod is positive (i.e., the angle  $\theta$  is a monotonically increasing function of arclength  $s$ ) and the lower branch, the case where  $\kappa \leq 0$  (and  $\theta$  is a monotonically decreasing function of  $s$ ).

## Appendix B

# Involute of a Circle

An involute of a circle is a plane curve used throughout to model wrapped structures. This curve is a spiral, with each arm of the spiral parallel to adjacent arms. Here, parallelism means that for any point on the spiral, the normally separated point on the adjacent arm is a constant distance away. Additionally, the tangent vectors of these two points are parallel. This property is not shared by other spiral curves; for example, in an Archimedean (or arithmetic) spiral, successive arms are not parallel.

In general, an involute is a curve that follows the end of a taut string being unwrapped from the surface of some generator curve. Therefore, as shown in Figure B.1, an involute of a circle is generated by following a point  $c\{\cos \alpha, \sin \alpha\}$  on a circle of radius  $c$  and the unit tangent to the circle at this point  $\{\sin \alpha, -\cos \alpha\}$ , which defines the direction of the taut string. The length of this string is simply the arclength of the circle  $c\alpha$ , giving the final equation of the involute of the circle.

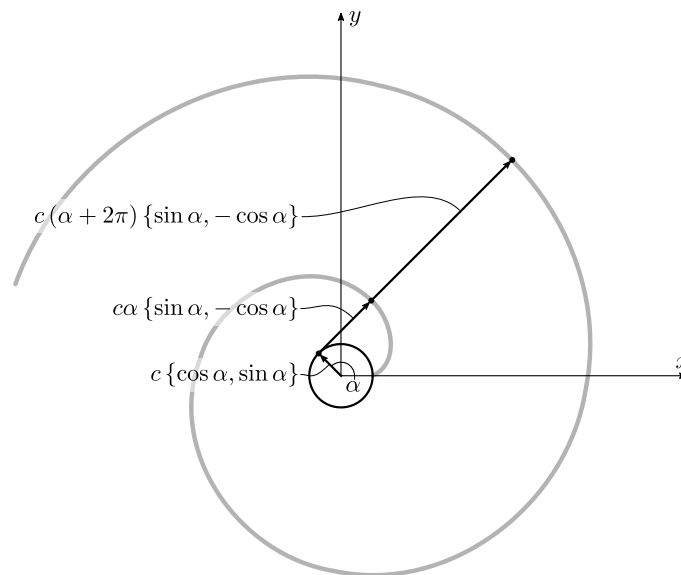


Figure B.1: Involute of a circle.

In Cartesian coordinates, an involute of a circle is described as follows:

$$\mathbf{p}(\alpha) = c \begin{Bmatrix} \cos \alpha \\ \sin \alpha \end{Bmatrix} + c\alpha \begin{Bmatrix} \sin \alpha \\ -\cos \alpha \end{Bmatrix} \quad (\text{B.1})$$

The unit tangent to the involute of a circle is

$$\mathbf{t}(s) = \frac{d\mathbf{p}}{ds} = \frac{d\mathbf{p}}{d\alpha} \frac{d\alpha}{ds} \quad (\text{B.2})$$

$$= c\alpha \begin{Bmatrix} \cos \alpha \\ \sin \alpha \end{Bmatrix} \frac{d\alpha}{ds} \quad (\text{B.3})$$

Since  $\|\frac{d\mathbf{p}}{ds}\| = 1$ , it must be that

$$\mathbf{t}(s) = \begin{Bmatrix} \cos \alpha \\ \sin \alpha \end{Bmatrix} \quad (\text{B.4})$$

and

$$\left| c\alpha \frac{d\alpha}{ds} \right| = \pm 1 \quad (\text{B.5})$$

Taking the upper branch and integrating

$$\frac{d\alpha}{ds} = \frac{1}{c\alpha} \quad (\text{B.6})$$

$$\Rightarrow \int c\alpha \, d\alpha = \int ds \quad (\text{B.7})$$

$$\Rightarrow \alpha^2 - \alpha_0^2 = \frac{2}{c}(s - s_0) \quad (\text{B.8})$$

Using the definition of signed curvature  $\kappa(s)$  from [25]:

$$\kappa(s) = -\frac{d\mathbf{n}}{ds}(s) \cdot \mathbf{t}(s) \quad (\text{B.9})$$

where  $\mathbf{n}(s)$  is the unit normal. The normal  $\mathbf{n}(s)$  is perpendicular to the tangent vector  $\mathbf{t}(s)$ , which

is given by Equation (B.4), and hence:

$$\mathbf{n}(s) = \begin{Bmatrix} -\sin \alpha \\ \cos \alpha \end{Bmatrix} \quad (\text{B.10})$$

$$\frac{d\mathbf{n}(s)}{ds} = \frac{d\mathbf{n}}{d\alpha} \frac{d\alpha}{ds} \quad (\text{B.11})$$

$$= -\frac{1}{c\alpha} \begin{Bmatrix} \cos \alpha \\ \sin \alpha \end{Bmatrix} \quad (\text{B.12})$$

Substituting this and Equation (B.4) into Equation (B.9):

$$\kappa(s) = \frac{1}{c\alpha} \quad (\text{B.13})$$

To see that successive arms are parallel and constantly separated, consider  $\mathbf{p}(\alpha + 2\pi)$ :

$$\mathbf{p}(\alpha + 2\pi) = c \begin{Bmatrix} \cos(\alpha + 2\pi) \\ \sin(\alpha + 2\pi) \end{Bmatrix} + c(\alpha + 2\pi) \begin{Bmatrix} \sin(\alpha + 2\pi) \\ -\cos(\alpha + 2\pi) \end{Bmatrix} \quad (\text{B.14})$$

$$= c \begin{Bmatrix} \cos \alpha \\ \sin \alpha \end{Bmatrix} + c(\alpha + 2\pi) \begin{Bmatrix} \sin \alpha \\ -\cos \alpha \end{Bmatrix} \quad (\text{B.15})$$

$$= \mathbf{p}(\alpha) + 2\pi c \mathbf{n}(\alpha) \quad (\text{B.16})$$

Thus, for every  $\alpha$ ,  $\mathbf{p}(\alpha)$  and  $\mathbf{p}(\alpha + 2\pi)$  are normally separated by distance  $2\pi c$ , and these two points share the same normal.

## Appendix C

# Generator Curves for Compact Wrapping

### C.1 Generator Curve for 2-fold Symmetry

The generator curve  $\mathbf{p}(s) : [0, L/2] \rightarrow \mathbb{R}^2$  consists of three pieces: a semi-circle  $\mathbf{p}_c(s)$  of radius  $R$ , a vertical line  $\mathbf{p}_l(s)$  of some as-yet undetermined length  $s_l$ , and an involute of a circle  $\mathbf{p}_v(s)$  with pitch  $2\pi c = 2n\phi h$ . The involute of the circle is the spiral curve that accounts for the wrapped volume of the stack of strips; the semi-circle and the line are geometric models for the inner part of the wrap. The only requirement on this inner part of the curve is that they connect the end of the involute to the origin in a smooth manner.

$$\mathbf{p}(s) = \begin{cases} \mathbf{p}_c(s) & \text{if } s \in [0, \pi R) \\ \mathbf{p}_l(s) & \text{if } s \in [\pi R, \pi R + s_l) \\ \mathbf{p}_v(s) & \text{if } s \in [\pi R + s_l, L/2] \end{cases} \quad (\text{C.1})$$

Figure C.1 shows these three pieces of the generator curve. It is desired to connect these three pieces in a manner that ensures slope continuity.

To ensure shape and slope continuity of the base curve  $\mathbf{r}(s)$  as defined in Equation (2.14), the semi-circle must begin at the origin  $O = \{0, 0\}$ . It terminates at some point  $A$ , which, for simplicity, is taken to lie on the  $x$ -axis; thus  $A = \{2R, 0\}$ , and the center of the semi-circle lies at  $\{R, 0\}$ . This gives the expression for  $\mathbf{p}_c(s)$ :

$$\mathbf{p}_c(s) = \begin{Bmatrix} R \\ 0 \end{Bmatrix} - R \begin{Bmatrix} \cos s/R \\ \sin s/R \end{Bmatrix} \quad (\text{C.2})$$

$$s \in [0, \pi R) \quad (\text{C.3})$$

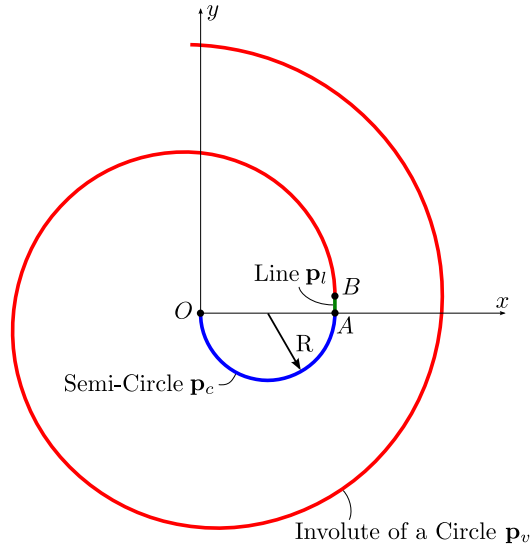


Figure C.1: Generator curve for a z-folded stack.

The tangent to the semi-circle at  $A$  is vertical, thus maintaining slope continuity with the vertical line. The vertical line has some to-be-determined length  $s_l$ , and it must be coincident with point  $A$ . This gives its equation:

$$\mathbf{p}_l(s) = \begin{Bmatrix} 2R \\ 0 \end{Bmatrix} + \begin{Bmatrix} 0 \\ (s - \pi R) \end{Bmatrix} \quad (\text{C.4})$$

$$s \in [\pi R, \pi R + s_l] \quad (\text{C.5})$$

This gives the location of point  $B$  at  $\{2R, s_l\}$ .

Now it is required that the involute of the circle  $\mathbf{p}_v(s)$  begin at this point  $B$ , and, to maintain slope continuity, have a vertical tangent there. The curve of an involute of a circle is given by Equation (B.1). However, here a counter-clockwise rotation by an angle  $\theta$  is imposed on the involute; this extra degree of freedom allows the involute to have a vertical tangent at point  $B$ . Thus the involute is described by

$$\mathbf{p}_v = \begin{Bmatrix} \cos \theta & -\sin \theta \\ \sin \theta & \cos \theta \end{Bmatrix} \left( c \begin{Bmatrix} \cos \alpha \\ \sin \alpha \end{Bmatrix} + c\alpha \begin{Bmatrix} \sin \alpha \\ -\cos \alpha \end{Bmatrix} \right) \quad (\text{C.6})$$

$$= c \begin{Bmatrix} \cos(\alpha + \theta) \\ \sin(\alpha + \theta) \end{Bmatrix} + c\alpha \begin{Bmatrix} \sin(\alpha + \theta) \\ -\cos(\alpha + \theta) \end{Bmatrix} \quad (\text{C.7})$$

$$\alpha \in [\alpha_0, \alpha_{max}] \quad (\text{C.8})$$

where  $\alpha$  is an angular parameter, related to the arclength  $s$  through Equation (B.8). The tangent

vector to the involute is given by Equation (B.4), rotated counter-clockwise by  $\theta$ :

$$\mathbf{t} = \begin{Bmatrix} \cos(\alpha + \theta) \\ \sin(\alpha + \theta) \end{Bmatrix} \quad (\text{C.9})$$

At point  $B$ , when  $\alpha = \alpha_0$ , the tangent vector must be vertical:

$$\begin{Bmatrix} \cos(\alpha_0 + \theta) \\ \sin(\alpha_0 + \theta) \end{Bmatrix} = \begin{Bmatrix} 0 \\ 1 \end{Bmatrix} \quad (\text{C.10})$$

$$\Rightarrow \alpha_0 + \theta = 2\pi m + \frac{\pi}{2} \quad (\text{C.11})$$

where  $m$  is some integer. Without loss of generality, set  $m = 0$ , which gives the value for  $\theta$ :

$$\theta = \frac{\pi}{2} - \alpha_0 \quad (\text{C.12})$$

For shape continuity, the starting point of the involute  $\mathbf{p}_v(\alpha_0)$  must be point  $B$ . This provides the following condition:

$$\begin{Bmatrix} 2R \\ s_l \end{Bmatrix} = c \begin{Bmatrix} \cos(\alpha_0 + \theta) \\ \sin(\alpha_0 + \theta) \end{Bmatrix} + c\alpha_0 \begin{Bmatrix} \sin(\alpha_0 + \theta) \\ -\cos(\alpha_0 + \theta) \end{Bmatrix} \quad (\text{C.13})$$

Using Equation (C.10),

$$\begin{Bmatrix} 2R \\ s_l \end{Bmatrix} = c \begin{Bmatrix} 0 \\ 1 \end{Bmatrix} + c\alpha_0 \begin{Bmatrix} 1 \\ 0 \end{Bmatrix} \quad (\text{C.14})$$

This gives the expression for undetermined parameters  $\alpha_0$  and  $s_l$ :

$$\alpha_0 = \frac{2R}{c} \quad (\text{C.15})$$

$$s_l = c \quad (\text{C.16})$$

Putting this together gives the expression for the generator curve for a wrapped stack of z-folded strips given in Equation (2.15).

## C.2 Generator Curves for $N$ -fold Symmetry

There are two generator curves that are used to describe the wrapped structure in Section 3.1.1,  $\mathbf{q}(s)$  and  $\mathbf{p}(s)$ . For a single sector, these curves exist in a wedge bound by two lines that intersect at an angle  $\beta = \frac{2\pi}{N}$ . To describe adjacent sectors, these generator curves can be rotated through an angle  $\beta$ . Figure C.2 shows the pieces of these curves.

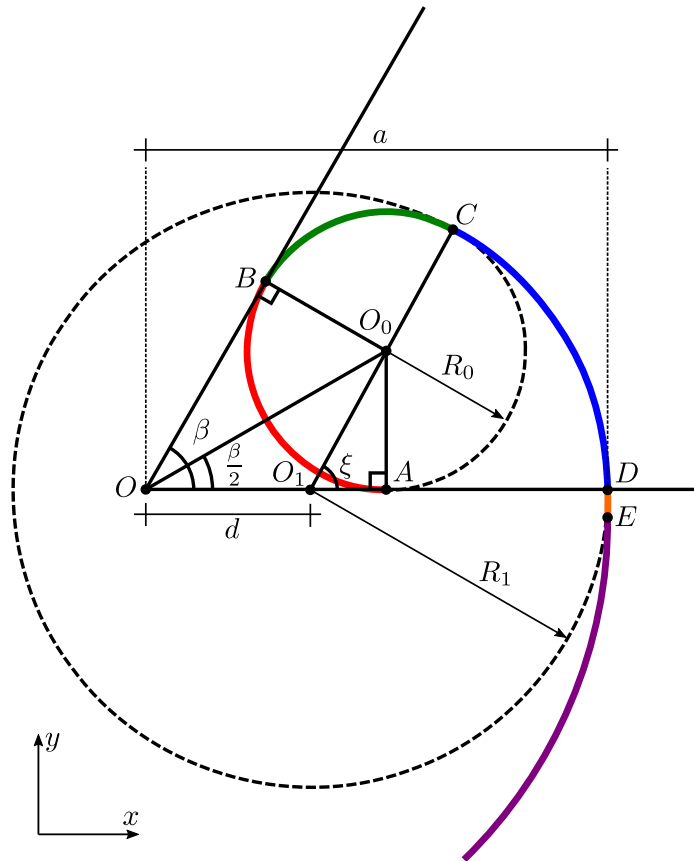


Figure C.2: Generator curve for  $N$ -fold symmetry.

$\mathbf{q}(s)$  is an arc  $AB$  of a circle  $c_0$  of radius  $R_0$ , centered at a point  $O_0$ . To ensure tangency to the two bounding lines of the wedge (to allow slope continuity between adjacent sectors),  $O_0$  lies on the angular bisector of the two bounding lines:

$$O_0 = R_0 \begin{Bmatrix} \cot \frac{\beta}{2} \\ 1 \end{Bmatrix} \quad (\text{C.17})$$

From this, an equation for  $\mathbf{q}(s)$  can be obtained:

$$\mathbf{q}(s) = R_0 \begin{Bmatrix} \cot \frac{\beta}{2} \\ 1 \end{Bmatrix} + R_0 \begin{Bmatrix} \cos \theta(s) \\ \sin \theta(s) \end{Bmatrix} \quad (\text{C.18})$$

$$\theta(s) \in (\pi/2 + \beta, 3\pi/2] \quad (\text{C.19})$$

The generator curve  $\mathbf{p}(s)$  is composed of four pieces: an arc  $BC$ , denoted  $\mathbf{p}_{c0}$ , of circle  $c_0$ ; a second arc  $CD$ , denoted  $\mathbf{p}_{c1}$ , of circle  $c_1$  of radius  $R_1$  centered at  $O_1$ ; a vertical line  $DE$ , denoted  $\mathbf{p}_l$ , of some undetermined length  $s_l$ ; and an involute of a circle  $\mathbf{p}_v$  with pitch  $2\pi c = 2NH$ .

The vertical line  $\mathbf{p}_l$ , and the involute  $\mathbf{p}_v$  are determined exactly the same way as Section C.1; the vertical line has length  $c$ , and the involute, which begins at point  $E = \{a, -c\}$ , has the expression

$$\mathbf{p}_v = c \begin{Bmatrix} -\sin(\alpha - \alpha_0) + \alpha \cos(\alpha - \alpha_0) \\ -\cos(\alpha - \alpha_0) - \alpha \sin(\alpha - \alpha_0) \end{Bmatrix} \quad (\text{C.20})$$

$$\alpha^2 = \frac{2}{c}(s - s_0) + \alpha_0^2 \quad (\text{C.21})$$

$$\alpha_0 = \frac{a}{c} \quad (\text{C.22})$$

The  $y$ -coordinate of the involute has been negated as compared to Equation (2.15) to account for the fact that the involute here is reflected through the  $x$ -axis as compared to the one in Section C.1.

The  $x$ -coordinate of point  $E$ , denoted  $a$ , is determined by considering the other two pieces of the generator curve.

$\mathbf{p}_{c0}$  is a continuation of the circular arc  $AB$ ; as such, shape and slope continuity with  $\mathbf{q}(s)$  are maintained. It continues from  $\theta = \pi/2 + \beta$  to an as-yet undetermined angle  $\xi$ :

$$\mathbf{p}_{c0}(s) = R_0 \begin{Bmatrix} \cot \frac{\beta}{2} \\ 1 \end{Bmatrix} + R_0 \begin{Bmatrix} \cos \theta(s) \\ \sin \theta(s) \end{Bmatrix} \quad (\text{C.23})$$

$$\theta(s) \in (\xi, \pi/2 + \beta] \quad (\text{C.24})$$

$\mathbf{p}_{c1}$  is a circular arc of a to-be-determined radius  $R_1$  that is tangent to  $\mathbf{p}_{c0}$  at point  $C$ . As such, the center of this arc  $O_1$  must lie on the line  $O_0C$ . To connect to the vertical line at point  $D$ , the circular arc  $\mathbf{p}_{c1}$  must terminate at the  $x$ -axis with a vertical tangent. This locates its center  $O_1$  at the intersection of the line  $O_0C$  and the  $x$ -axis; thus  $O_1 = \{d, 0\}$ . Its  $x$ -coordinate  $d$  can be related to the angle  $\xi$ .

Consider  $\triangle O_1O_0A$ . From Figure C.2,

$$|O_0A| = R_0 \quad (\text{C.25})$$

$$\Rightarrow |O_1A| = R_0 \cot \xi \quad (\text{C.26})$$

From  $\triangle OO_0A$

$$|OA| = R_0 \cot \frac{\beta}{2} \quad (\text{C.27})$$

Since  $d + |O_1A| = |OA|$ , it can be obtained that

$$d = R_0 \left( \cot \frac{\beta}{2} - \cot \xi \right) \quad (\text{C.28})$$

A similar relationship can be obtained relating  $R_1$  to  $R_0$  and  $\xi$ . Once again, consider  $\triangle O_1O_0A$ :

$$|O_1O_0| = |O_0A| \sec \xi = R_0 \sec \xi \quad (\text{C.29})$$

Since  $|O_1C| = R_1$  and  $|O_0C| = R_0$ , it can be obtained that

$$|O_1C| = |O_1O_0| + |O_0C| \quad (\text{C.30})$$

$$\Rightarrow R_1 = R_0 \sec \xi + R_0 \quad (\text{C.31})$$

$$= R_0 (\sec \xi + 1) \quad (\text{C.32})$$

Thus, by fixing the value of  $\xi$ , the radius  $R_1$  and center  $O_1 = \{d, 0\}$  of the circular arc  $\mathbf{p}_{c1}$  can be determined through Equation (C.32) and Equation (C.28), respectively. To find a suitable value for  $\xi$ , the position of point  $D$  at  $\{a, 0\}$  is determined using the following argument.

Recall that the wrapped shape of these structures has  $N$ -fold symmetry. This symmetry needs to be considered here. The sector that exists counter-clockwise to the present sector must be allowed sufficient space so as to avoid self-intersection in the wrapped structure. Consider the part of the generator curve labeled  $DEI$  in Figure C.3; its rotated copy  $D'E'I'$  must be placed at a location such that it exists some length  $MH$  away from the point  $G$ , which represents the projection of circle  $c_1$  centered at  $O_1$  onto the line  $OD'$ . Thus,

$$|GD'| = MH \quad (\text{C.33})$$

$H = n\phi h$  is the half the thickness of each arm, and  $M \geq 1$  is a free parameter.

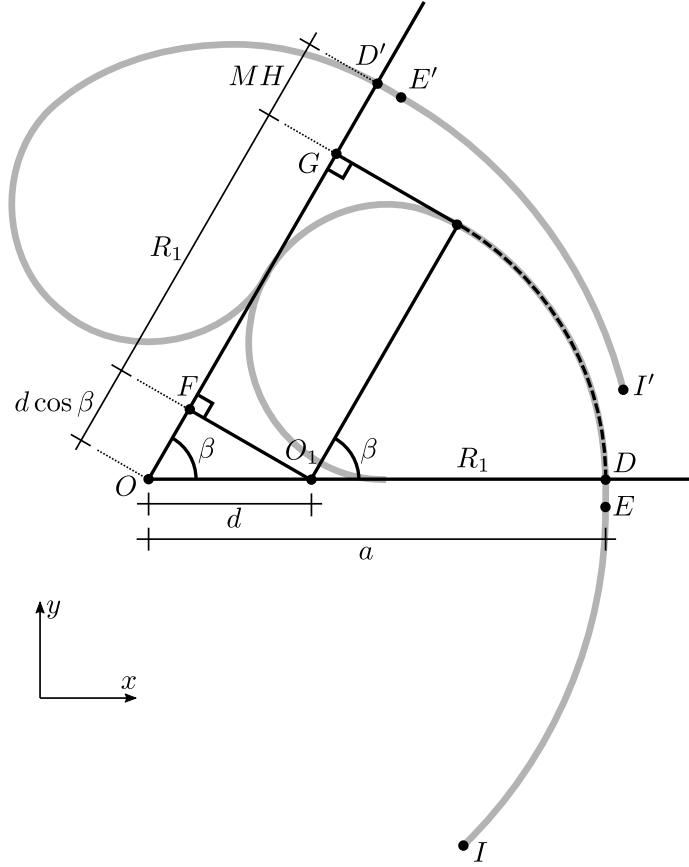


Figure C.3: To fix the geometry of this curve, the position of point  $D$  must be determined. This is done by considering the rotational symmetry of the problem and allowing the rotated curve  $D'E'I'$  enough space to avoid intersecting the original curve  $DEI$ .

From  $N$ -fold symmetry about the origin  $O$ ,

$$|OD| = |OD'| = a \quad (\text{C.34})$$

Projected onto line  $OD'$ , the center  $O_1$  of circle  $c_1$  falls on point  $F$ . This gives

$$|OF| = d \cos \beta \quad (\text{C.35})$$

and

$$|FG| = R_1 \quad (\text{C.36})$$

Combining Equation (C.34), Equation (C.35), Equation (C.36), and Equation (C.33):

$$|OD'| = |OF| + |FG| + |GD'| \quad (\text{C.37})$$

$$\Rightarrow a = d \cos \beta + R_1 + MH \quad (\text{C.38})$$

From the location of point  $D$  at  $\{a, 0\}$ :

$$a = d + R_1 \quad (\text{C.39})$$

Substituting Equation (C.38) into Equation (C.39):

$$d + R_1 = d \cos \beta + R_1 + MH \quad (\text{C.40})$$

$$\Rightarrow d(1 - \cos \beta) = MH \quad (\text{C.41})$$

Substituting Equation (C.28), and solving for  $\xi$ :

$$\Rightarrow R_0 \left( \cot \frac{\beta}{2} - \cot \xi \right) = \frac{MH}{1 - \cos \beta} \quad (\text{C.42})$$

$$\Rightarrow \xi = \operatorname{arccot} \left[ \cot \frac{\beta}{2} - \frac{MH}{R_0(1 - \cos \beta)} \right] \quad (\text{C.43})$$

$\xi$  must exist within the range  $[\beta/2, \beta + \pi/2]$ : the lower bound represents the case when center  $O_1$  of arc  $CD$  is coincident with the origin  $O$  and the arc  $CD$  in Figure C.2 spans half the wedge; the upper bound is the case arc  $BC$  in Figure C.2 vanishes. These bounds on  $\xi$  provide corresponding bounds on the value of  $M$ :

$$M \in \left[ 0, \frac{R_0}{H} \tan \beta \right] \quad (\text{C.44})$$

Within this range,  $M$  is a free tunable parameter.

## Appendix D

# TRAC Cross-Section Properties

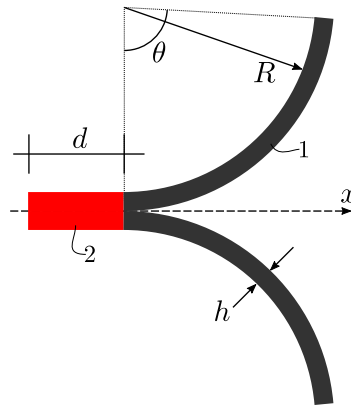


Figure D.1: TRAC longeron cross section.

The area of a TRAC section can be calculated as the sum of the areas  $2A_1$  of the flanges (labeled 1 in Figure D.1) and the area  $A_2$  of the bonded section (labeled 2 in Figure D.1):

$$A = 2A_1 + A_2 \quad (\text{D.1})$$

$$A_1 = \frac{\theta}{2} ((R+h)^2 - R^2) \quad (\text{D.2})$$

$$= \frac{h\theta}{2} (2R+h) \quad (\text{D.3})$$

$$A_2 = 2hd \quad (\text{D.4})$$

The second moment of area of a TRAC longeron section about the  $x$  axis can be calculated as

the sum of the second moments of area of the flanges  $I_{xx,1}$  and the bonded section  $I_{xx,2}$ :

$$I_{xx} = 2I_{xx,1} + I_{xx,2} \quad (\text{D.5})$$

$$I_{xx,1} = \int \int y^2 dA \quad (\text{D.6})$$

$$y = (R + h) - r \cos \phi \quad (\text{D.7})$$

$$\Rightarrow I_{xx,1} = \int_0^\theta \int_R^{R+h} (R + h - r \cos \phi) r dr d\phi \quad (\text{D.8})$$

$$= \frac{h}{48} \left[ \begin{array}{l} -32(h + R)(h^2 + 3hr + 3R^2) \sin \theta \\ +6(h + 2R) \{ (5h^2 + 10hR + 6R^2)\theta \\ + h^2 \cos \theta \sin \theta + R(h + R) \sin 2\theta \} \end{array} \right] \quad (\text{D.9})$$

$$I_{xx,2} = \frac{(2h)^3 d}{12} = \frac{2h^3 d}{3} \quad (\text{D.10})$$

## Appendix E

# Cutting Pattern

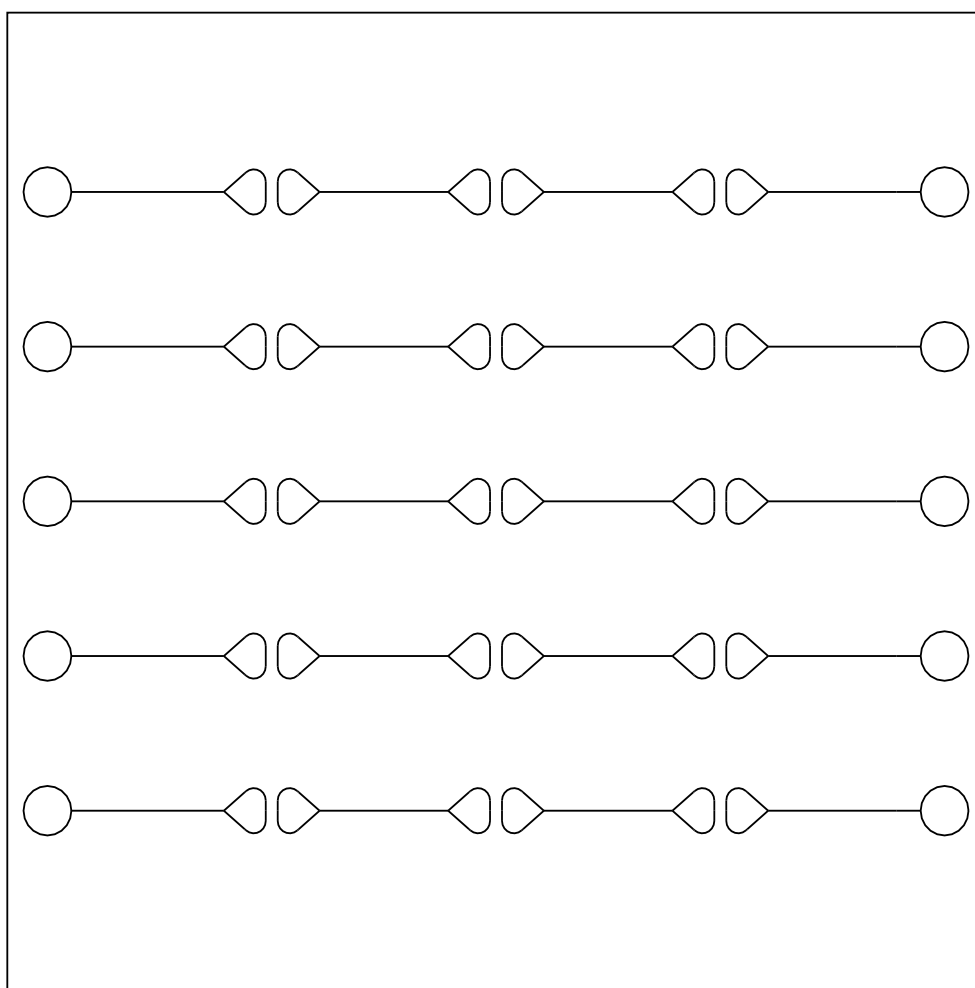


Figure E.1: Cutting pattern with 6 strips, and 3 ligament connections between adjacent strips.

Cutting along this pattern will produce a simple z-foldable structure that can be slip wrapped as described in Chapter 2. Please note that paper ligaments are not very robust, and will likely tear if overly stressed.

# Bibliography

- [1] “NASA Announces Next Steps on Journey to Mars: Progress on Asteroid Initiative.” <http://www.jpl.nasa.gov/news/news.php?feature=4523>, 2015. Accessed 2016.04.16.
- [2] H. Sawada, O. Mori, N. Okuizumi, Y. Shirasawa, Y. Miyazaki, M. Natori, S. Matunaga, H. Furuya, and H. Sakamoto, “Mission Report on The Solar Power Sail Deployment Demonstration of IKAROS,” in *52<sup>nd</sup> AIAA/ASME/ASCE/AHS/ASC Structures, Structural Dynamics, and Materials Conference*, 2011.
- [3] T. W. Murphey, *A nonlinear elastic constitutive model for wrinkled thin films*. PhD thesis, University of Colorado at Boulder, 2000.
- [4] A. Papa and S. Pellegrino, “Systematically creased thin-film membrane structures,” *Journal of Spacecraft and Rockets*, vol. 45, no. 1, pp. 10–18, 2008.
- [5] K. Miura, “Method of packaging and deployment of large membranes in space,” in *Proceedings of the 31st Congress of the International Astronautical Federation*, pp. 1–10, 1980.
- [6] K. Miura and M. Natori, “2-D array experiment on board a space flyer unit,” *Space Solar Power Review*, vol. 5, pp. 345–356, 1985.
- [7] C. Bidy and T. Svitek, “LightSail-1 Solar Sail Design and Qualification,” in *41<sup>st</sup> Aerospace Mechanisms Symposium*, pp. 451–463, 2012.
- [8] S. D. Guest and S. Pellegrino, “Inextensional wrapping of flat membranes,” in *First International Seminar on Structural Morphology*, pp. 203–215, Sept. 1992.
- [9] S. A. Zirbel, R. J. Lang, M. W. Thomson, D. A. Sigel, P. E. Walkemeyer, B. P. Trease, S. P. Magleby, and L. L. Howell, “Accommodating Thickness in Origami-Based Deployable Arrays,” *Journal of Mechanical Design*, vol. 135, p. 111005, Nov 2013.
- [10] E. E. I. Montgomery and C. L. Adams, “NanoSail-D,” in *CubeSat Developer’s Workshop*, 2008.
- [11] N. Lee and S. Close *Proceedings of the Royal Society of London A: Mathematical, Physical and Engineering Sciences*.

- [12] N. Lee and S. Pellegrino, “Multi-layer membrane structures with curved creases for smooth packaging and deployment,” in *AIAA SciTech Spacecraft Structures Conference*, 2014.
- [13] Y. Satou and H. Furuya, “Fold line based on mechanical properties of crease in wrapping fold membrane,” in *54<sup>th</sup> AIAA/ASME/ASCE/AHS/ASC Structures, Structural Dynamics, and Materials Conference*, April 2013.
- [14] C. Hoberman, “Reversibly expandable three-dimensional structure,” 1988. United States Patent Number 4,780,344.
- [15] Y. Chen, R. Peng, and Z. You, “Origami of thick panels,” *Science*, vol. 349, pp. 396–400, 2015.
- [16] M. Trautz and A. Künstler, “Deployable folded plate structures: folding patterns based on 4-fold-mechanism using stiff plates,” in *Proceedings of the International Association for Shell and Spatial Structures Symposium*, October 2009.
- [17] T. Tachi, “Rigid-Foldable Thick Origami,” in *Origami 5* (M. Yim, ed.), pp. 253–263, 2011.
- [18] B. J. Edmondson, R. J. Lang, S. P. Magleby, and L. L. Howell, “An offset panel technique for thick rigidly foldable origami,” in *Proceedings of the ASME 2014 International Design Engineering Technical Conferences*, 2014.
- [19] W. D. Reynolds and T. W. Murphey, “Elastic Spiral Folding for Flat Membrane Apertures,” in *55<sup>th</sup> AIAA/ASME/ASCE/AHS/ASC Structures, Structural Dynamics, and Materials Conference*, Jan. 2014.
- [20] J. S. Ku and E. D. Demaine, “Folding flat crease patterns with thick materials,” in *ASME 2015 International Design Engineering Technical Conferences*, 2015.
- [21] B. Tibbalds, S. D. Guest, and S. Pellegrino, “Inextensional Packaging of Thin Shell Slit Reflectors,” *Technische Mechanik*, vol. 24, no. 3-4, pp. 211–220, 2004.
- [22] W. D. Reynolds, T. W. Murphey, and J. A. Banik, “Highly Compact Wrapped-Gore Deployable Reflector,” in *52<sup>nd</sup> AIAA/ASME/ASCE/AHS/ASC Structures, Structural Dynamics, and Materials Conference*, April 2011.
- [23] G. Greschik, “Deployment of Dishes with Surface Discontinuities,” *Journal of Spacecraft and Rockets*, vol. 33, no. 4, 1996.
- [24] M. Arya, N. Lee, and S. Pellegrino, “Wrapping Thick Membranes with Slipping Folds,” in *2<sup>nd</sup> Spacecraft Structures Conference*, 2015.
- [25] M. Spivak, *A Comprehensive Introduction to Differential Geometry*, vol. II. Houston, Texas: Publish or Perish, Inc, 3 ed., 1999.

- [26] DuPont Teijin Films, “Mylar Polyester Film Product Information,” 2003.
- [27] W. E. Lanford, “Folding appartus,” 1961. United States Patent Number 3,010,372.
- [28] H. M. Irvine, *Cable Structures*. Cambridge, Massachusetts: The MIT Press, 1981.
- [29] A. S. Bonin and K. A. Seffen, “De-wrinkling of pre-tensioned membranes,” *International Journal of Solids and Structures*, vol. 51, no. 19-20, pp. 3303–3313, 2014.
- [30] J. A. Banik and T. W. Murphey, “Synchronous Deployed Solar Sail Subsystem Design Concept,” in *48<sup>th</sup> AIAA/ASME/ASCE/AHS/ASC Structures, Structural Dynamics, and Materials Conference*, April 2007.
- [31] M. Gärdsback and G. Tibert, “Deployment Control of Spinning Space Webs,” *Journal of Guidance, Control, and Dynamics*, vol. 32, no. 1, pp. 40–50, 2009.
- [32] M. Arya, N. Lee, and S. Pellegrino, “Ultralight Structures for Space Solar Power Satellites,” in *3<sup>rd</sup> Spacecraft Structures Conference*, 2016.
- [33] E. D. Demaine, M. L. Demaine, V. Hart, G. N. Price, and T. Tachi, “(Non)existence of Pleated Folds: How Paper Folds Between Creases,” *Graphics and Combinatorics*, vol. 27, no. 3, pp. 377–397, 2012.
- [34] H. Furuya, O. Mori, N. Okuizumi, Y. Shirasawa, M. C. Natori, Y. Miyazaki, and S. Matunaga, “Manufacturing and Folding of Solar Sail IKAROS,” in *52<sup>nd</sup> AIAA/ASME/ASCE/AHS/ASC Structures, Structural Dynamics, and Materials Conference*, pp. 4–7, April 2011.
- [35] G. Greschik and M. M. Mikulas, “Design Study of a Square Solar Sail Architecture,” *Journal of Spacecraft and Rockets*, vol. 39, pp. 653–661, Sept. 2002.
- [36] J. M. Fernandez, V. J. Lappas, and A. J. Daton-Lovett, “Completely Stripped Solar Sail Concept Using Bi-stable Composite Booms,” *Acta Astronautica*, vol. 69, no. 1, 2011.
- [37] V. M. Melnikov and V. A. Koshelev, *Large Space Structures Formed by Centrifugal Forces*. Amsterdam, The Netherlands: Gordon and Breach Science Publishers, 1998.
- [38] K. A. Seffen, Z. You, and S. Pellegrino, “Folding and deployment of curved tape springs,” *International Journal of Mechanical Sciences*, vol. 42, no. 10, pp. 2055–2073, 2000.
- [39] Z. P. Bazant and L. Cedolin, *Stability of Structures: Elastic, Inelastic, Fracture and Damage Theories*. Singapore: World Scientific Publishing Company, 2010.
- [40] S. P. Timoshenko and J. M. Gere, *Theory of Elastic Stability*. New York: McGraw-Hill, 2 ed., 1961.

- [41] J. A. Banik and T. W. Murphey, "Performance Validation of the Triangular Rollable and Collapsible Mast," in *24<sup>th</sup> Annual AIAA/USU Conference on Small Satellites*, 2010.
- [42] "North thin ply technologies." <http://www.thinplytechnology.com/>. Accessed 2016.04.05.
- [43] S. Tsai, S. Sihn, and R. Kim, "Thin ply composites," in *46<sup>th</sup> AIAA/ASME/ASCE/AHS/ASC Structures, Structural Dynamics and Materials Conference*, 2005.
- [44] J. Steeves, *Multilayer Active Shell Mirrors*. PhD thesis, California Institute of Technology, 2015.
- [45] I. Asimov, "Reason," in *Astounding Science-Fiction* (J. W. Campbell Jr., ed.), Street & Smith Publications, Inc, April 1941.
- [46] P. E. Glaser, "Power from the Sun: Its Future," *Science*, vol. 162, no. 3856, pp. 857–61, 1968.
- [47] T. F. Stocker, D. Qin, G.-K. Plattner, M. M. B. Tignor, S. K. Allen, J. Boschung, A. Nauels, Y. Xia, V. Bex, and P. M. Midgley, eds., *Climate Change 2013: The Physical Science Basis. Contribution of Working Group I to the Fifth Assessment Report of the Intergovernmental Panel on Climate Change*. Cambridge, United Kingdom and New York, NY, USA: Cambridge University Press, 2013.
- [48] O. Edenhofer, R. Pichs-Madruga, Y. Sokona, E. Farahani, S. Kadner, K. Seyboth, A. Adler, I. Baum, S. Brunner, P. Eickemeier, B. Kriemann, J. Savolainen, S. Schlömer, C. von Stechow, T. Zwickel, and J. C. Minx, eds., *Climate Change 2014: Mitigation of Climate Change. Contribution of Working Group III to the Fifth Assessment Report of the Intergovernmental Panel on Climate Change*. Cambridge, United Kingdom and New York, NY, USA: Cambridge University Press, 2014.
- [49] R. Gross, P. Heptonstall, D. Anderson, T. Green, M. Leach, and J. Skea, "The Costs and Impacts of Intermittency: An assessment of the evidence on the costs and impacts of intermittent generation on the British electricity network," tech. rep., 2006.
- [50] US Department of Energy and National Aeronautics and Space Administration, "Satellite Power System: Concept Development & Evaluation Program," Tech. Rep. October, 1978.
- [51] C. Carrington, J. Fikes, M. Gerry, D. Perkinson, H. Feingold, and J. Olds, "The Abacus/Reflector and integrated symmetrical concentrator - Concepts for space solar power collection and transmission," in *35<sup>th</sup> Intersociety Energy Conversion Engineering Conference*, 2000.
- [52] J. C. Mankins, "A Technical Overview of the Suntower Solar Power Satellite Concept," *Acta Astronautica*, vol. 50, no. 6, pp. 369–377, 2002.

- [53] J. C. Mankins, *The Case for Space Solar Power*. Houston, Texas: The Virginia Edition, 2014.
- [54] M. Oda, “Realization of the Solar Power Satellite Using the Formation Flying Solar Reflector,” in *NASA Formation Flying Symposium*, 2004.
- [55] W. Seboldt, M. Klimke, M. Leipold, and N. Hanowski, “European Sail Tower SPS concept,” *Acta Astronautica*, vol. 48, no. 5-12, pp. 785–792, 2001.
- [56] S. Sasaki, K. Tanaka, K. Higuchi, N. Okuizumi, S. Kawasaki, N. Shinohara, K. Senda, and K. Ishimura, “A new concept of solar power satellite: Tethered-SPS,” *Acta Astronautica*, vol. 60, no. 3, pp. 53–165, 2007.
- [57] S. Sasaki, K. Tanaka, K. Higuchi, N. Okuizumi, S. Kawasaki, M. Shinohara, and K. Ishimura, “Construction scenario for tethered solar power satellite,” in *57<sup>th</sup> International Astronautical Congress*, 2006.
- [58] D. M. Murphy, “The Scarlet Solar Array: Technology Validation and Flight Results,” in *Proceedings of the Deep Space I Technology Validation Symposium*, 2000.
- [59] J. J. Wachholz and D. M. Murphy, “SCARLET I: Mechanization Solutions for Deployable Concentrator Optics Integrated with Rigid Array Technology,” in *30<sup>th</sup> Aerospace Mechanisms Symposium*, 1996.
- [60] R. S. Pappa, J. A. Woods-Vedeler, and T. W. Jones, “In-Space Structural Validation Plan for a Stretched-Lens Solar Array Flight Experiment,” in *20<sup>th</sup> International Modal Analysis Conference*, 2002.
- [61] M. O’Neill, A. McDanal, M. Piszczor, M. Eskenazi, P. Jones, C. Carrington, D. Edwards, and H. Brandhorst, “The stretched lens ultralight concentrator array,” in *Photovoltaic Specialists Conference, 2000. Conference Record of the Twenty-Eighth IEEE*, pp. 1135–1138, 2000.
- [62] B. R. Spence, S. F. White, and K. Schmid, “Rollable and accordion foldable refractive concentrator space solar array panel,” 2014. United States Patent Number 8,636,253.
- [63] Steering Committee for NASA Technology Roadmaps, *NASA Space Technology Roadmaps and Priorities: Restoring NASA’s Technological Edge and Paving the Way for a New Era in Space*. 2012.
- [64] L. T. Tan and S. Pellegrino, “Thin-shell deployable reflectors with collapsible stiffeners: Part 1 Approach,” *AIAA Journal*, vol. 44, no. 11, pp. 2515–2523, 2006.
- [65] F. Rimrott, “Storable Tubular Extendable Member: A Unique Machine Element,” *Journal of Machine Design*, vol. 37, pp. 156–165, 1965.

- [66] L. Herbeck, M. Eiden, M. Leipold, C. Sickinger, and W. Unckenbold, “Development and test of deployable ultra-lightweight CFRP booms for a Solar Sail,” in *Proceedings of the European Conference on Spacecraft Structures, Materials and Mechanical Testing*, pp. 107–112, 2000.
- [67] A. Cavallo, G. De Maria, C. Natale, and S. Pirozzi, “Robust control of flexible structures with stable bandpass controllers,” *Automatica*, vol. 44, no. 5, pp. 1251–1260, 2008.
- [68] C. R. McInnes, *Solar Sailing: Technology, Dynamics, and Mission Applications*. London: Springer Praxis, 1999.
- [69] G. M. T. D’Eleuterio and G. R. Heppler, *Newton’s Second Law and All That: A Treatment of Classical Mechanics*. 2006.
- [70] D. M. Murphy, M. E. McEachen, B. D. Macy, and J. L. Gaspar, “Demonstration of a 20-m Solar Sail System,” in *46<sup>th</sup> AIAA/ASME/ASCE/AHS/ASC Structures, Structural Dynamics & Materials Conference*, 2005.